Broadband Waveform Modeling and Its Application to the Lithospheric Structure of the Tibetan Plateau

Thesis by

Lupei Zhu

In Partial Fulfillment of the Requirements

for the Degree of

Doctor of Philosophy

Caltech

Pasadena, California

1998

(Submitted February 26, 1998)

Acknowledgements

My five years of graduate study at the Seismo Lab have been a very pleasant experience. To the faculty, staff, and my fellow students I would like to extend my sincere thanks.

I have benefited greatly from my advisor Don Helmberger who, throughout my entire research work, has been very supportive. He seemed always enthusiastic in whatever I did. He is truly a waveform master. Under his guidance, I learned how to appreciate the beauty of a seismogram. It is amazing that once you devote yourself to it, each wiggle of the waveform is willing to tell you a secret about our Earth.

The interactions with other Seismo Lab faculty have been exciting and also intellectually challenging. Hiroo Kanamori and Don Anderson showed me a broad view of seismology. I want to thank Rob Clayton, my academic advisor, for walking me through the Lab when I first arrived and providing all the needed assistance in the following years.

I wish to thank Cheryl Contopulos, Ann Freeman, Evelina Cui, Elisa Loeffen, and all other Seismo Lab staff for their support and back-stage work which has made the Seismo Lab such a wonderful place. I enjoyed all the birthday parties and picnics.

My officemates have been a constant source of help in every aspect. Sharon, Tim, Weishi, Lian-she, Xiaodong, and Miriam made it easier for me to settle down at Caltech in the first year. Julie and Magali are fun to talk with. Many of my fellow students have provided help for me. Craig and Tim spent lots of time reviewing almost all manuscripts I wrote and improved them greatly. Blair solved many of my computer-related problems. Working with my classmates, Lianxing, Igor, Jasha, Xiaoming, George, Xi, on homework and projects was interesting and fun.

There are many people who had significant impact on me and my research interests during my early years of pursuing geophysics degrees, including Huilan Zhou at the University of Science and Technology of China, and Rongsheng Zeng and Yuntai

Chen at the Institute of Geophysics, SSB, Beijing. I want to thank Rongsheng Zeng, Tom Owens, and Francis Wu for initiating the 1991-1992 Sino-US Tibet seismic experiment which has produced the high-quality dataset used in this thesis. Through the experiment I had the pleasure to work with my colleagues of IGSSB, Zhi-feng Ding, Wei-guo Sun, Guang-ying Chen, and Zheng-qin He, and the US participants, including George Randall, Dan McNamara, Randy Kuehnel, and Gregory Wagner. Tom and Dan have been very supportive friends to me for all these years.

Some chapters of this thesis are based on papers I published in the past four years. Many people helped me by reviewing the manuscripts, including Hiroo Kanamori, Egill Hauksson, Larry Burdick, C. J. Ammon, Mark Simons, Bill Keller, and several anonymous reviewers. Chapter 6 is a collaborative work with Tom Owens. I thank Georges Poupinet and Anne Paul for providing the Sino-French 1993 Lithoscope Kunlun experiment data. The Ph.D. research work was supported by NSF under contracts EAR-9196115 and EAR89-20136, by SCEC, contract No. 569933, and by the Department of Defense as monitored by the Air Force Office of Scientific Research under contracts F49620-92-J-0470 and F19628-95-C-0096.

I am grateful to Joann Stock and Kerry Sieh who made a careful review of the whole thesis while serving in my thesis exam committee.

Finally, I thank my parents for their support throughout my education. I also want to thank my daughter Daphne for the joy she's brought to my life. In the end, I have to acknowledge my debts to my wife Yingshu. Without her caring and patience, I wouldn't have been able to finish this thesis.

Abstract

This thesis presents a study of the lithospheric structure of the Tibetan Plateau. The data are broadband seismic waveforms recorded during the 1991-1992 Sino-US Tibet PASSCAL experiment. Several techniques are developed to retrieve the structural information from these waveforms at ranges from near-field to teleseismic distances.

First, a 1-D average crustal velocity model is derived from regional earthquakes, based on travel times of various phases and modeling waveforms of Love waves. The source mechanisms and depths of 62 events in Tibet and surrounding areas are determined using this 1-D model. The result is that most earthquakes occur at shallow depths, between 5 and 15 km. Thrust faulting source mechanisms are dominant on the margins of the plateau. Within the plateau but at locations with surface elevation less than 5 km, source mechanisms are a mixture of strike-slip and thrust. In areas with surface elevation higher than 5 km, all events show consistently normal faulting, which indicates that a large portion of the high plateau is under EW extension. I also found three sub-crustal earthquakes at depth range between 70 and 80 km in southern Tibet. Their existence suggests relatively cold uppermost mantle in the region.

The lateral variations are investigated using teleseismic waveforms. Crustal thickness and Vp/Vs ratio at each station are estimated using receiver function analysis. I found crustal Vp/Vs ratios to range from 1.75 to 2.0 and crustal thicknesses from 55 to 80 km. On average the northern Tibetan crust is 20 km thinner and has a higher Vp/Vs ratio than the southern part. Teleseismic P and S arrival delays exhibit strong azimuthal and lateral variation. The uniform surface elevation of Tibet coupled with large variations of crustal thickness and upper mantle velocity suggest that the north-central plateau is supported partly by a hot upper mantle. A low velocity layer is found in the mid-crust of northern Tibet. Modeling the anomalous "double-pulse" P waveform at the northernmost station reveals a 15 to 20 km Moho offset between the plateau and the Qaidam Basin.

Contents

List of Figures

List of Tables

Chapter 1

Introduction

Each time an earthquake occurs, it radiates seismic waves which, after traveling through Earth, are recorded by seismic stations on the surface. Seismic waves are practically the only signal that can penetrate the deep Earth to bring back information about the interior of our planet. The last decade has seen a dramatic increase in the number of stations equipped with broadband, high dynamic range sensors. As a result, our ability to understand dynamic processes inside Earth has been greatly enhanced.

A broadband seismic waveform carries signatures of both earthquake source and structure along the propagation path. However, modeling a seismic waveform is complicated by the fact that the earthquake source and structure response are coupled in the sense that in order to resolve the structure one needs to know the source and vice versa. This complexity predetermines that waveform modeling needs to be done in a progressive fashion. First, we establish a 1-D reference velocity model, or starting model, from those observations that are not very sensitive to source parameters, such as differential travel times between different seismic phases or inter-station surface wave group/phase velocity measurements. Sometimes, an earthquake source can be determined independently by other observations. In other cases, source effects show up preferentially on one component of three-component records which then can be used as an effective source time function to isolate structure effects from the other two components. An example is the vertical component of a teleseismic P wave which usually has little interaction with crustal structure because of the wave's near vertical incidence. The isolated response from the horizontal components, so-called receiver functions, are frequently used to investigate structure beneath stations [*Langston*, 1977].

Once the 1-D model is available, its theoretical response can be computed so that earthquake sources can be estimated from observed waveforms, assuming that the 1-D model is a reasonable approximation of the real Earth structure between source and receiver. Currently, earthquakes of magnitude larger than 5.5 anywhere on the globe can be processed semi-automatically or automatically to determine their moment tensors [*Dziewonski and Woodhouse*, 1983; *Sipkin*, 1986; *Kawakatsu*, 1995; *Polet and Kanamori*, 1995]. As magnitudes get smaller, one has to rely on records in regional distance ranges (less than 1000 km). At such distances, broadband seismic waveforms sample the shallow part of Earth (crust and uppermost mantle). Because of rapid variation of structure both vertically and laterally, regional waveforms exhibit many fascinating features. For crustal events beyond the distance range of 200-300 km, the first 1-2 min of waveform is called *Pnl*, which consists of the *Pn* arrival followed by the crust-trapped *P-SV* multiple conversions (*PL*). The large-amplitude surface waves (Rayleigh/Love) appear later in the record. If the source is below the crust, shear-coupled *P* waves (*sPmP*) can often be observed ahead of the direct *S*.

There are two issues which make source estimation using the whole waveform difficult. First, a whole-waveform inversion is mainly controlled by the surface waves because of their large amplitude. However, *Pnl* is very useful for source estimation because it is more stable and less sensitive to velocity structure [*Helmberger and Engen*, 1980], and the amplitude ratio between *Pnl* and surface waves is a good discriminant of source depth. Second, these two portions of the waveform sample different parts of the structure and thus require different adjustments of the velocity model used. To overcome these difficulties, *Zhao and Helmberger* [1994] developed a source estimation technique which breaks the whole waveform into *Pnl* and surface wave segments and inverts them independently. When comparing each segment with synthetics, it allows a time shift between the two to get maximum alignment. This relaxation of timing proves to be quite helpful when only imperfect velocity models and inaccurate event locations are available at the beginning.

Source parameters determined using the 1-D velocity model help us to improve the starting model. For example, more layering may need to be added to the structure.

Usually, lateral variation is revealed by different source-receiver paths. This leads to further regionalization of the study area with several 1-D models, or even a 3-D model. The waveform modeling procedure can now be iterated upon using the new model as the reference model.

It is my intention in this thesis to establish the procedure described above and apply it to the Tibetan Plateau using a data set collected in a PASSCAL experiment between 1991 and 1992 [*Owens et al.*, 1993]. The Tibetan Plateau is chosen because of its great tectonic interest to the geophysical and geological communities. Unlike other places in the world, much of its lithospheric structure remains unresolved. Although there were many attempts to unravel it before the 1990's, the 1991-92 experiment is the first in which modern digital broadband instruments were deployed on the plateau. Therefore, the Tibetan Plateau serves as an appropriate place to test the feasibility of our procedure for a region where little prior information is available. As an increasing number of similar temporary seismic deployments have been conducted recently in many tectonically interesting regions, it is expected that broadband waveform modeling will be used more extensively for various purposes. I believe that most of the techniques developed in this thesis can be easily transported to other regions.

Each chapter in the thesis is an independent unit, with its own abstract, introduction, and conclusion sections. In Chapter 2, I discuss a source estimation technique using broadband regional waveforms called the "cut and paste" (CAP) method, originally developed by *Zhao and Helmberger* [1994]. I improve the CAP method by redefining its waveform misfit error to preserve amplitude information, so that the focal depth and source mechanism can be better constrained. To demonstrate its effectiveness, I use waveform data from the TERRAscope network of southern California where earthquake locations are relatively well determined from a dense short-period seismic network and the structure is more-or-less well understood.

The remaining chapters focus on the Tibetan Plateau. In Chapter 3, a short introduction to its tectonic evolution and several plateau uplift models are presented, followed by a brief review of seismic observations and results prior to the 1991-92 experiment. I use regional earthquake data obtained during the experiment to derive

an average 1-D crustal velocity model. Because event locations in Tibet from the global earthquake catalog are not always reliable, the earthquakes are first relocated using a relocation algorithm that does not require a prior velocity model. The 1-D model is based on the travel times of various regional phases. In addition, modeling waveforms of regional Love waves provides constraints on the shallow part structure of the 1-D model.

After the 1-D model is established, the source mechanisms and depths of 62 earthquakes in Tibet and surrounding areas are determined, using the technique developed in Chapter 2. Most of the events are found to occur in the upper crust, between 5 and 15 km. However, I also find three sub-crustal earthquakes beneath southern Tibet. These three events are discussed in detail in Chapter 4.

The lateral structural variation of the crust and upper mantle are investigated in the last three chapters using teleseismic waveform data. Compared to regional waves, teleseismic waves have higher lateral resolution because of their steep incidence angles as they approach stations. A drawback is their poor vertical resolution, but some features in teleseismic waveforms can be used to alleviate this problem. Specifically, as teleseismic waves impinge on the crust, P-to-S or S-to-P conversions will occur at the crust-mantle boundary (Moho). These converted phases provide sampling paths within the crust and so they can help to separate crustal velocity anomalies from upper mantle anomalies.

In Chapter 5, I use the teleseismic receiver function method to estimate crustal thickness and Vp/Vs ratio at each individual station. Teleseismic P and S arrival time delays are also measured accurately using a multi-channel correlation technique. The result shows that, despite the uniform surface topography and small gravity anomaly within the plateau, there is a tremendous crustal thickness variation coupled with crustal and upper mantle velocity variation between northern and southern Tibet.

Detailed waveform modeling for laterally varying structures is carried out in Chapters 6 and 7. In Chapter 6, modeling the azimuthal variation of receiver functions of three stations in northern Tibet reveals a mid-crustal low S velocity layer with

its upper boundary dipping 20° to 30° to the south. The dipping structure causes a systematic azimuthal variation of both radial and tangential receiver functions. The most dramatic distortion of teleseismic P waveforms by lateral structural variation, presented in Chapter 7, occurs at the northernmost station, TUNL, which is located on the boundary between the plateau and the Qaidam Basin. Modeling the three-component waveforms indicates that there is a 15 to 20 km offset of the Moho over less than 5 km laterally. Such a sharp and large Moho relief under the margin of the plateau provides important constraints on dynamic models of continental collision and plateau uplift.

Chapter 2

Advancement in Source Estimation Techniques Using Broadband Regional Seismograms

2.1 Abstract

One important constraint on source retrieval from regional seismograms comes from the amplitude difference between various phases (such as Pnl/surface wave, SV/SH). Because the misfit errors used in some waveform inversions are normalized by the data and synthetics, the amplitude information in the data has not been fully utilized. In this chapter, we modify the "cut and paste" source estimation technique [*Zhao and Helmberger*, 1994] by removing this type of normalization. It is shown that the modified method increases the stability and resolution of the inversion. When multiple stations at different distance ranges are used, a distance scaling factor is introduced to compensate for the amplitude decay with distance. By applying the technique to the TERRAscope data, we have determined source mechanisms and depths of 364 southern Californian events with $M_L \geq 3.5$. The amplitude decays with distance are $r^{1.13}$ for Pnl, $r^{0.55}$ for Love waves, and $r^{0.74}$ for Rayleigh waves. In contrast to generally shallow source depths reported by the southern California short-period network, the depth distribution from waveform inversion shows a strong peak around 10 km with few earthquakes occurring above 5 km or below 20 km.

2.2 Introduction

Significant progress has been made recently in retrieving source mechanisms from regional broadband seismograms. A consequence is that the magnitude threshold of events that can be analyzed has been lowered to less than 4. Because of the frequent occurrence and relatively simple source functions of earthquakes in the magnitude range of 3 to 5, their waveforms are ideal for investigating regional structures, which is of great importance for delineating fault structures and understanding path effects for ground motions from large earthquakes.

Two kinds of regional waveform data are typically used for source estimation; surface waves [*Patton*, 1980; *Patton and Zandt*, 1991; *Thio and Kanamori*, 1995] and body waves [*Wallace and Helmberger*, 1982; *Fan and Wallace*, 1991; *Fan et al.*, 1994; *Dreger and Helmberger*, 1993]. Generally, body waves are less affected by shallow heterogeneities and are more stable than surface waves, although they have a lower signal-to-noise ratio due to their smaller energy. There have been several inversion methods proposed recently using whole waveforms of seismograms [*Walter*, 1993; *Ritsema and Lay*, 1993; *Zhao and Helmberger*, 1994; *Nabelek and Xia*, 1995]. Most of these inversions are mainly controlled by surface waves, particularly because they are performed using long-period waveforms. An exception is the "cut and paste" (CAP) method of *Zhao and Helmberger* [1994] which breaks broadband waveforms into *Pnl* and surface wave segments and inverts them independently. The source mechanism is obtained by applying a direct grid search through all possible solutions to find the global minimum of misfit between the observations and synthetics, allowing time shifts between portions of seismograms and synthetics. One of the advantages of the technique is that it proves insensitive to velocity models and lateral crustal variation.

Because the misfit errors defined in *Zhao and Helmberger* [1994] and others [*Wallace and Helmberger*, 1982; *Fan et al.*, 1994] are normalized by the data and synthetics, the amplitude information in the data has not been fully utilized to constrain the source orientation and depth. The purpose of this chapter is to strengthen the CAP technique by removing this normalization and allowing better use of amplitude

information. As multiple stations at different distance ranges are often used in source inversion, we will also investigate the amplitude decay with distance range for different crustal phases and correct them by introducing a distance scaling factor. Some applications of the modified technique to southern California regional earthquakes are presented.

2.3 Source Estimation Using True Amplitude Waveforms

Let $u(t)$ be the observed displacement. The corresponding synthetic displacement $s(t)$ for a double-couple source can be expressed as

$$s(t) = M_0 \sum_{i=1}^{3} A_i(\phi - \theta, \delta, \lambda) G_i(t), \tag{2.1}$$

here, $i = 1, 2, 3$ corresponds to three fundamental faults, i.e., vertical strike-slip, vertical dip-slip, and 45° dip-slip. G_i's are the Green's functions, A_i's are the radiation coefficients, and ϕ is the station azimuth. M_0 is the scalar moment, θ and δ are the strike and dip of the fault plane, and λ is the rake of the slip on the plane. They are the source parameters that we want to determine from the equation

$$u(t) = s(t) = M_0 \sum_{i=1}^{3} A_i(\phi - \theta, \delta, \lambda) G_i(t). \tag{2.2}$$

Since there are only limited unknown parameters and all of them are limited to a range of values ($0 \leq \theta \leq 2\pi, 0 \leq \delta \leq \frac{\pi}{2}, 0 \leq \lambda \leq 2\pi$), it is convenient to solve the above non-linear equation by a grid search method. We define an object function to measure the misfit error between u and s and search through the parameter space to find the global minimum of the object function.

In *Zhao and Helmberger* [1994], the misfit error is defined as the norm ($L1$ or $L2$)

of the difference between u and s normalized by the norms of both u and s:

$$e = \frac{\| u - s \|}{\| u \| \cdot \| s \|}. \tag{2.3}$$

Because Pnl usually has smaller amplitude than surface waves, this normalization helps to weight Pnl and surface waves equally. It also prevents the inversion from being completely dominated by the strongest station, which is usually the nearest station, if several stations at different distance ranges are used. However, the amplitude information is lost during the normalization. Some of this information, such as amplitude ratios of Pnl-to-surface waves and SV-to-SH, provide important constraints on the source orientation and depth. A more severe problem with this normalization is that it introduces singularities in the source parameter space at those points where source orientation generates nodal synthetics (where the norm of synthetics vanishes). In the case when data include nodal records, the grid search will miss the true minimum.

As an example, Figure 2.1A shows the misfit error as defined by (2.3) as a function of dip and rake (the location of the event and the waveforms are displayed in Figure 2.2). The global minimum is very obscure. The error surface is distorted by some peaks and ridges which are associated with singularities introduced by the normalization. Figure 2.1B is the misfit error using true amplitudes without normalization

$$e = \| u - s \| . \tag{2.4}$$

It has a well defined global minimum at $\delta = 60°$, $\lambda = -10°$. Note that the $P-SV$ waves at stations PFO, GSC, and ISA are close to nodal (Figure 2.2), which are well matched by the synthetics of solution B. However, the synthetics of solution A have larger $P - SV$ amplitudes compared with the data. This particular example of waveform modeling exposes the difficulties encountered at nodes. Since the $P-SV$ motions are near nodal to the north, the radial and vertical components are easily contaminated by SH motions (see reference lines in Figure 2.2). Only the PAS observations display

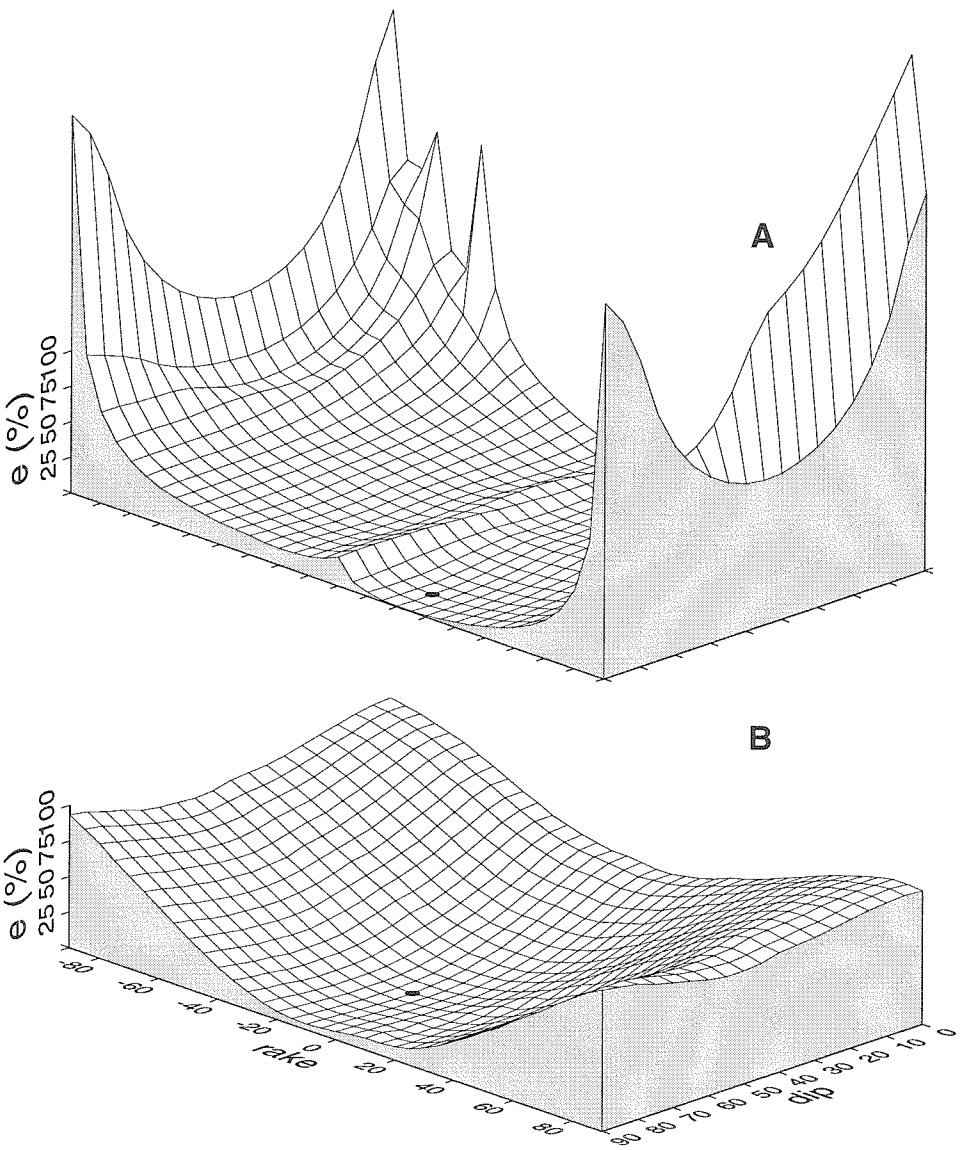

Figure 2.1: Waveform misfit errors as a function of dip and rake for a southern California event (May 24, 1992, 12:22UTC). A) The misfit error using normalization (expression (2.3) in the text), solution is: θ=70°, δ=80°, λ=20°, M_w=3.9, h=14 km. B) The misfit error using the true amplitude of the recorded waveforms (expression (2.4)), solution is: θ=245°, δ=60°, λ=-10°, M_w=3.9, h=17 km. The global minima from the grid search are indicated by the black dots.

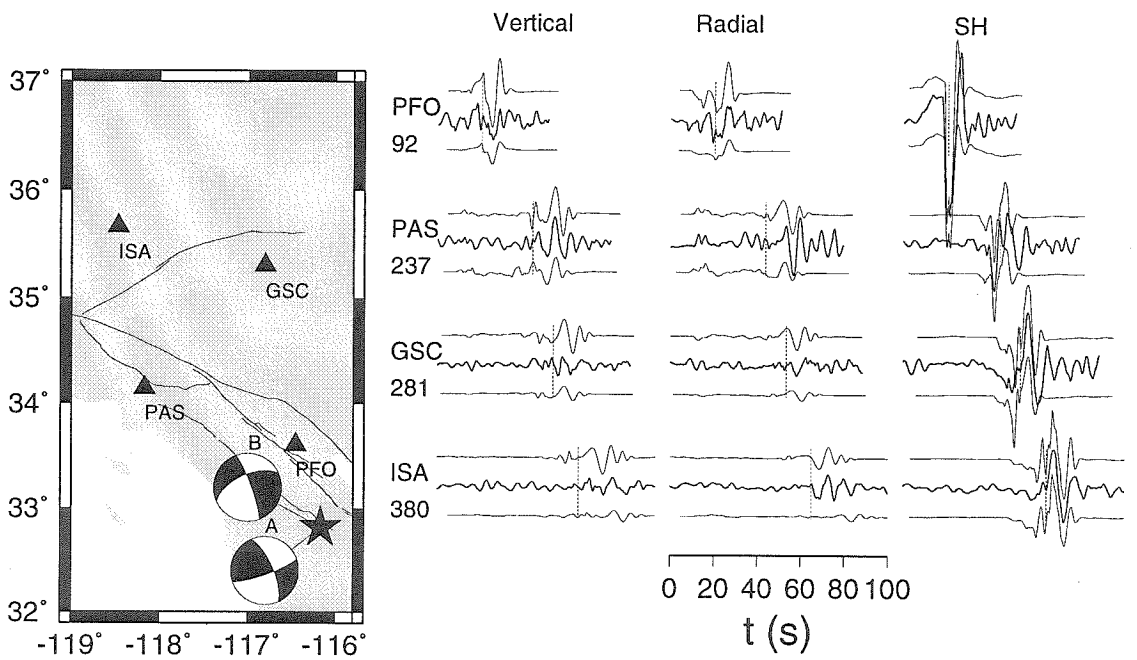

Figure 2.2: The location of event (star) used in Figure 2.1. The focal spheres correspond to the solution A and B in Figure 2.1 and their synthetics are plotted above (solution A) and below (solution B) the data trace. Reference lines are arrivals of Love waves as determined from the tangential components. Numbers below the station names are epicentral distances in km.

a true Rayleigh wave with the expected time lag behind the Love wave. The "cut and paste" aspect of the inversion with amplitude normalization moves the synthetic Rayleigh wave forward attempting to capture some of this energy (see ISA). The modified method tends to suppress such spurious attempts.

2.4 Distance Range Scaling

Using true-amplitude waveforms for source inversion usually leads to the problem of the closest station dominating the inversion when stations are distributed over a large distance range. Figure 2.3 shows misfit errors as a function of distance. These misfit errors were obtained through a global search applying expression (2.4) to 364 southern Californian regional events of $M_L \geq 3.5$. The Standard southern California crustal model (SC model [*Dreger and Helmberger*, 1993, see]) was used in the inversion.

The misfits of surface waves have larger scatter than the misfits of body waves, which is expected because surface waves are more easily affected by shallow heterogeneity. It has been shown that *Pnl* at the range of 300 km to 1000 km is quite stable [*Helmberger and Engen*, 1980] and easily inverted for source mechanisms [*Wallace and Helmberger*, 1982]. At closer range, the details of the Moho transition play a more important role as well as the PL waves trapped in the shallow crust [*Song et al.*, 1996]. Since both of these features show strong local variation, we should expect the large scatter displayed in Figure 2.3 at closer distances. However, because the *Pnl*'s at the nearest stations play an essential role in early warning [*Scrivner and Helmberger*, 1995], the local velocity structure should probably be added to each station. This approach will be pursued in future efforts.

Despite the scatter in Figure 2.3, the misfit errors show a rapid decay with distance. Since the effects of the radiation patterns have been taken out, this decay is related to the amplitude decay due to geometrical spreading and attenuation. To compensate for this decay, we introduce a distance range scaling factor and define the

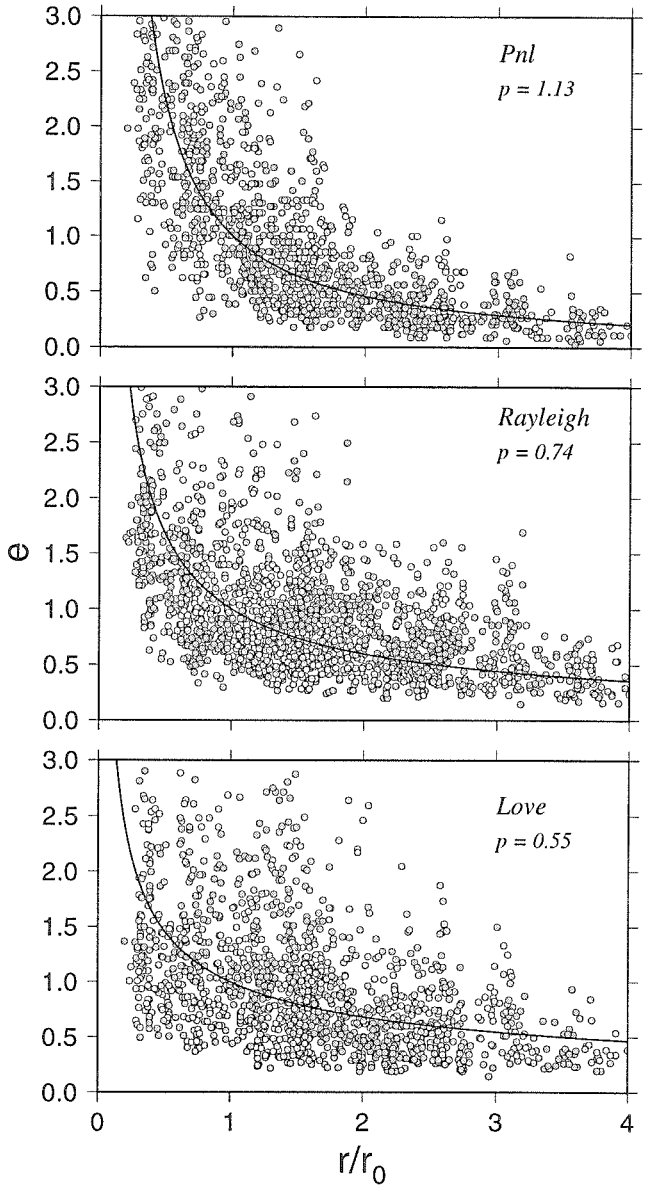

Figure 2.3: Misfit errors of different portions of seismograms of 364 southern California events. True amplitude waveforms are used in the inversion. We chose $r_0 = 100$ km as reference distance. The solid lines are $(\frac{r_0}{r})^p$ where the p values are determined from a least-square fit.

misfit error for a record at a distance r as

$$e = \| (\frac{r}{r_0})^p \| \cdot \| u - s \|; \tag{2.5}$$

where p is a scaling factor to give the record at r the same weight as that at a reference distance r_0. If we assume a spherical geometrical spreading for body waves and cylindrical geometrical spreading for surface waves, an appropriate choice of p would be 1 for body waves, and 0.5 for surface waves. For southern California, the p values determined from Figure 2.3 are 1.13 for *Pnl*, 0.55 for Love waves, and 0.74 for Rayleigh waves. The scatter in the figure is large especially at the smaller distances, suggesting considerable variation in local structure and the need for regionalization. Nevertheless, it appears that the p values derived from geometrical spreading are reasonably good for the period range (5 to 100 s) used in the waveform inversion.

2.5 Applications

Because there is essentially no manual intervention required for this technique, it can be fully automated. We have implemented it using data from TERRAscope. As soon as a regional event larger than 3.5 occurs, the preliminary event location is used to trigger the code to invert for the source mechanism using real-time waveform data. Usually it takes 3 min on a SUN-SPARC 10 workstation for the code to complete a 10° spacing grid search while fixing the source depth. If needed, the best focal depth can be determined through an additional iteration in a range of depths.

We present the recent Ridgecrest earthquake in southern California as an example (Figure 2.4). This event, which occurred on September 20, 1995, is the largest (M_L 5.8) since the 1994 Northridge earthquake. The best solution of the waveform inversion gives an almost purely strike-slip mechanism with one nodal plane striking N30°W. This mechanism is consistent with the first-motion focal mechanism [*Hauksson et al.*, 1995]. To give an estimate of uncertainty of the solution, we plot misfit error as a function of depth (Figure 2.4B) and contours of misfit values around the

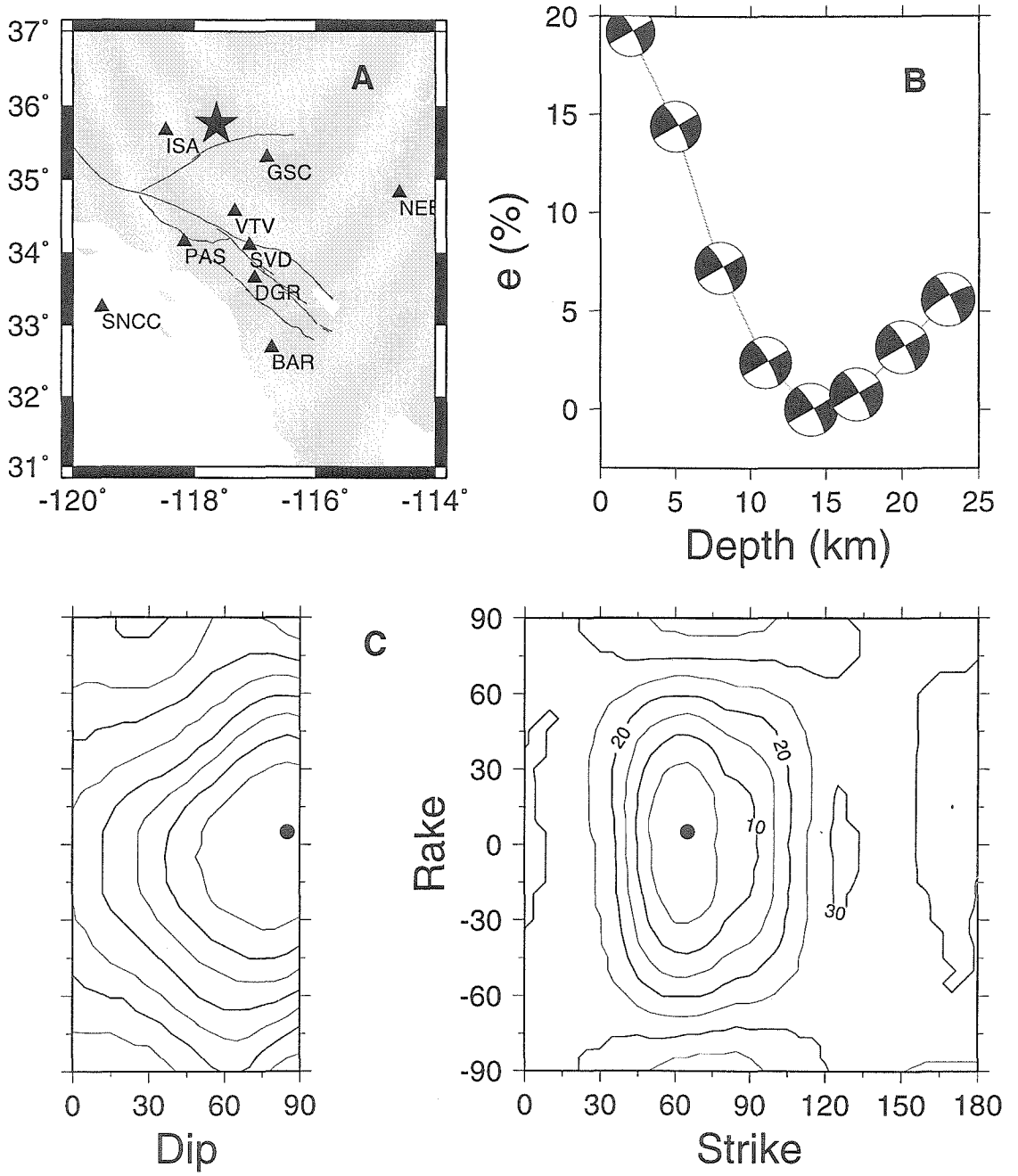

Figure 2.4: A) Map containing the location of September 20, 1995, Ridgecrest event (star) and the recording TERRAscope stations; B) Misfit errors as function of depth; C) Contours of misfit errors around the best solution (indicated by the black dot).

Figure 2.5: Comparison of data (heavy traces) with synthetics of solution at a depth of 5 km (upper traces) and 14 km (lower traces) for the Ridgecrest event. The numbers below station names are epicentral distances in km. True amplitudes are preserved with distance scalings. Vertical and radial components of surface waves are amplified by a factor of 2 with respect to the tangential for display reason.

best solution (Figure 2.4C). They show that the strike is the well-defined (within ± 10°) while the rake and dip are less well constrained (± 30°). The best focal depth of 14 km determined from the inversion is deeper than the 5 km depth listed in the Southern California Seismographic Network (SCSN) catalog. Figure 2.5 shows a comparison of data with synthetics for the best solutions at the depths of 5 and 14 km. Note that all the TERRAscope stations except NEE show strong SH components and weak vertical and radial components because most of them are close to the $P - SV$ nodal directions for this event (Figure 2.4A). The synthetics match the observations well both in shape and amplitude. This indicates that the amplitude adjustment with distance scaling is about correct and that the Green's functions are satisfactory. For all stations except DGR, the synthetics with the deeper focal depth fit the data better. Some paths cause difficulties, such as the path to SNCC (San Nicolas Island). Some stations also show complexities such as the large apparent Rayleigh motions arriving on the tangential component at PAS. Fortunately, good station coverage overwhelms these types of misfits.

We have applied the technique to all available regional events of $M_L \geq 3.5$ recorded by TERRAscope back to 1990. A total of 364 focal mechanism solutions are obtained (see Appendix D). Although a large number of them are aftershocks of the 1992 Landers and 1994 Northridge earthquakes, the data set still gives a good sampling of active source regions in southern California (Figure 2.6). Figure 2.7 is the comparison of inverted focal depths and M_0 with the depths and M_L from the SCSN catalog. M_0 vs. M_L essentially follows the relation found by *Thatcher and Hanks* [1973]. However, the waveform inverted depths are generally deeper than the catalog depths. We will discuss this in the next section.

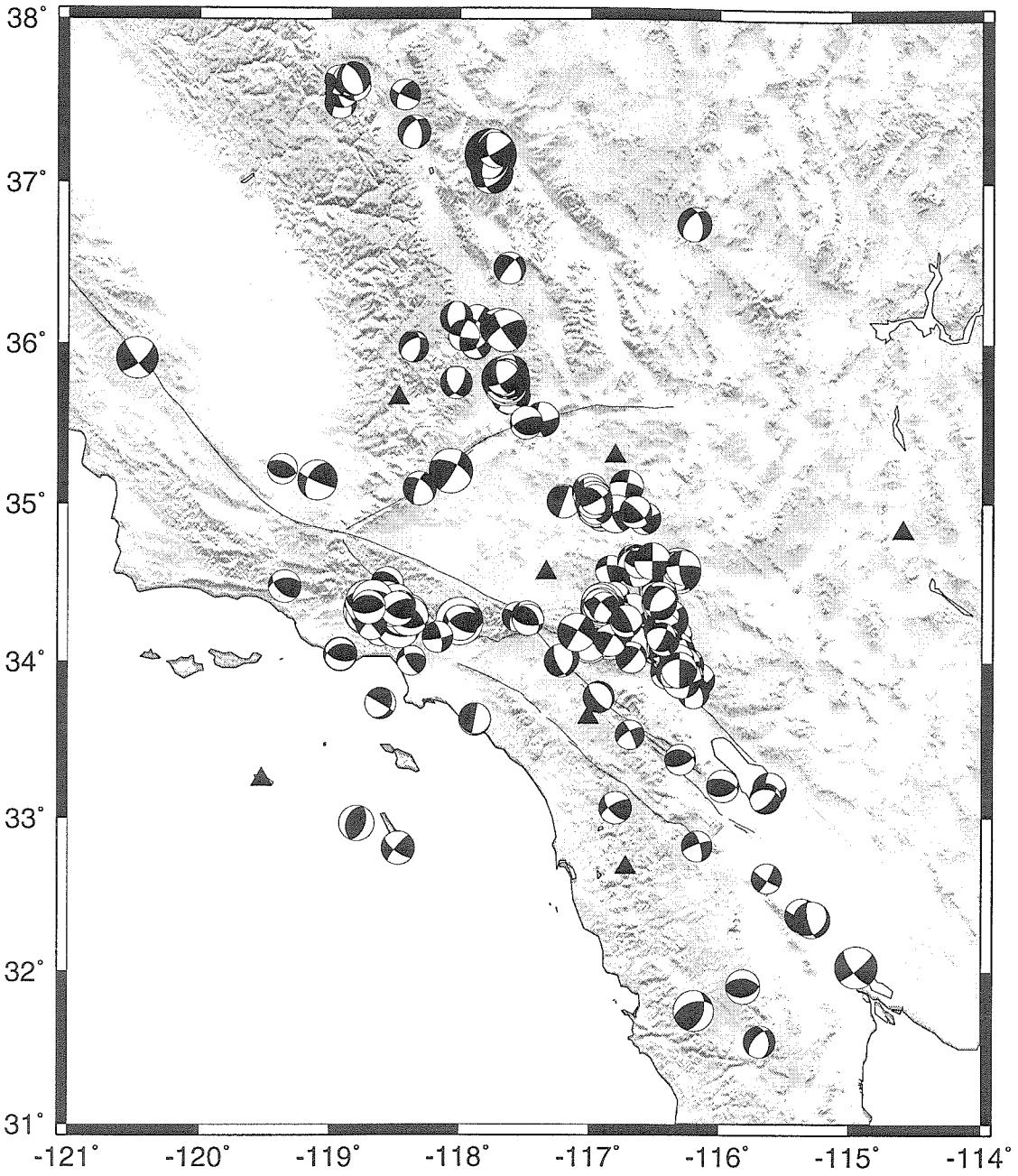

Figure 2.6: Focal mechanisms determined from the waveform inversion of 364 regional events (see text). The sizes of the focal spheres are proportional to M_w.

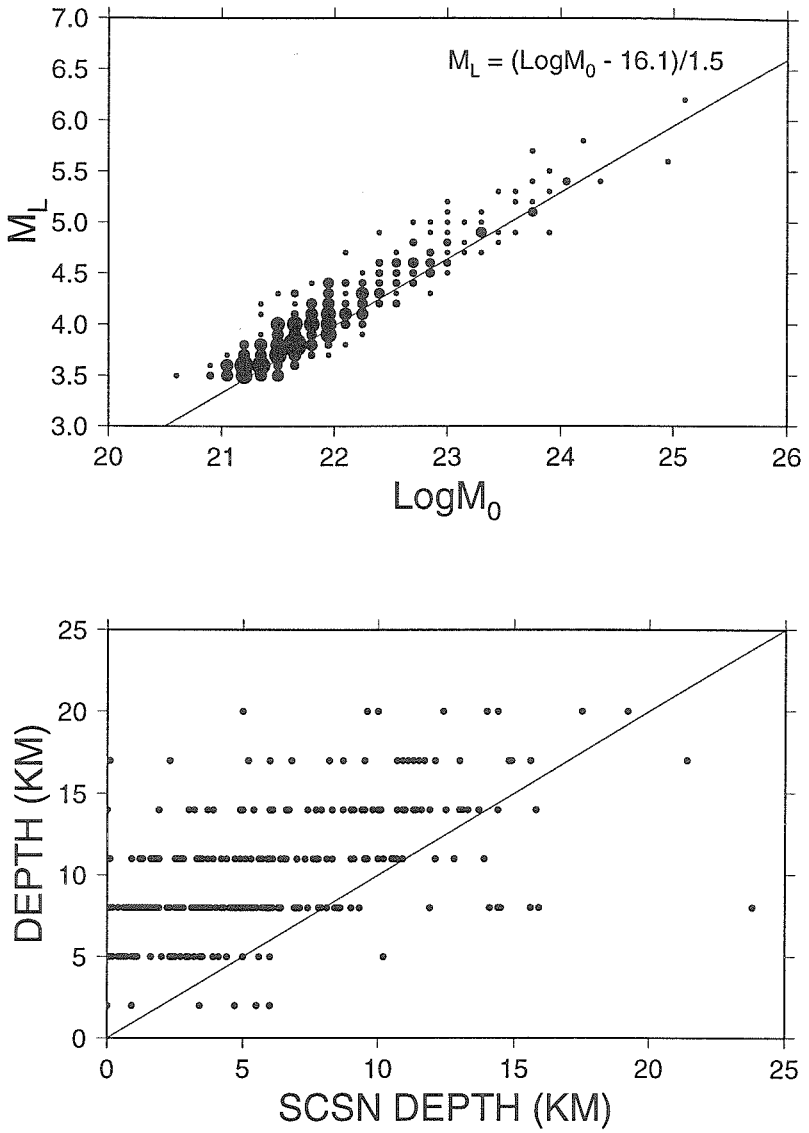

Figure 2.7: Upper panel displays the SCSN catalog M_L vs. M_0 determined by the waveform inversion. These results can be compared against the relation determined by *Thatcher and Hanks* [1973]. Lower panel contains the depths estimated from the waveform inversion vs. the SCSN catalog depths.

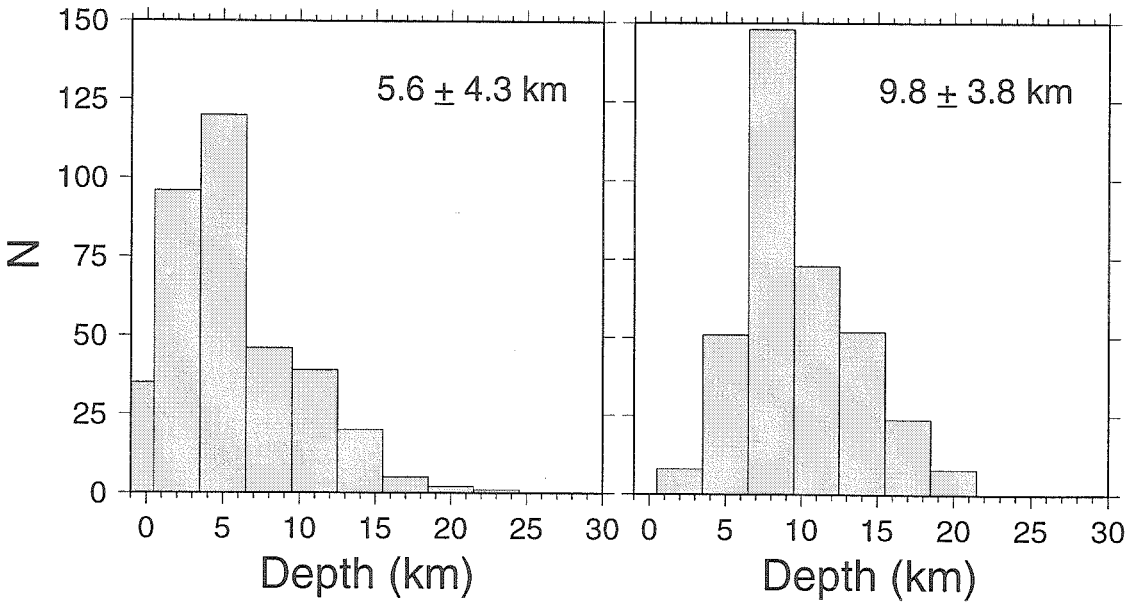

Figure 2.8: Histograms of earthquake depth distribution in southern California, Left panel: SCSN catalog depths; Right panel: waveform inverted depths. The numbers in the figure are the average focal depths and the standard deviations.

2.6 Focal Depth Distribution and the Seismogenic Zone in Southern California

Figure 2.8 shows the histograms of SCSN catalog depths and waveform inversion depths for the 364 events included in this study. The catalog depths are determined from the P arrival times as recorded by the southern California short-period network. Large uncertainty exists for these routinely determined depths, mostly caused by the trade-off between depth and origin time, and in some cases also sparse station distribution. The most accurate information on depth distribution of seismicity is usually obtained from aftershock sequences during which temporary stations are deployed directly above the mainshock rupture. However, the interpretation of aftershocks can be complicated because the mainshock greatly changes the local stress field. Preshocks and background events probably provide a more accurate picture of the evolving stress field. Since our waveform inversion technique conserves the amplitude information among various crustal phases, source depths should be well constrained, even for small magnitude earthquakes.

The depth distribution obtained from waveforms inversion shows a strong peak at about 10 km with few events occurring above 5 km or below 20 km. This seems quite compatible with the expected seismogenic zone for a tectonically active region as southern California. It is generally thought that the lower boundary of the seismogenic zone is due to a transition from brittle to ductile behavior in continental crust [*Meissner and Strehlau*, 1982; *Sibson*, 1984; *Doser and Kanamori*, 1986]. The top of the seismogenic zone is controlled by a transition from stable sliding to stick slip, which can be attributed to the presence of unconsolidated fault gouge [*Marone and Scholz*, 1988]. For a region overlain by sedimentary structures of unconsolidated material and with well-developed faults, they predict a minimum source depth of 3 to 5 km, which agrees well with our results.

This 1-D picture of seismicity is obviously over-simplified in that there are well-known deep seismic zones (e.g., ANZA network) and shallow seismic zones (e.g., Imperial Valley). There is also considerable evidence for 2-D and 3-D structures which are causing much of the scatter seen in Figure 2.3. These latter features need to be incorporated in our simulation system to obtain better locations and develop the ability to recover second order source characteristics on a routine basis.

2.7 Conclusions

In summary, we have improved the CAP technique by removing the normalization in the definition of misfit error. This modification helps to fully utilize the amplitude information of three-component records to give a better constraint on source orientations and depths. It is shown that both the stability and resolution power of the inversion are increased. We also introduced a distance scaling factor to the misfit error formalism in order to compensate for the amplitude decay with distance when multiple stations at different distance ranges are used.

This technique has been fully automated and is presently servicing the TERRAscope data stream where it takes just a few minutes to estimate source parameters. In batch mode it takes a few days to re-run through the complete TERRAscope data

archive of local events. Preliminary results from such runs suggest deeper faulting activity, by 5 km on average, than obtained from the SCSN catalog. Resolution of such disagreements and local regionalization should prove much easier with this new tool.

Chapter 3

Modeling Broadband Regional Waveforms on the Tibetan Plateau

3.1 Abstract

Regional waveform data obtained by the 1991-1992 Sino-US Tibet experiment provide a unique opportunity to study the Tibetan crustal structure and earthquake sources with ray paths completely confined to the plateau. We first use 363 P arrival picks from 49 earthquakes to relocate these events, using a relocation method that does not require a prior velocity model. The relocation shows that earthquakes in Tibet are poorly located in the global earthquake catalog. After relocation, velocities of various crustal phases are estimated. High Pn velocity (8.17 km/s) and Sn velocity (4.84 km/s) are found, in contrast to low Pg velocity (6.17 km/s) and Sg velocity (3.50 km/s). Average crustal P and S velocities from the Pn and Sn intercept times are 6.25 km/s and 3.42 km/s respectively, assuming a crustal thickness of 65 km and shallow source depths. A 1-D average Tibetan crustal velocity model is developed using the above constraints plus modeling regional Love wave waveforms. Source mechanisms and depths of 62 events that occurred in the plateau and surrounding regions are determined using this model. Most earthquakes are located at depths between 5 and 15 km. The shallow seismicity cut-off depth and low crustal velocities suggest high temperatures in the lower crust. Thrust faulting source mechanisms are dominant at the margins of plateau. Within the plateau but at locations with surface elevations below 5 km, source mechanisms are a mixture of strike-slip and thrust. For areas with surface elevation higher than 5 km, all events show consistently normal faulting, which indicates that a large portion of the high plateau is under EW

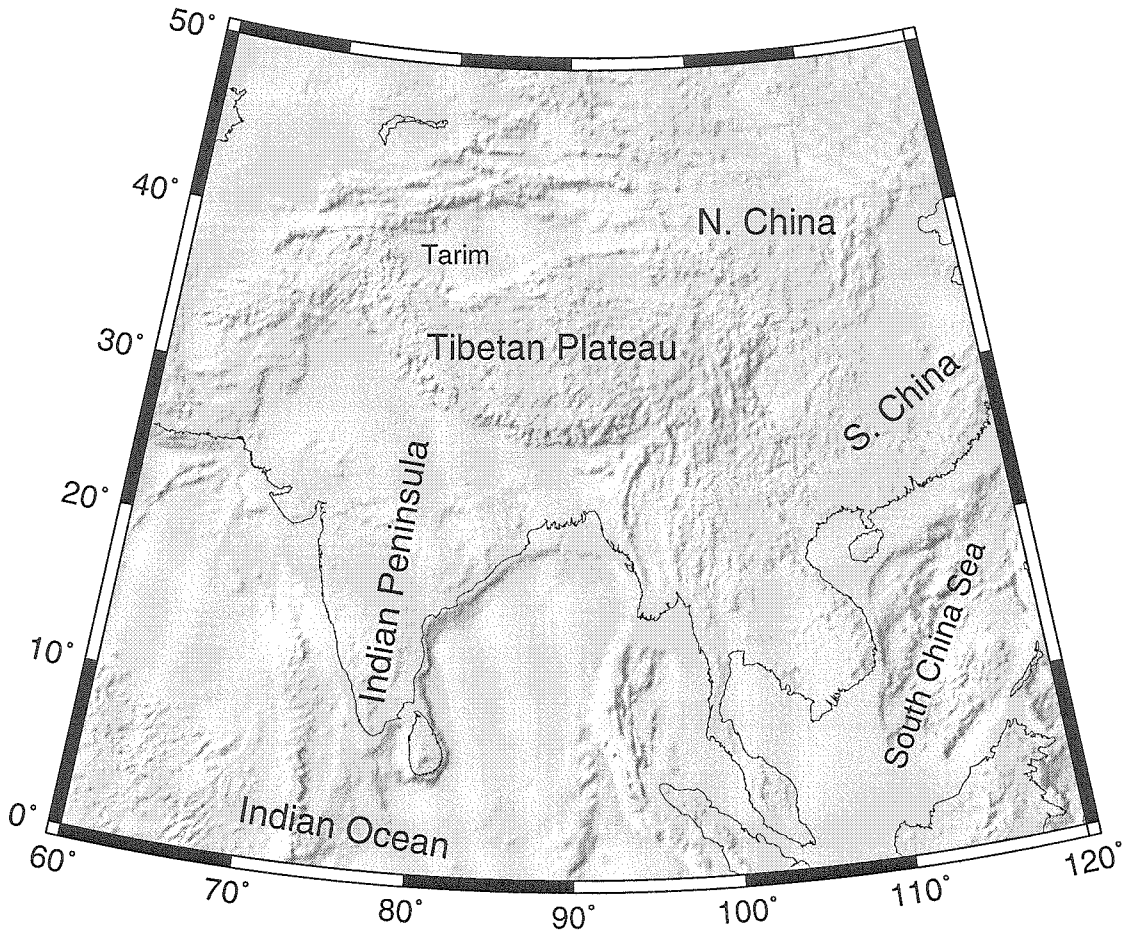

Figure 3.1: A shaded relief map of south and east Asia.

extension.

3.2 Introduction

Asia is the largest and also youngest continent on earth. A large portion of Asia was formed by accreting several continent fragments to its southern margin in the past 400 million years [*Sengor and Natalin*, 1996]. The most recently added fragment is the Indian subcontinent which collided with Asia about 45 million years ago. This collision and the following northward penetration of India into Eurasia have greatly modified the Asian tectonic framework and produced the world's largest and highest landmass, the Tibetan Plateau (Figure 3.1).

Understanding the Tibetan Plateau's tectonic evolution will contribute signifi-

cantly to our knowledge about how continents evolve over geological time. Although plate tectonics has proven quite successful in describing the kinematics of oceanic plates, theories for continental plates have not yet been well established. In this respect, the Tibetan Plateau provides a natural laboratory to test various hypotheses. There have been many attempts to unravel deep structures of the plateau and surrounding areas since the 1960's. Most of them used seismic observations. Because of the remoteness and extreme environment of Tibet, early seismic studies had to rely on data recorded outside the plateau, which greatly limited the accuracy and reliability of results.

In 1991 and 1992, a PASSCAL passive seismic recording experiment was conducted on the plateau by research groups from the Institute of Geophysics, State Seismological Bureau of the People's Republic of China, the University of South Carolina, and the State University of New York at Binghamton [*Owens et al.*, 1993]. For the first time, 11 broadband digital seismic stations were deployed along and east of the Lhasa–Golmud highway (Figure 3.2 and Table 3.1). Except for station TUNL where a Guralp sensor was installed, the other ten stations were all equipped with STS2 sensors. Each station records ground motion in a continuous mode of 5 samples per second (SPS) and a triggered mode of 40 SPS. The experiment lasted for a year, from July 1991 to July 1992. The large amount of high quality data from this experiment provided a unique opportunity to study the structure using stations directly above it.

In this chapter, we first give a brief introduction to the tectonic evolution of the Tibetan Plateau and several existing uplift models, followed by a short review of seismic observations and results prior to the experiment. We use regional earthquake data to derive an average 1-D crustal velocity model for the Tibetan Plateau. This is done using travel times of various regional phases from earthquakes within the plateau and modeling their Love wave waveforms. After the 1-D model is established, source mechanisms and depths of 62 earthquakes in Tibet and surrounding regions are determined using the technique we developed in Chapter 2. Their implications for the tectonics of the Tibetan Plateau will also be discussed.

Table 3.1: Station locations of the 1991-1992 Sino-US Tibet experiment

Station	Latitude	Longitude	Altitude, m
AMDO	32.246	91.686	4700
BUDO	35.530	93.913	4620
ERDO	34.518	92.707	4640
GANZ	29.780	94.064	3152
LHSA	29.703	91.128	3789
MAQI	34.478	100.248	3736
SANG	31.022	91.700	4760
TUNL	36.200	94.817	3133
USHU	33.033	97.000	3750
WNDO	33.450	91.904	4760
XIGA	29.233	88.852	3900

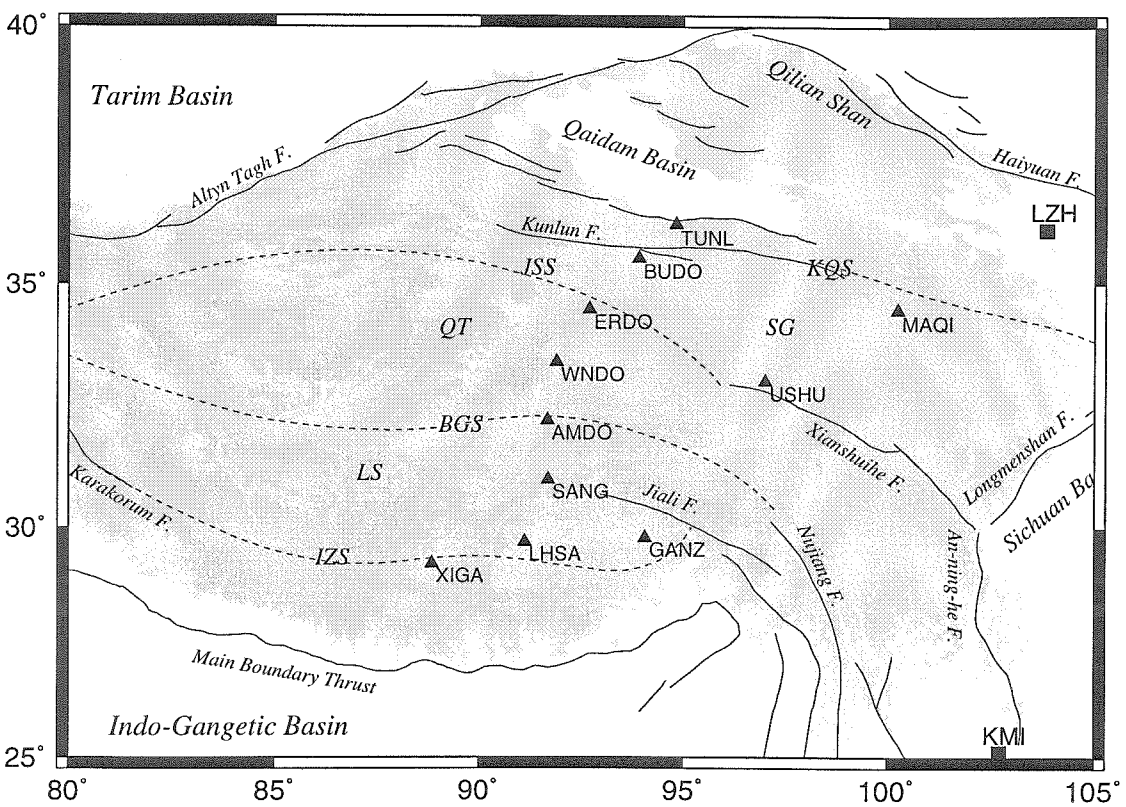

Figure 3.2: Tectonic map of the Tibetan Plateau. Areas above elevations of 3 and 5 km are shaded. Solid lines are major faults. The plateau are divided into several terranes separated by sutures (dashed lines); BGS: Bangong Suture; IZS: Indo-Zangbu Suture; JSS: Jinsha Suture; KQS: Kunlun-Qinling Suture; LS: Lhasa terrane; SG: Songpan-Ganzi terrane; QT: Qiangtang terrane. Triangles are 11 broadband stations of the 1991-92 Sino-US PASSCAL experiment. Squares are the permanent Chinese Digital Seismic Network (CDSN) stations.

3.3 Tectonic Evolution of the Tibetan Plateau and Uplift Models

The Tibetan Plateau is the youngest plateau in the world. It is estimated that the present elevation of much of the plateau was attained only 8 to 11 million years ago [*Harrison et al.*, 1992; *Molnar et al.*, 1993]. It has an areal extent of about 3×10^6 km^2 and an average elevation of 5 km (e.g., *Fielding et al.* [1994]). The plateau is surrounded by several Precambrian cratons with large-scale thrust and strike-slip faults serving as boundaries (Figure 3.2). Relief along the edges is also very sharp. Despite its uniform elevation, the plateau is actually composed principally of three terranes that were accreted successively to Eurasia during the Mesozoic Era [*Dewey et al.*, 1988]. They are, from north to south, the Songpan-Ganzi Terrane, the Qiangtang Terrane, and the Lhasa Terrane (Figure 3.2). This division is mostly based on the recognition of several ophiolite zones that are interpreted as sutures. The Songpan-Ganzi Terrane accreted to Tarim-North China along the Kunlun-Qinling Suture during the late Permian, followed by the accretion of Qiangtang Terrane to the Songpan-Ganzi Terrane along the Jinsha Suture during the late Triassic, and the Lhasa Terrane to the Qiangtang Terrane along the Bangong Suture during the later Jurassic [*Dewey et al.*, 1988]. The Qiangtang and Lhasa blocks, underlain by Precambrian continental crust, are believed to come from Gondwanaland. The Songpan-Ganzi Terrane might be an extension of the South China block [*Dewey et al.*, 1988; *Yin and Nie*, 1996].

The Indian continent collided with the Lhasa Terrane along the Indo-Zangbu Suture during the Eocene about 45 million years ago [*Molnar and Tapponnier*, 1975]. Since the collision, it has moved northward into the rest of Eurasia by about 2000 to 3000 km [*Lin and Watts*, 1988]. Although it is now widely accepted that the uplift of the Tibetan Plateau is the result of its thickened crust in response to this collision, the mechanism of thickening crust by collision is not clear. Many models have been proposed. Most of them lie between two extremes, the crustal underthrusting model and the crustal shortening model. The crustal underthrusting model, first proposed

by *Argand* [1924] and favored by many others [*Bird*, 1978; *Powell and Conaghan*, 1973, 1975; *Barazangi and Ni*, 1982], suggests that the thick Tibetan crust is produced by underthrusting the Indian crust beneath the Asian crust. This model predicts a shield-like mantle lithosphere beneath the plateau, similar to the one beneath India. The uplift would have started from southern Tibet and expanded northward. However, there is no clear evidence to support such a progressive uplift history. A variant of this model is the crustal ejection model by *Zhao and Morgan* [1985] who propose that the Indian crust was injected into a softer Asian Tibetan lower crust so the plateau would be uplifted uniformly by hydraulic pressure. On the other hand, the crustal shortening model suggests that the thick crust was formed by horizontal shortening and vertical stretching of the Asian crust [*Dewey and Bird*, 1970; *Dewey and Burke*, 1973; *England and McKenzie*, 1982; *England and Houseman*, 1986; *Dewey et al.*, 1988]. In this scenario, both the crust and mantle lithosphere of Asian Tibet were first thickened and the plateau was raised to 3 km elevation. The thickened mantle lithosphere was later removed by a thermal instability or convection, which increased the surface elevation to 5 km [*England and Houseman*, 1986; *Dewey et al.*, 1988].

Because different models predict different crustal and upper mantle structures, seismic observations and results can play a crucial role in resolving these debates. Before the 1991-92 PASSCAL experiment, many seismic studies used surface waves propagating across the plateau to measure their group and phase velocities and invert for 1-D velocity structures [*Romanowicz*, 1982; *Jobert et al.*, 1985; *Brandon and Romanowicz*, 1986]. Others used *Pn* and *Sn* travel times to estimate velocities in the uppermost mantle [*Chen and Molnar*, 1981; *Barazangi and Ni*, 1982]. There were also several deep seismic sounding profiles in southern and central Tibet by Chinese and French scientists [*Teng et al.*, 1983; *Hirn et al.*, 1984b, a; *Lu and Wang*, 1990]. Upper mantle structure down to 400 km beneath the plateau was investigated using *S* waves in the distance range of 15° to 30° [*Lyon-Caen*, 1986; *Zhao et al.*, 1991]. The results from these studies have been summarized by *Molnar* [1988]. In general, all of them show a thick crust (50 to 80 km) with high *Pn* and *Sn* velocities of 8.1 to

8.4 km/s for Pn and 4.6 to 4.8 km/s for Sn. The average velocities of lithospheric mantle are low, particularly under north-central Tibet. Many studies also emphasize lateral variation. For example, surface wave studies indicate a thinner crust in north-central Tibet. Strong attenuation of high-frequency Sn exists in the same region [*Ni and Barazangi*, 1983].

3.4 Event Relocation and Travel Time Analysis

During the one year experiment, about 100 earthquakes listed in the International Seismological Centre (ISC) Bulletin were recorded by the array with distances less than 1000 km (Figure 3.3). For the purpose of deriving a 1-D average velocity model for the plateau, we exclude events that are outside the plateau to avoid possible path contamination. 49 earthquakes are selected which all have at least 4 stations recorded with clear P onsets.

One advantage of having broadband waveform records is that many crustal phases can be identified based on their amplitude and frequency characteristics. As an example, Figure 3.4 shows the record section for one of the events, Event 222 (see Figure 3.3). This event occurred in the middle of the north-south linear array between ERDO and WNDO, so its record section forms a natural seismic profile. We can see that the long-period Moho head waves, Pn and Sn, arrive before the direct arrivals (Pg and Sg) beyond a distance of about 320 km (Figure 3.4). Such a large cross-over distance between the direct waves and down-going waves confirms a thick crust.

We hand-pick first P and S arrivals on vertical and tangential components of records for all 49 events, which gives 363 P picks and 267 S picks. Their travel times vs. epicentral distances are plotted in Figure 3.5A. The large scatter is mostly attributed to the unreliable locations and origin times in the ISC catalog. The magnitudes of these events are less than 5, so the number of station reports used by the ISC location is very limited. The abnormal crust of Tibet also causes bias in the ISC event origin times. Therefore, relocating these events is necessary before further travel time analysis can be applied.

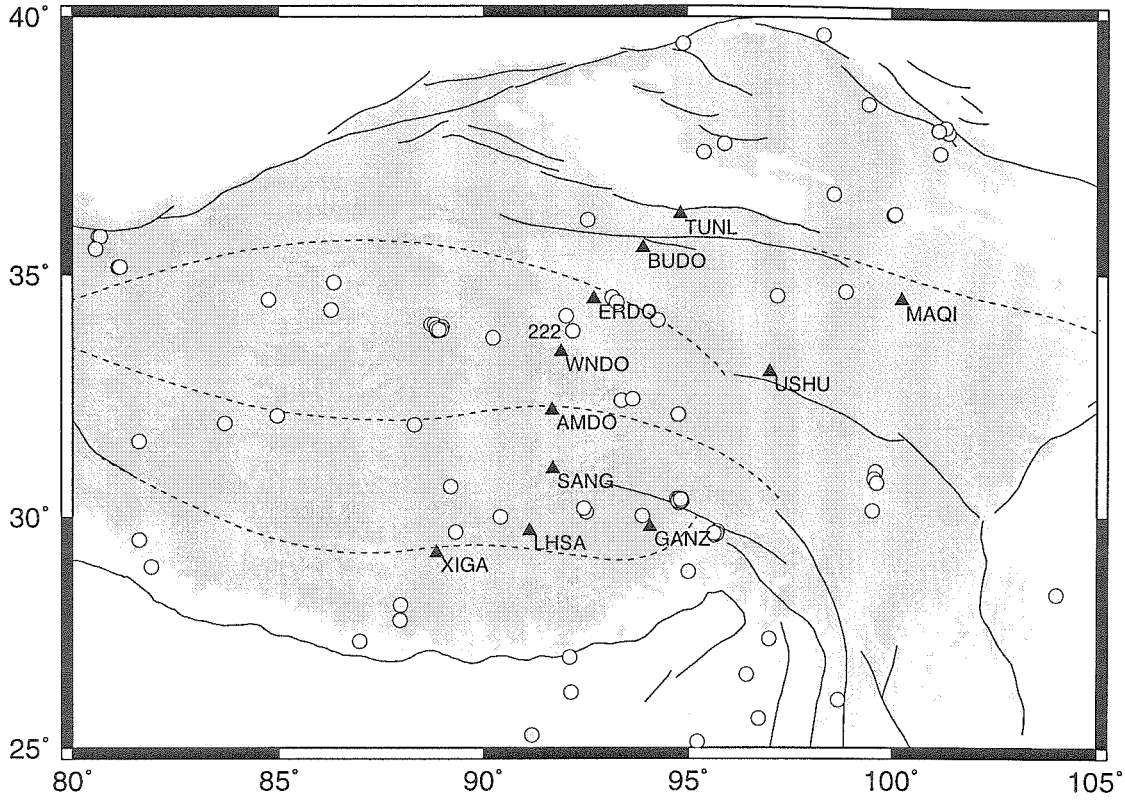

Figure 3.3: The ISC locations of earthquakes (circles) recorded by the 1991-92 PASSCAL experiment in Tibet and surroundings.

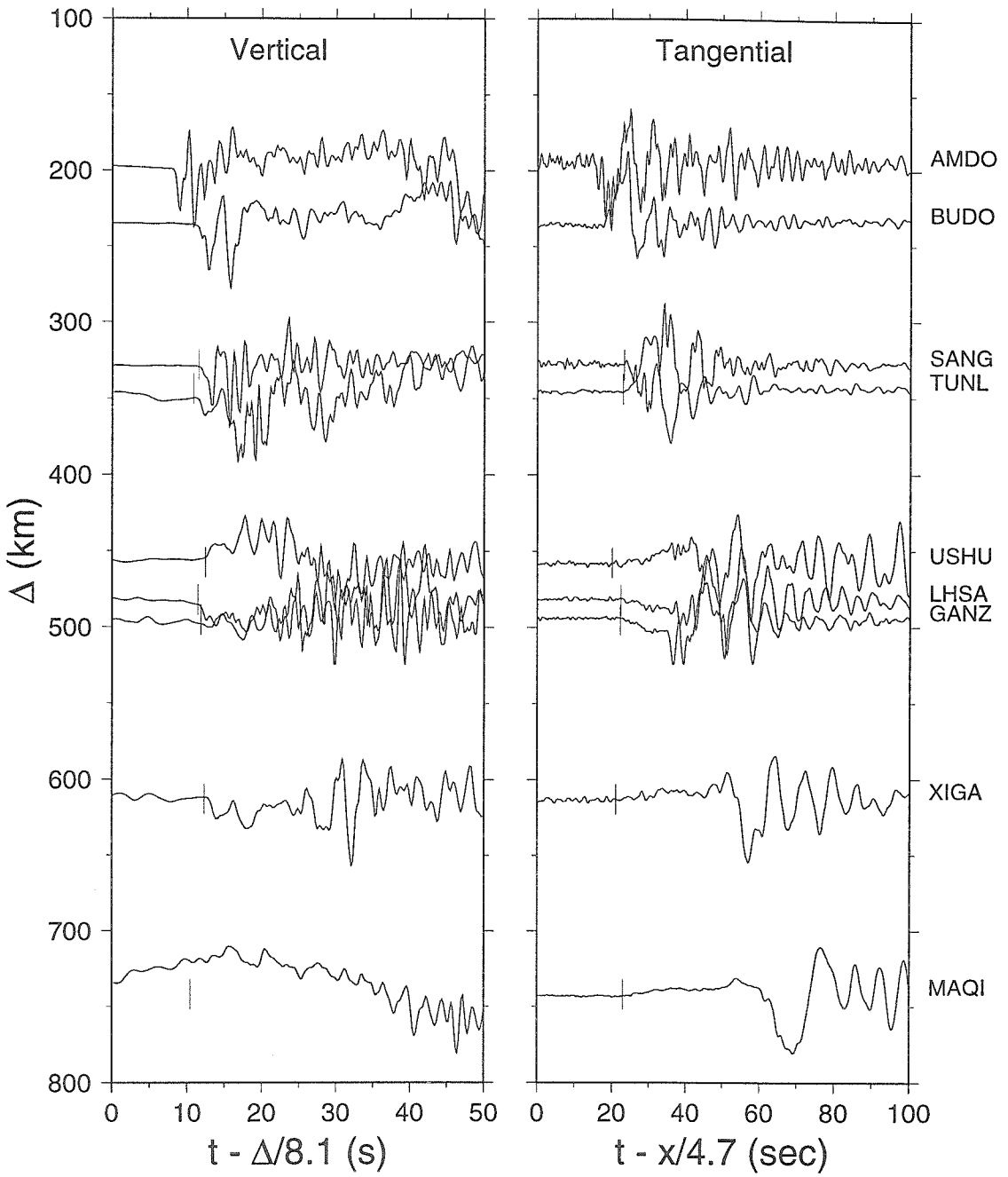

Figure 3.4: Distance profiles of displacement records of Event 222 (location shown in Figure 3.3). Vertical lines show the Pn and Sn arrivals.

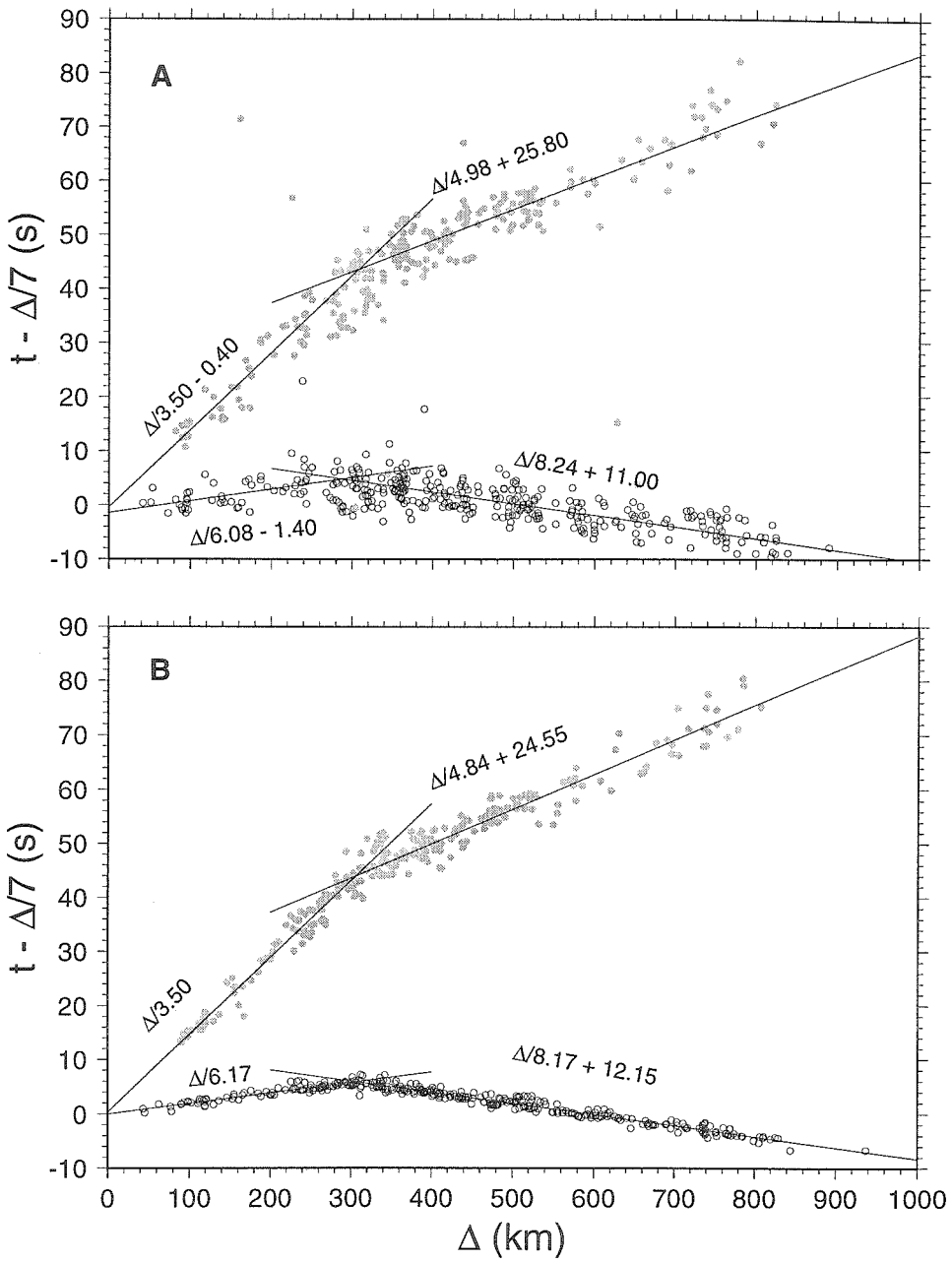

Figure 3.5: (A) first P (open circles) and S (gray dots) arrival times as a function of epicentral distance using the ISC source locations and origin times. (B) travel times after relocation. Velocities of Pn, Pg, Sn, Sg from the relocation are presented next to their branches.

There are several crustal velocity models that could be used for the relocation, such as M45 [*Romanowicz*, 1982] or TIP [*Zhao et al.*, 1991]. However, we prefer relocating these events without using any prior velocity model to avoid bias because the travel time data will be used later to derive a velocity model.

We developed a simple but effective relocation method which does not require a prior velocity model. Assuming a one-layer crustal velocity model, the first arrival time at station i from event j satisfies

$$t_{ij} = \begin{cases} p_n \Delta_{ij}(x_j, y_j) + t_n^0 + o_j & \text{if } \Delta_{ij} > \Delta_c \\ p_g \Delta_{ij}(x_j, y_j) + t_g^0 + o_j & \text{if } \Delta_{ij} < \Delta_c, \end{cases} \tag{3.1}$$

where x_j, y_j, and o_j are the longitude, latitude and origin time of event j; p_n and p_g are the apparent slownesses for Pn and Pg, and t_n^0 and t_g^0 are the intercept times; Δ_{ij} is the epicentral distance and Δ_c is the cross-over distance. The event relocation is formulated as an optimizing problem: find the best (x_j, y_j, o_j) that minimizes the difference between observed and predicted travel times. Note that both event parameters (x_j, y_j, o_j) and velocity model parameters (p_n, t_n^0, p_g, t_g^0) are unknown. The problem is solved in two steps. First, using the ISC locations and origin times as the initial values of (x_j, y_j, o_j), model parameters (p_n, t_n^0, p_g, t_g^0) can be obtained by solving the above linear equations. Then we fix the velocity model parameters and look for "the best" event locations. This is done using a grid search surrounding the ISC locations, starting from the event with the largest *rms* travel time residual. The procedure is repeated until a convergence is reached. This technique does not require a prior velocity model but assumes that all events are located at the same depth. Since parameter o_j trades off with source depth, depth difference between events are absorbed into the origin time. Besides, there is evidence that most earthquakes in Tibet occur at depths between 5 and 20 km [*Molnar and Chen*, 1983; *Zhao and Helmberger*, 1991].

The relocation result is listed in Table 3.2. Figure 3.6 shows their new locations and offsets with respect to the ISC locations. An encouraging sign about the relo-

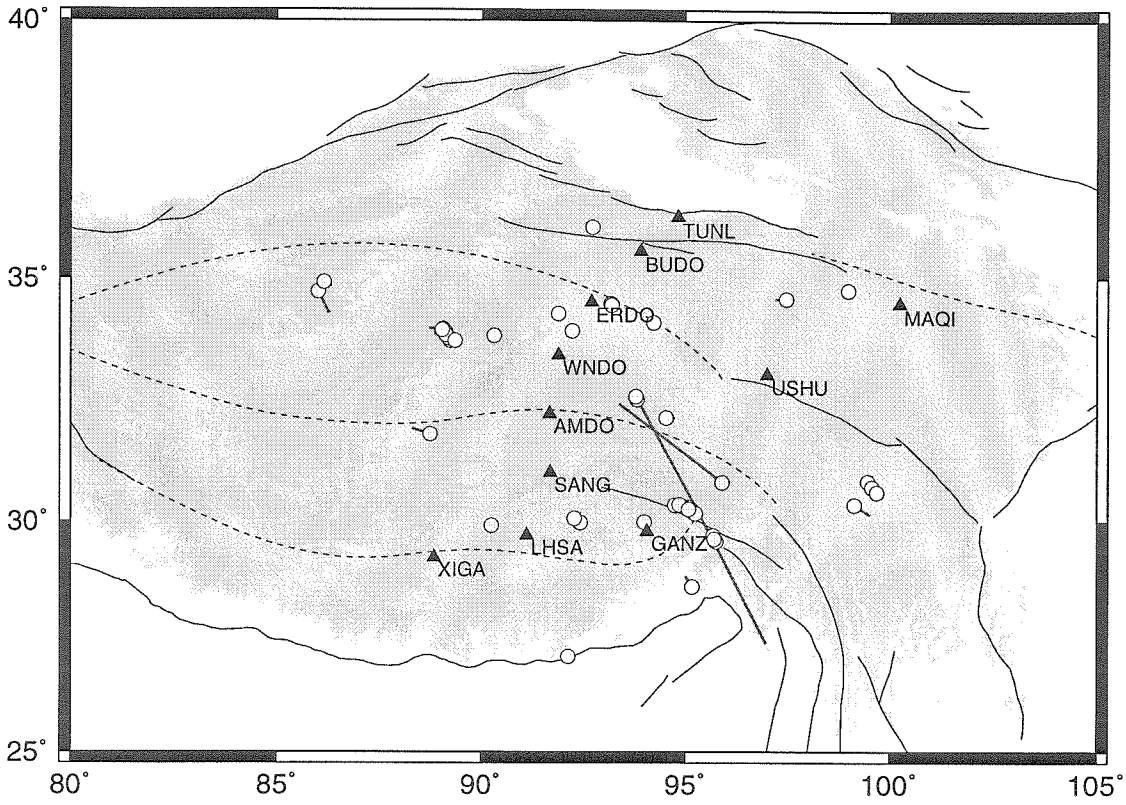

Figure 3.6: Event locations (circles) after the relocation; straight lines show the offset between the ISC location and the new location.

cation is that a cluster of events near station GANZ follow more closely the nearby fault after the relocation. Most offsets range between 10 and 50 km with no obvious preferred direction. There are two events that are relocated by several hundred kilometers from their ISC locations (300 km for event 270c and 650 km for event 090, see Table 3.2). These two are listed in the ISC Bulletin as "poor" or "unreliable" solutions. Their ISC locations are mostly based on P arrivals at a few stations in India and Pakistan, and the azimuthal coverage is very poor. On the other hand, their relocations are well constrained because they are located within the PASSCAL array. The relocation demonstrates the poor earthquake locations in the global catalog for a remote region such as Tibet.

Table 3.2: Comparison of the ISC locations with the relocation results

	ISC Location and Origin Time				Relocation		
Event	Date	o, GMT	Lat./Long.	M_b	Lat./Long.	Δx	Δo
199a	07/18/1991	13:24:56.9	30.37/94.83	4.4	30.26/ 95.10	28.7	-2.4
199b	07/18/1991	17:45:43.9	30.40/94.72	4.4	30.33/ 94.76	8.7	-2.1
201a	07/20/1991	18:52:24.1	30.30/94.77	4.3	30.19/ 95.19	42.2	-7.1
201b	07/20/1991	19:02:28.3	30.39/94.81	4.7	30.21/ 95.16	39.1	-2.8
204	07/23/1991	16:51:51.8	30.33/94.83	4.0	30.33/ 94.87	3.9	-0.6
205	07/24/1991	06:06:43.8	30.38/94.78	4.7	30.29/ 95.07	29.6	-4.3
206	07/25/1991	01:52:43.7	30.39/94.76	4.7	30.34/ 94.74	5.9	0.1
209	07/28/1991	23:58:20.5	30.34/94.80	4.8	30.16/ 95.24	46.8	-7.9
210a	07/29/1991	03:20:16.1	30.34/94.74	4.4	30.31/ 94.94	19.4	-4.8
210b	07/29/1991	15:48: 7.5	30.34/94.82	4.3	30.35/ 94.85	3.1	-1.7
211	07/30/1991	22:22: 5.3	30.37/94.81	4.6	30.25/ 95.08	29.1	-4.8
222	08/10/1991	20:21:52.7	33.87/92.19	4.8	33.94/ 92.24	9.0	0.0
239	08/27/1991	05:14:34.4	34.18/92.03	3.3	34.29/ 91.90	17.1	-2.8
242	08/30/1991	14:32:12.1	34.57/97.19	4.3	34.57/ 97.47	25.7	-0.2

continued on next page

continued from previous page

252	09/09/1991	21:54:51.7	28.84/95.00	4.6	28.61/ 95.16	29.9	-6.5
255	09/12/1991	23:06:30.7	29.69/95.70	4.5	29.69/ 95.67	3.9	-3.5
270a	09/27/1991	07:39:54.3	34.65/98.88	4.5	34.75/ 98.99	15.0	-0.3
270b	09/27/1991	11:56:40.7	30.00/90.41	3.7	29.91/ 90.26	17.6	-2.0
270c	09/27/1991	23:31:21.5	32.45/93.38	4.3	30.81/ 95.90	300.1	-18.9
323	11/19/1991	01:04:18.0	32.48/93.65	4.2	32.54/ 93.82	16.9	-1.7
325	11/21/1991	13:37:43.8	33.74/90.24	4.0	33.85/ 90.32	14.2	-2.7
328	11/24/1991	07:35:26.2	34.01/88.72	4.1	33.99/ 89.07	32.3	-2.5
329	11/25/1991	10:08:39.4	34.01/88.81	4.2	33.75/ 89.24	49.1	1.2
330a	11/26/1991	15:31:14.8	33.88/88.86	4.0	33.80/ 89.20	32.7	-0.3
330b	11/26/1991	21:16: 0.0	34.09/94.26	4.2	34.10/ 94.22	3.9	-1.9
336	12/02/1991	19:45:38.1	32.16/94.75	4.2	32.16/ 94.53	20.8	-3.3
348	12/14/1991	08:20:23.7	33.92/88.84	4.6	33.92/ 89.11	25.0	-1.5
349	12/15/1991	15:59:34.3	30.03/93.88	4.3	29.98/ 94.00	12.8	-4.3
351	12/17/1991	20:27:47.8	33.96/88.98	4.3	33.90/ 89.10	12.9	0.4
357a	12/23/1991	01:58:25.0	33.90/88.89	4.6	33.91/ 89.13	22.2	-1.0
357b	12/23/1991	02:14:56.0	33.90/88.97	4.8	33.87/ 89.13	15.1	-1.6
358	12/24/1991	21:27:50.9	30.11/92.52	4.4	29.97/ 92.44	17.3	0.4
360	12/26/1991	13:24:18.8	30.96/99.60	4.1	30.83/ 99.47	19.0	-0.2
365	12/31/1991	21:14:15.8	30.81/99.57	4.4	30.71/ 99.58	11.1	1.0
002	01/02/1992	02:35:38.4	33.94/88.85	4.1	33.97/ 89.04	17.9	-3.3
007	01/07/1992	16:23: 9.3	30.13/99.53	4.6	30.34/ 99.14	44.1	2.9
008	01/08/1992	17:41:39.9	30.19/92.46	3.9	30.06/ 92.30	21.1	2.3
023	01/23/1992	10:26:25.8	34.55/93.16	4.3	34.49/ 93.18	6.9	-0.9
034	02/03/1992	15:44:22.6	34.45/93.26	4.5	34.46/ 93.20	5.7	1.0
037	02/06/1992	03:35:15.0	29.61/95.64	4.9	29.57/ 95.75	11.6	-1.8
040	02/09/1992	12:44:52.8	29.64/95.68	4.3	29.62/ 95.70	2.9	-0.8

continued on next page

continued from previous page

076	03/16/1992	01:18:56.4	34.30/86.27	4.1	34.74/ 86.00	54.7	-8.0
090	03/30/1992	18:29:47.7	27.39/96.98	3.9	32.60/ 93.79	653.7	21.4
104	04/13/1992	03:47:50.7	31.95/88.31	4.4	31.83/ 88.75	43.7	0.6
109	04/18/1992	18:19:28.9	36.09/92.56	4.4	36.01/ 92.73	17.7	1.5
111	04/20/1992	18:50:27.3	26.99/92.11	4.5	27.11/ 92.15	13.9	-2.6
139	05/18/1992	19:55:39.0	34.85/86.33	4.0	34.93/ 86.14	19.4	-7.7
143	05/22/1992	05:47:31.4	30.72/99.63	4.5	30.60/ 99.69	14.4	-2.2
155	06/03/1992	02:42:36.9	33.90/88.91	4.5	33.75/ 89.36	44.8	5.9

Δx: relocation offset in kms.

Δo: origin time in seconds with respect to the ISC origin time.

The total *rms* of P and S travel time residuals drop by 91% and 84% respectively after the relocation, although only P arrival times are used to relocate events. The velocities of Pn, Pg, Sn, and Sg are estimated from the relocated travel times (Figure 3.5). Our 8.17 km/s of Pn velocity is consistent with previous results [*Chen and Molnar*, 1981; *McNamara et al.*, 1995]. The Pg and Sg velocities represent the velocities of the upper crust. If we extrapolate the velocities to the lower crust, the estimated crustal thickness from the Pn and Sn intercept times is 63 to 68 km, assuming a shallow source depth of 10 km. If we fix the crustal thickness at 65 km, then the average crustal velocities from the intercept times are 6.25 km/s for P and 3.42 km/s for S. The results indicate the low crustal velocities of the plateau and a possible decreasing of S velocity in the lower crust.

3.5 SH Waveform Modeling

The above section has established the crustal velocities and thickness. The velocity structure in the top 10 km of the upper crust still needs to be determined because that part has a strong influence on the propagation of regional Love and Rayleigh waves. Two previous velocity models, M45 and TIP, have a top layer 3.8 to 4 km thick with

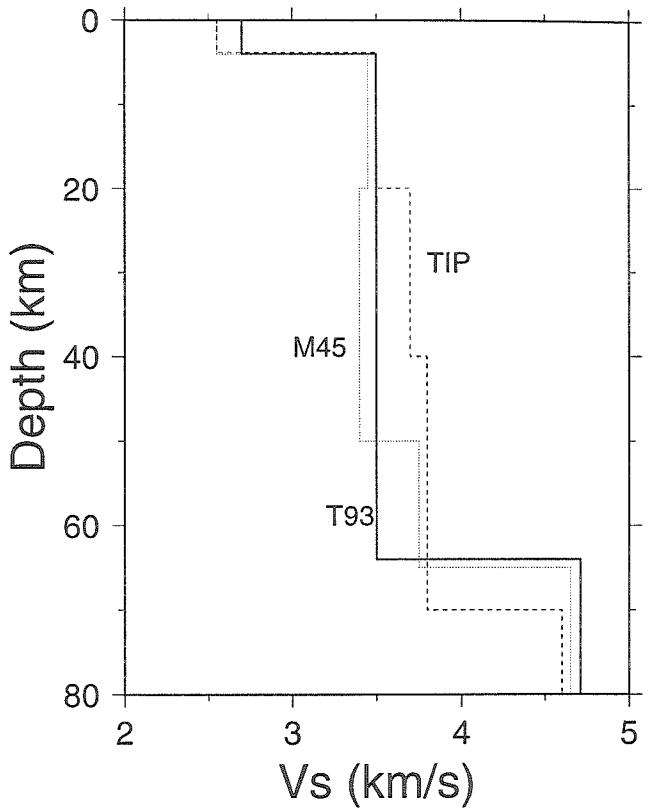

Figure 3.7: Two previous Tibetan crustal velocity models: TIP (dashed line), M45 (dotted line), and our new model T93.

an S velocity of 2.55 km/s (Figure 3.7). Model M45 was derived from pure-path phase velocity dispersions of long-period surface waves [*Romanowicz*, 1982]. TIP was from waveform modeling of long-period SH displacements of Tibetan earthquakes recorded in India [*Zhao et al.*, 1991]. Since we now have high quality waveform data at closer distances with both source and receiver within the plateau, a better constraint can be made on the structure of the uppermost layer.

We use the Love wave waveforms of Event 222 to invert for the velocity structure of the uppermost layer which is parameterized by a layer thickness and an S velocity. The source depth and mechanism for the event are taken from *Randall et al.* [1995] who estimate the moment tensors of 38 events using their long-period displacement records. Synthetic seismograms are computed for a range of velocity models with different thicknesses and velocities. The *rms* of misfit between the observed waveforms and synthetics is shown in Figure 3.8. The elongated minimum area shows the trade-

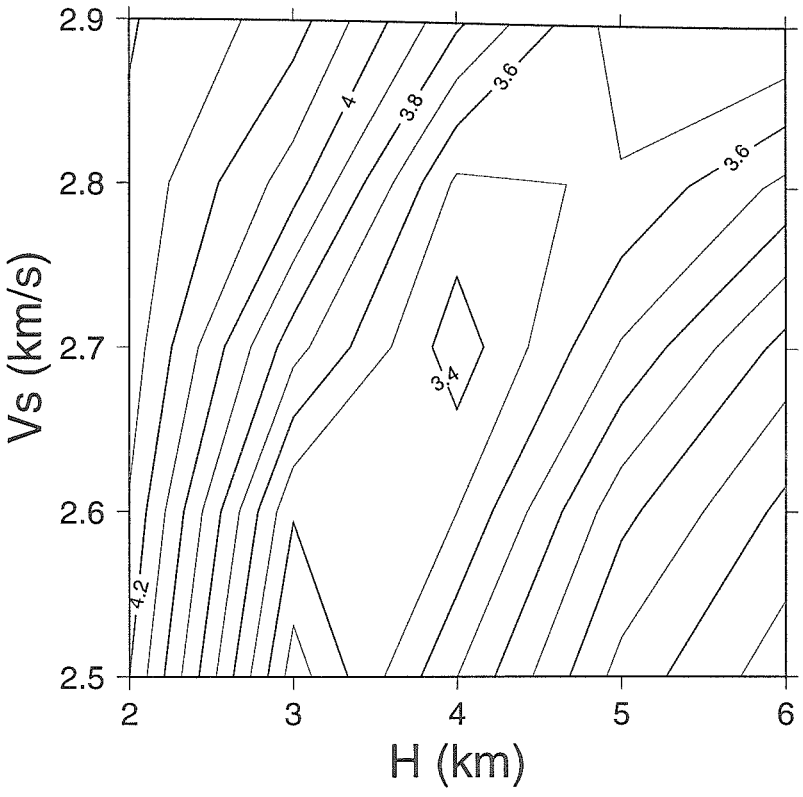

Figure 3.8: Waveform misfit errors between the SH waveforms of event 222 and synthetics using different velocity models for the uppermost layer.

off between the thickness and velocity, which is quite common for surface wave studies. The best model which fits the waveforms of Event 222 and has a similar thickness to that of M45 and TIP is a 4 km thick layer with an S velocity of 2.7 km/s.

Our final 1-D crustal model consists of two layers (Table 3.3 and Figure 3.7): the low velocity layer on top of a 60 km thick main crustal layer with an S velocity of 3.50 km/s and a P velocity of 6.25 km/s. Uppermost mantle P and S velocities are 8.08 km/s and 4.72 km/s respectively, from the obtained Pn and Sn velocities with earth curvature correction. This simplified crustal model does not imply in any way a homogeneous crustal structure of Tibet. In fact, as we will see in the following chapters, there are many indications of complicated structure with lateral variation. However, the 1-D model, derived purely from the observations within the plateau, serves as a good starting model for investigating structural details.

Table 3.3: 1-D velocity model of the Tibetan Plateau

Layer	Thickness, km	Vp, km/s	Vs, km/s
1	4	4.70	2.70
2	60	6.25	3.50
3	–	8.08	4.72

3.6 Source Depths and Mechanisms of Tibetan Earthquakes

Displacements of 62 events are recovered from their velocity records by removing instrument responses. In addition to the 49 events used in the travel time analysis, we also study three sub-crustal events in southern Tibet and 10 events in Qilian Shan, northeast of the Qaidam Basin (Figure 3.9). We use the CAP method to estimate source mechanisms and depths, as described in Chapter 2. Green's functions of the 1-D model are computed using a frequency-wavenumber (F-K) integration method [*Wang and Herrmann*, 1980; *Saikia and Burdick*, 1991]. All inversions are done in a period range between 100 s and 5 s. The results are listed in Table 3.4 and are plotted in Figure 3.9. The waveform fits by these solutions are visually checked. Most of them are very good, as shown by two samples in Figure 3.10 and Figure 3.11. It can be seen that the synthetics from the simple 1-D model match observations quite well. Our results are compared with those by *Randall et al.* [1995]. The two generally agree with each other well, but we include more events of smaller magnitudes.

Table 3.4: Source mechanisms and depths from the waveform inversion

Event	Date	o, GMT	Lat.	Long.	$\phi/\delta/\lambda$	h	M_w	h_I	M_b
199a	07/18/1991	13:24:54.5	30.26	95.10	200/20/-30	5	4.1	9	4.4
199b	07/18/1991	17:45:41.8	30.33	94.76	170/20/-50	5	3.6	33	4.4
201a	07/20/1991	18:52:17.0	30.19	95.19	150/10/-70	5	3.5	33	4.3
201b	07/20/1991	19:02:25.5	30.21	95.16	140/10/-80	5	4.0	6	4.7

continued on next page

continued from previous page

204	07/23/1991	16:51:51.2	30.33	94.87	10/70/-80	5	4.0	14	4.0
205	07/24/1991	06:06:39.5	30.29	95.07	0/60/-90	5	3.7	22	4.7
206	07/25/1991	01:52:43.8	30.34	94.74	200/30/-60	5	3.7	16	4.7
209	07/28/1991	23:58:12.6	30.16	95.24	200/20/-30	5	4.0	34	4.8
210a	07/29/1991	03:20:11.3	30.31	94.94	290/80/-80	5	3.5	33	4.4
210b	07/29/1991	15:48: 5.8	30.35	94.85	210/30/-30	10	3.9	20	4.3
211	07/30/1991	22:22: 0.5	30.25	95.08	180/20/-60	5	3.9	26	4.6
222	08/10/1991	20:21:52.7	33.94	92.24	250/80/ 10	10	4.7	15	4.8
239	08/27/1991	05:14:31.6	34.29	91.90	260/60/ 0	10	4.0	33	3.3
242	08/30/1991	14:32:11.9	34.57	97.47	100/70/-20	10	4.0	18	4.3
245	09/02/1991	11:05:50.5	37.41	95.38	90/40/ 80	20	4.6	10	4.8
251	09/08/1991	23:54:42.3	36.59	98.59	260/50/ 80	10	4.2	28	4.6
252	09/09/1991	21:54:45.2	28.61	95.16	250/30/ 20	30	4.3	0	4.6
255	09/12/1991	23:06:27.2	29.69	95.67	10/50/ 90	5	3.9	38	4.5
263	09/20/1991	11:16:11.7	36.18	100.06	110/50/ 80	15	4.8	13	5.1
270a	09/27/1991	07:39:54.0	34.75	98.99	330/30/ 80	5	4.0	22	4.5
270b	09/27/1991	11:56:38.7	29.91	90.26	250/50/ 10	10	3.4	33	3.7
270c	09/27/1991	23:31: 2.6	30.81	95.90	280/50/-20	10	3.7	33	4.3
273	09/30/1991	16:33: 5.2	37.79	101.40	100/40/ 90	15	4.8	13	4.8
279a	10/06/1991	09:48:51.0	37.38	101.19	60/70/ 60	10	3.7	10	4.2
279b	10/06/1991	12:18:12.0	37.89	101.33	100/60/ 50	10	3.9	10	4.5
285	10/12/1991	12:23:48.3	37.83	101.16	290/80/-20	15	3.9	46	4.3
323	11/19/1991	01:04:16.3	32.54	93.82	20/40/-90	10	3.9	33	4.2
325	11/21/1991	13:37:41.1	33.85	90.32	250/70/-10	10	4.5	49	4.0
328	11/24/1991	07:35:23.7	33.99	89.07	230/50/-60	15	3.9	29	4.1
329	11/25/1991	10:08:40.6	33.75	89.24	220/40/-50	10	4.2	32	4.2
330a	11/26/1991	15:31:14.5	33.80	89.20	200/40/-80	10	4.1	33	4.0

continued on next page

continued from previous page

330b	11/26/1991	21:15:58.1	34.10	94.22	290/60/-30	10	4.3	32	4.2
336	12/02/1991	19:45:34.8	32.16	94.53	40/70/-80	10	4.0	57	4.2
348	12/14/1991	08:20:22.2	33.92	89.11	30/40/-80	15	4.7	31	4.6
349	12/15/1991	15:59:30.0	29.98	94.00	210/70/-20	10	3.9	33	4.3
351	12/17/1991	20:27:48.2	33.90	89.10	230/40/-50	10	4.1	15	4.3
355	12/21/1991	19:52:45.1	27.80	87.95	200/80/-30	70	4.7	65	4.7
357a	12/23/1991	01:58:24.0	33.91	89.13	20/40/-90	15	4.7	32	4.6
357b	12/23/1991	02:14:54.4	33.87	89.13	10/40/-70	10	4.4	48	4.8
358	12/24/1991	21:27:51.3	29.97	92.44	30/40/-70	10	4.1	20	4.4
360	12/26/1991	13:24:18.6	30.83	99.47	300/70/-10	15	4.1	33	4.1
365	12/31/1991	21:14:16.8	30.71	99.58	120/60/ 0	15	4.2	5	4.4
002	01/02/1992	02:35:35.1	33.97	89.04	210/40/-80	10	4.3	48	4.1
007	01/07/1992	16:23:12.2	30.34	99.14	300/60/-60	10	4.0	29	4.6
008	01/08/1992	17:41:42.2	30.06	92.30	30/50/-70	10	3.8	14	3.9
012	01/12/1992	00:12:27.3	39.67	98.34	80/80/ 20	20	4.8	22	5.1
023	01/23/1992	10:26:24.9	34.49	93.18	280/50/ 40	5	4.1	19	4.3
034	02/03/1992	15:44:23.6	34.46	93.20	280/80/ 70	10	4.3	10	4.5
037	02/06/1992	03:35:13.2	29.57	95.75	10/50/ 70	5	4.8	15	4.9
040	02/09/1992	12:44:52.0	29.62	95.70	0/50/ 70	10	4.3	10	4.3
067	03/07/1992	22:41:49.8	29.68	89.31	250/60/-20	80	4.2	92	4.3
076	03/16/1992	01:18:48.4	34.74	86.00	240/60/-40	15	4.2	36	4.1
090	03/30/1992	18:30: 9.1	32.60	93.79	40/50/-60	10	3.7	33	3.9
095	04/04/1992	17:43:19.7	28.12	87.96	50/70/-30	80	4.8	25	4.2
104	04/13/1992	03:47:51.3	31.83	88.75	50/60/ 0	20	4.4	35	4.4
109	04/18/1992	18:19:30.4	36.01	92.73	90/70/-10	5	4.2	8	4.4
111	04/20/1992	18:50:24.7	27.11	92.15	10/80/ 40	15	4.0	33	4.5
137	05/16/1992	20:19:53.1	36.19	100.09	280/30/ 80	15	4.3	17	4.5

continued on next page

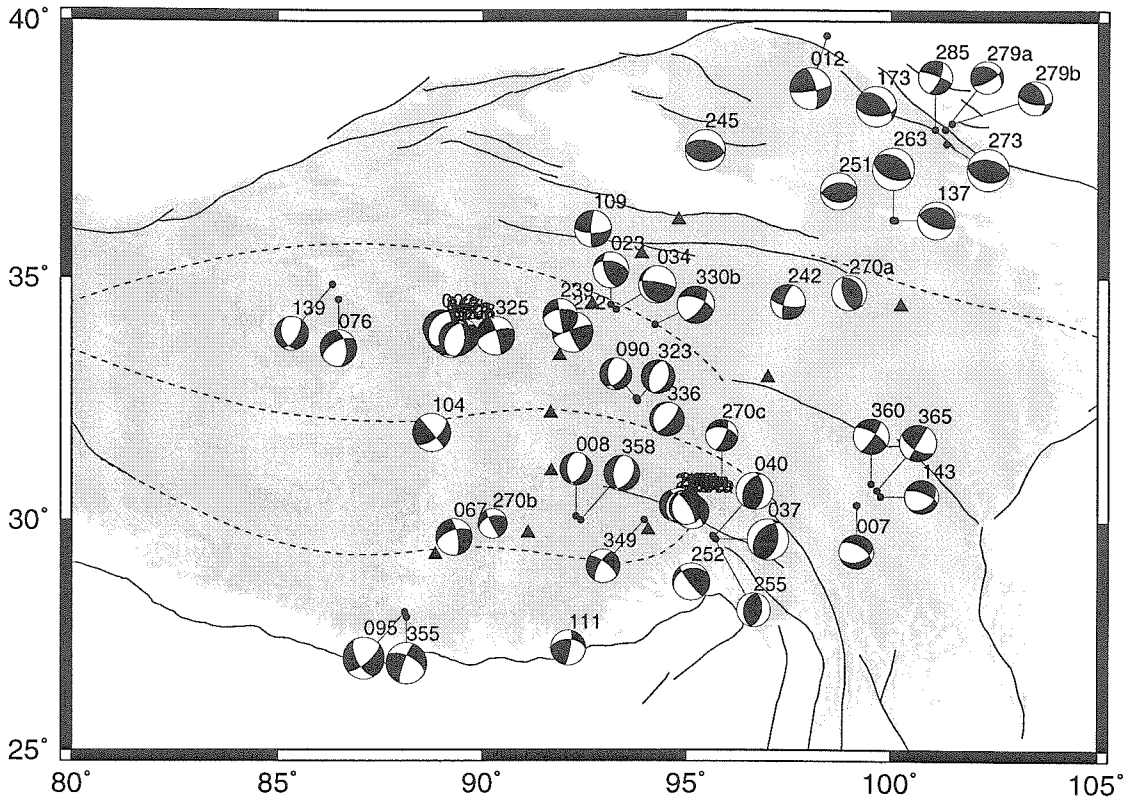

Figure 3.9: Source mechanisms of earthquakes in Tibet and surrounding areas determined from inverting their broadband regional waveforms. All earthquakes are found to be located in the upper crust, between 5 and 30 km, except three events (Events 355, 095, and 067) in southern Tibet that lie at depths between 70 and 80 km.

continued from previous page

139	05/18/1992	19:55:31.3	34.93	86.14	30/60/-60	5	3.9	33	4.0
143	05/22/1992	05:47:29.2	30.60	99.69	290/70/-60	10	3.9	30	4.5
155	06/03/1992	02:42:42.8	33.75	89.36	210/40/-70	10	4.1	10	4.5
173	06/21/1992	11:19:37.2	38.33	99.45	90/50/ 60	15	4.6	2	4.9

ϕ, δ: strike and dip of the fault plane in degrees.

λ: rake of the slip in degrees.

h: source depth in kms; h_I is the ISC depth.

The three sub-crustal events will be discussed in the next chapter. The focal depths of most crustal events are determined to be between 5 and 15 km, except for one event at the southern margin (Event 252) that is 30 km deep. There are

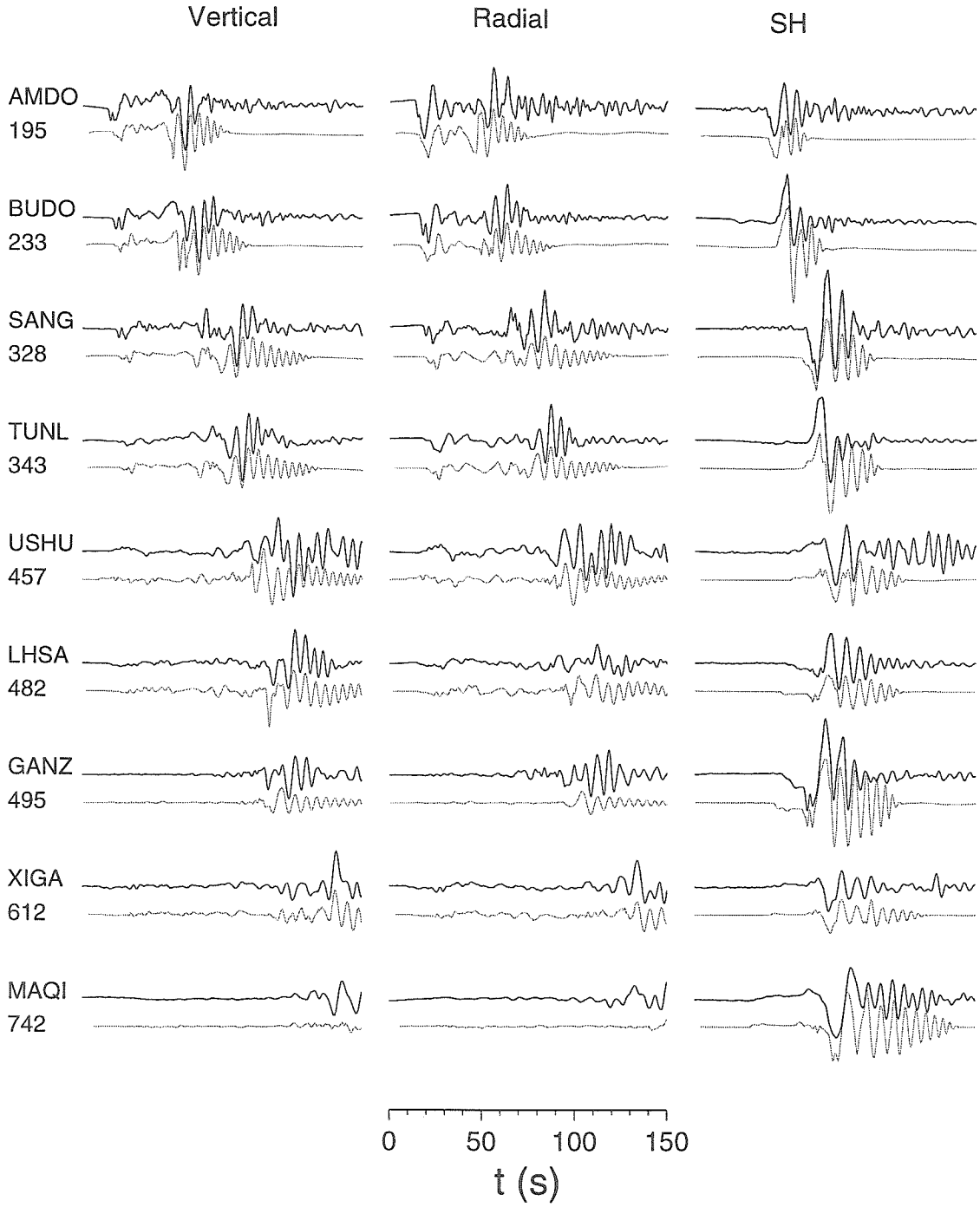

Figure 3.10: Displacement waveform fit of a crustal event (Event 222) produced by the waveform inversion. Each trace is multiplied by the square root of its epicentral distance (indicated by the number below the station name) to account for the surface wave amplitude decay with distance.

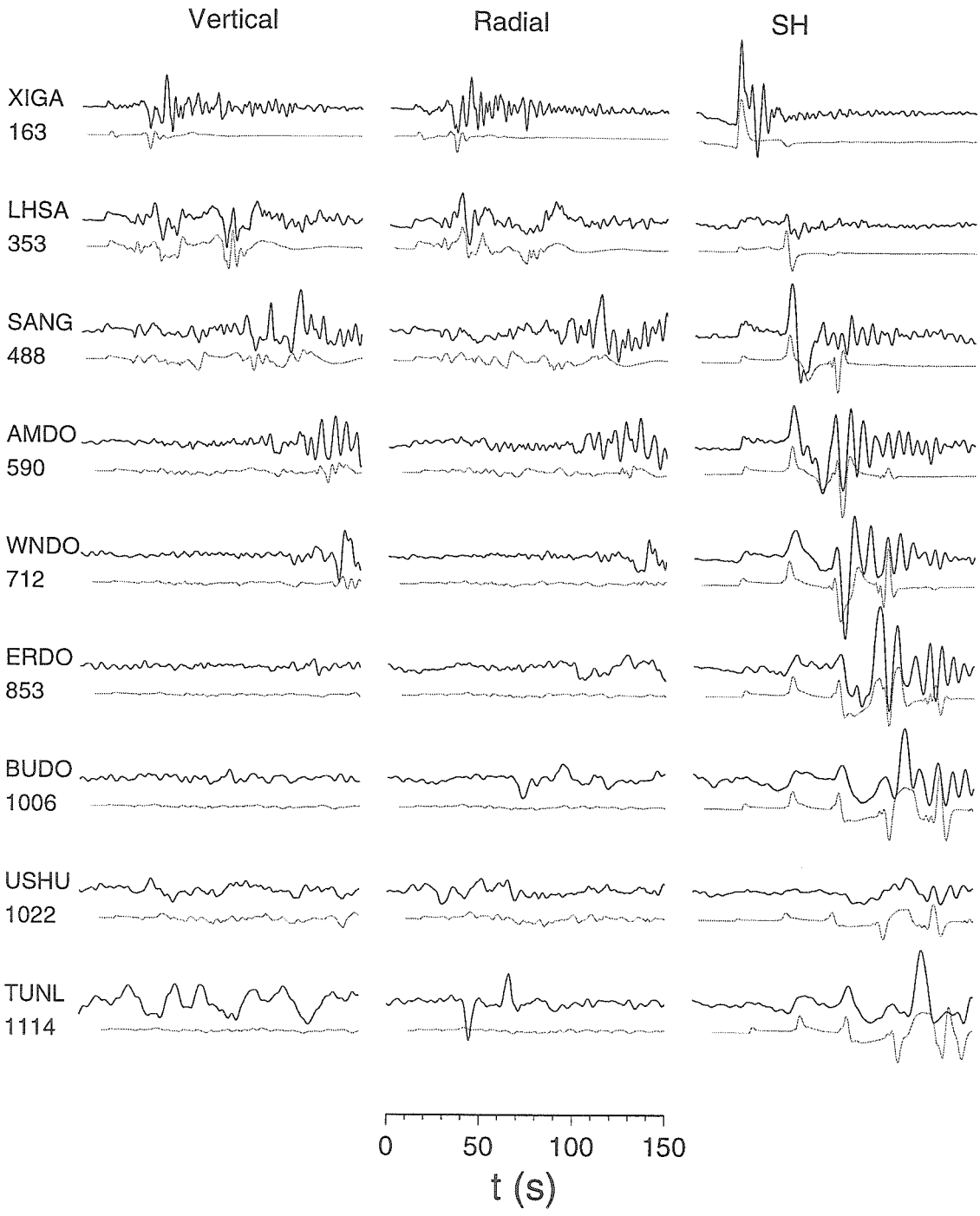

Figure 3.11: Displacement waveform fit for a sub-crustal event (Event 355) produced by the waveform inversion. Each trace is multiplied by its epicentral distance (indicated by the number below station name) to account for the body wave amplitude decay with distance.

diverse styles of source mechanisms which correlate strongly with elevations where the epicenters are located. Along the margins of the plateau and in Qilian Shan where surfacer elevations are below 4 km, thrusting events are dominant with few strike-slip events, probably reflecting ongoing crustal shortening in these regions. Within the plateau but at locations with surface elevation below 5 km, source mechanisms are a mixture of strike-slip and thrust. For areas with surface elevation higher than 5 km, all events show consistently normal faulting (Figure 3.9 and Figure 3.12). Such a variation of source mechanism with elevation in Tibet was noted by *Molnar and Lyon-Caen* [1989] when they compiled fault plane solutions of 74 large earthquakes between 1962 and 1986. Our results, although only from one year of events, demonstrate more clearly the separation of normal faulting from strike-slip/thrust faulting by the 5 km elevation.

3.7 Discussion and Conclusions

The regional earthquake travel time analysis and waveform modeling show that the Tibetan Plateau has low average crustal velocities, especially S velocity. The shallow source depths from waveform inversion indicate a shallow seismicity cut-off depth. These suggest a high crustal geothermal gradient which could be produced by the concentration of continental crustal materials during crustal shortening [*Zhao and Helmberger*, 1991]. An alternative might be high heat flow from the upper mantle. Although the Pn and Sn velocities are high, they might only represent velocities in the uppermost mantle. We will see later from the teleseismic arrival delays that a lower velocity upper mantle exists beneath north-central Tibet.

5 km seems to be a critical elevation at which the Tibetan Plateau can be maintained over long distances. Normal fault earthquakes occur where elevations are above this limit, an indication of crustal thinning and extension. The numerous large scale NS-trending grabens in southern and central Tibet are probably products of this extension over long geological time. The timing and mechanism of the transition from the early NS compression to the current EW extension is not clear. It is proposed

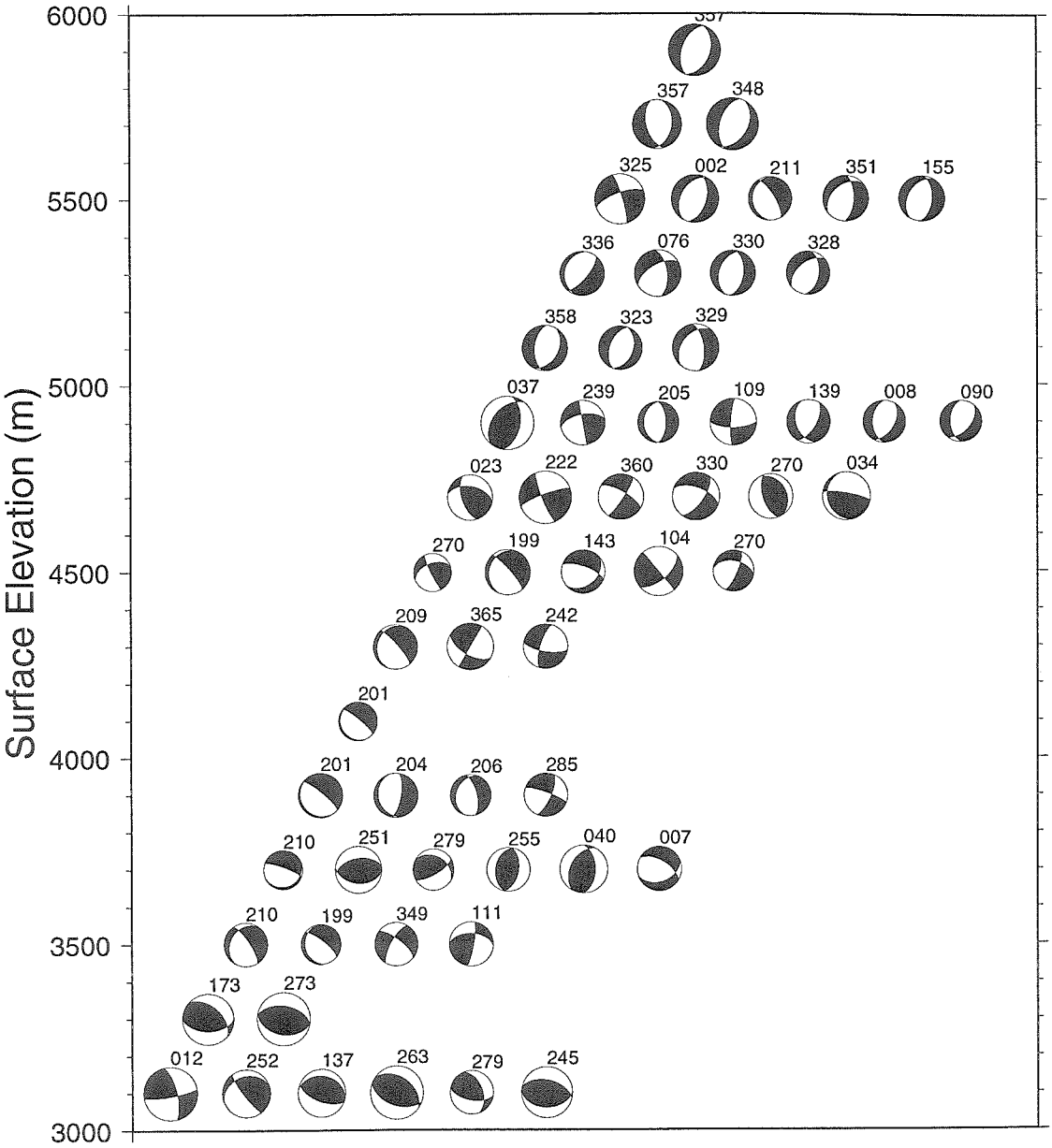

Figure 3.12: Variation of source mechanism with surface elevation.

that the transition occurred when the thickened Tibetan mantle lithosphere was removed by a thermal instability, which subsequently lifted the plateau from 3 km to 5 km [*England and Houseman*, 1986]. However, as we will see later, the low velocity "hot" upper mantle is beneath the northern plateau where the elevations have not reached 5 km and earthquake source mechanisms show NE horizontal compression. These are issues that need to be addressed by future studies.

Chapter 4

Intermediate Depth Earthquakes Beneath the India-Tibet Collision Zone

4.1 Abstract

We report on three intermediate depth earthquakes in the India-Tibet collision zone, two under the Himalayan Thrust Belt (HTB) and one beneath the Indo-Zangbu suture. The M_b magnitudes of these three events are from 4.3 to 4.9, and are too small to be well located by conventional means. However, from modeling their broadband waveforms recorded at near-regional distances on a temporary PASSCAL array, we can confidently confine the sources to be below the crust, between 70 and 80 km deep. The existence of these intermediate depth earthquakes in this area suggests relatively low temperatures in the mantle lithosphere. The two events under the HTB display strike-slip mechanisms with some normal faulting component; this is quite different from the shallow thrust events typical of the same area. The principal P and T axes of all three fault plane solutions show roughly NS compression and EW extension, consistent with a regional stress field produced by the indenting of the Indian continent.

4.2 Introduction

Since the inception of the India-Eurasia collision at approximately 45 Ma, the India plate has indented northwards about 2000 km, producing the highest continuous topography on earth, the Himalayas and the Tibetan Plateau. In the past two decades, considerable efforts were made to investigate the crustal and upper mantle structure

of this area in order to understand the collision mechanism and formation of the plateau (see *Molnar* [1988] for a review).

Among various approaches, studying source characteristics and depth distribution of earthquakes provides unique information about mechanical properties and stress orientation of lithosphere. There have been numerous results published based on the relocation and source inversion of large events in the Tibetan Plateau and surrounding areas [*Molnar and Chen*, 1983; *Baranowski et al.*, 1984; *Ni and Barazangi*, 1984; *Molnar and Lyon-Caen*, 1989; *Zhao and Helmberger*, 1991]. These studies conclude that seismicity beneath the Tibetan Plateau is shallow, restricted to the upper 20 km of the crust. Only three intermediate depth earthquakes (85-90 km deep) located in southern Tibet were reported (see Figure 4.1) [*Chen et al.*, 1981; *Molnar and Chen*, 1983; *Ekstrom*, 1987; *Chen*, 1988]. Due to the lack of seismic stations on the plateau, almost all of above studies used records from stations outside the plateau, usually at teleseismic distances, thus limiting the number of events that could be investigated. However, from 1991 to 1992, a PASSCAL experiment was conducted on the Tibetan Plateau with a deployment of 11 broadband stations. In this report, we present waveform modeling results of 3 events which show strong evidence of sub-crustal focal depths. One of the events is located in the same area as two previous intermediate depth events (Figure 4.1), and the other two lie under the Himalayan Thrust Belt (HTB), where, to our knowledge, few intermediate depth events have been reported to date.

4.3 Data and Results

The stations occupied during the 1991-1992 Tibet PASSCAL experiment were equipped with STS-2 Streckheisen seismometers which have a flat velocity response between 0.008 and 50 Hz. The details of the instrumentation can be found in *Owens et al.* [1993]. During its one-year deployment, about 50 earthquakes within the plateau were recorded by the array with good signal-to-noise ratios (Figure 4.1). *Randall et al.* [1995] determined the focal depths and moment-tensors of 38 events in the

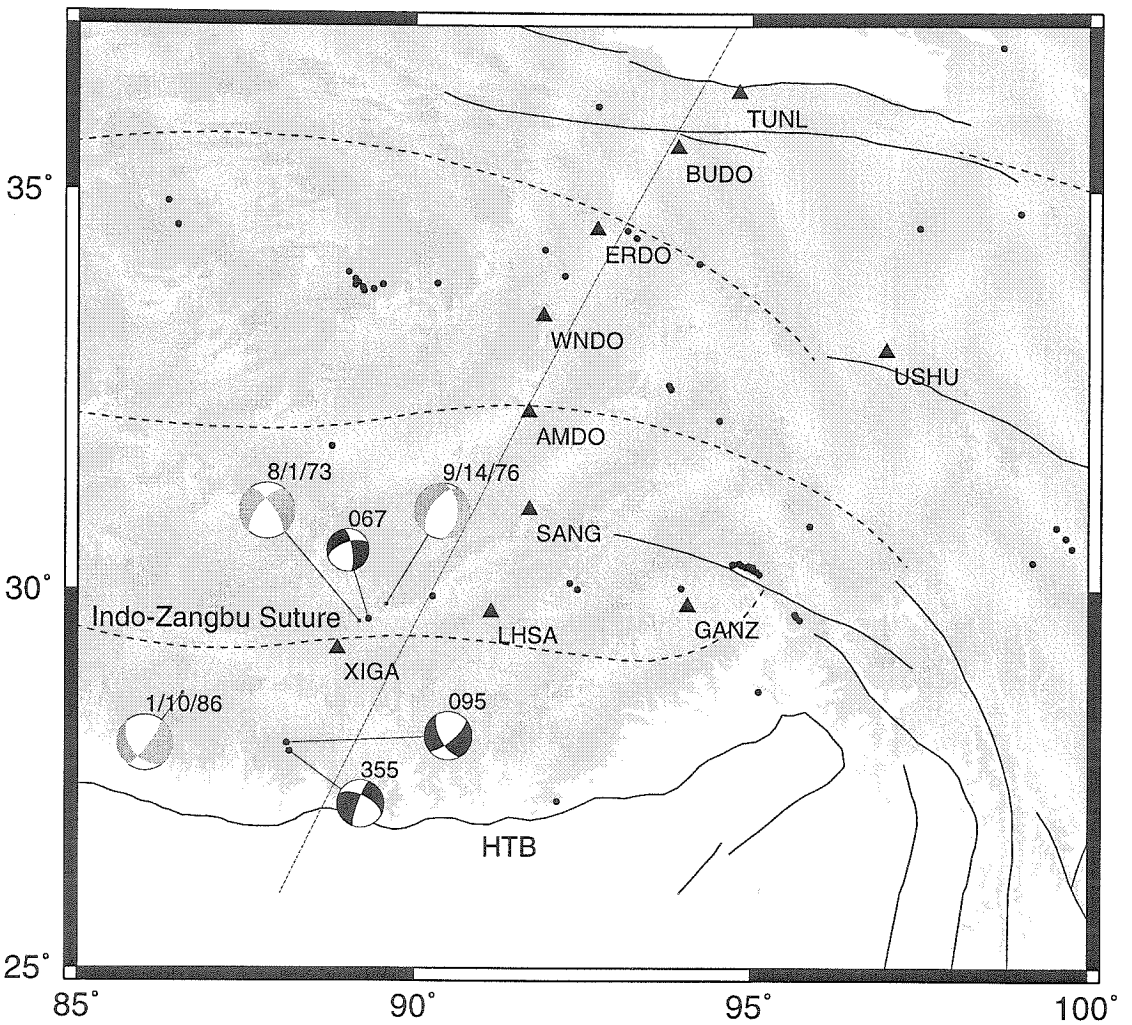

Figure 4.1: Map of eastern Tibet showing major tectonic boundaries and the station locations (triangles) of the 1991-1992 Tibet PASSCAL experiment. Shading indicates elevation above 3 km. Darkly shaded focal spheres are for sub-crustal events analyzed in this study. Lightly shaded focal spheres are from *Molnar and Chen* [1983] and the Harvard CMT solution (for event on 1/10/86). All of them are located at intermediate depths. A crustal cross section along with the source mechanisms of these events is shown in Figure 5.9. The straight line shows the location of the cross section.

Table 4.1: Locations of the events from the PDE catalog

Event	Date	Origin time	Lat./Long.	h, km	M_b
355	12-21-91	$19^h52^m45.5$	27.90N/88.14E	57	4.9
067	03-07-92	$22^h41^m50.8$	29.44N/89.37E	113	4.3
095	04-04-92	$17^h43^m20.7$	28.15N/87.98E	33	4.9

north-central and southeastern part of the plateau by inverting long-period waveforms ($T > 20$ s). Their results agree with previous studies that have indicated shallow seismicity.

The Preliminary Determination of Epicenter (PDE) catalog locations and origin times of the three events investigated in this chapter are listed in Table 4.1. Events 355 and 095 are reported as crustal events and event 067 as sub-crustal. A distinguishing character of all three events recorded on the array is their sharp direct P and S arrivals, even at large distances (Figure 4.2). This feature suggests a sub-crustal focal depth because the first arrivals beyond 320-350 km for crustal events in this region are head waves with emergent onsets on broadband displacement records.

To test the sensitivity of waveforms to the focal depth, we have calculated the Green's functions for different source depths from 10 km to 90 km, using a reflectivity code developed by *Saikia and Burdick* [1991]. The velocity model consists of two layers over a half space with the Moho at 64 km (Table 3.3). It is very similar to model M45 [*Romanowicz*, 1982] which has proven reasonably good for modeling events on the Tibetan Plateau [*Randall et al.*, 1995]. Figure 4.3 shows the SH component of the Green's functions at a distance of 350 km for various source depths, along with the observed SH displacements for Events 355 and 095 recorded at the same distances. We focus on the SH displacement first because it is much simpler than $P - SV$ displacement and has less dependence on source orientation. By comparing the waveforms for source depths of 60 km (above the Moho) and 70 km (below the Moho), one can see that the waveform shapes are quite diagnostic; the crustal synthetics predict a gently rising Sn phase whereas sub-crustal events produce a sharp onset. Furthermore, the strong crustal phase $Sd + SmS$ vanishes when the

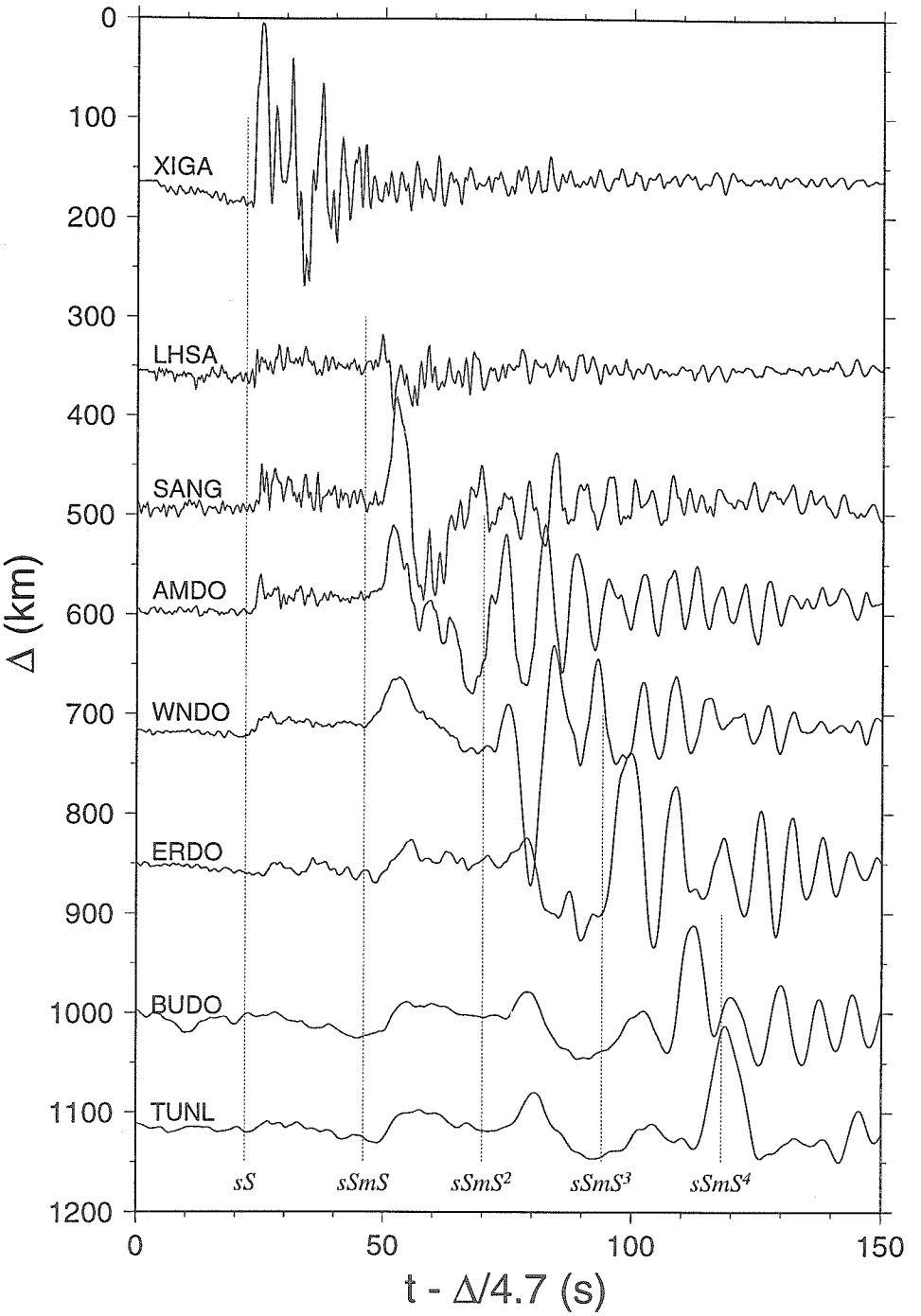

Figure 4.2: SH displacements of event 355. Note the sharp onsets of S waves beyond 300 km. Crustal multiples up to 4th order are indicated by the evenly separated dashed lines.

source is below the Moho. From the sharp S arrivals and lack of Sd/SmS in the observed waveforms, we conclude that Events 355 and 095 are sub-crustal events. The synthetics for sources at 70, 80, and 90 km also show that for a deeper source, the shape of the first arrival is more impulsive. Accordingly, the step-like shape of first S arrivals indicates that the two events are confined to the uppermost mantle.

Figure 4.4 compares vertical and radial displacements for Event 355 with synthetics generated from a source above the Moho (60 km) and below it (70 km). Source mechanisms obtained from inversion of the whole array data are used when constructing the synthetics. Although the long-period features of data and the two corresponding synthetics are similar, as is expected from theoretical arguments [*Helmberger and Malone*, 1975], the synthetics for sub-crustal focal depths match the broadband features of the data much better, with many individual phases aligned.

To invert whole broadband seismograms for source depths and mechanisms, we apply a grid search in the source parameter space (strike, dip, rake, M_0, depth) to find the global minimum of misfit between the synthetic and observed waveforms [*Zhao and Helmberger*, 1994]. An advantage of the method is that it allows time shifts between various portions of the observations and synthetics, thus relaxing the strong dependence of the inversion on the velocity model and the influence of lateral variation. Uncertainty of the solution can be estimated easily by quantifying the misfit error distribution around the global minimum.

The global minima of the three events as a function of depth are shown in Figure 4.5. As expected, the waveform misfit errors of all three events decrease rapidly as the sources drop below the Moho. The mechanisms show some depth dependence but remain mostly strike-slip. Table 4.2 lists the inversion results at the best-fit depths and the uncertainties estimated by examining all the solutions with misfit errors within 5% of the minimum. For all three events, the azimuths of the P and T axes are better constrained (within 10°), while the plunges are relatively poorly constrained (within 10° to 20°).

In Figure 4.1 we have plotted the lower-hemisphere projections of the best fault plane solutions. The source mechanisms of the two events under the HTB display

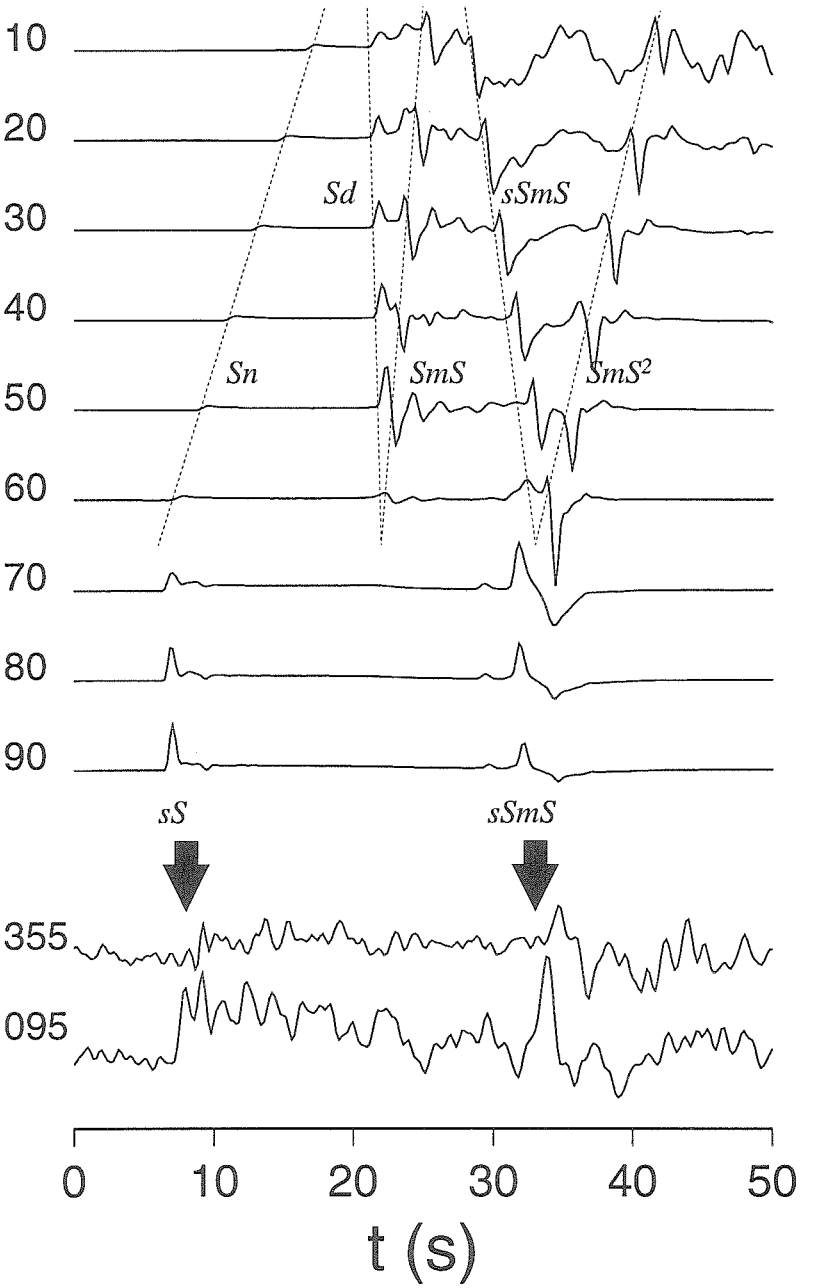

Figure 4.3: SH components of the Green's functions of a strike-slip source at different depths (numbers in km left of the trace). The velocity model is given in Table 3.3. Distance range is 350 km. Also shown in the figure are observed SH displacements of Events 355 and 095 recorded at station LHSA at the same distances.

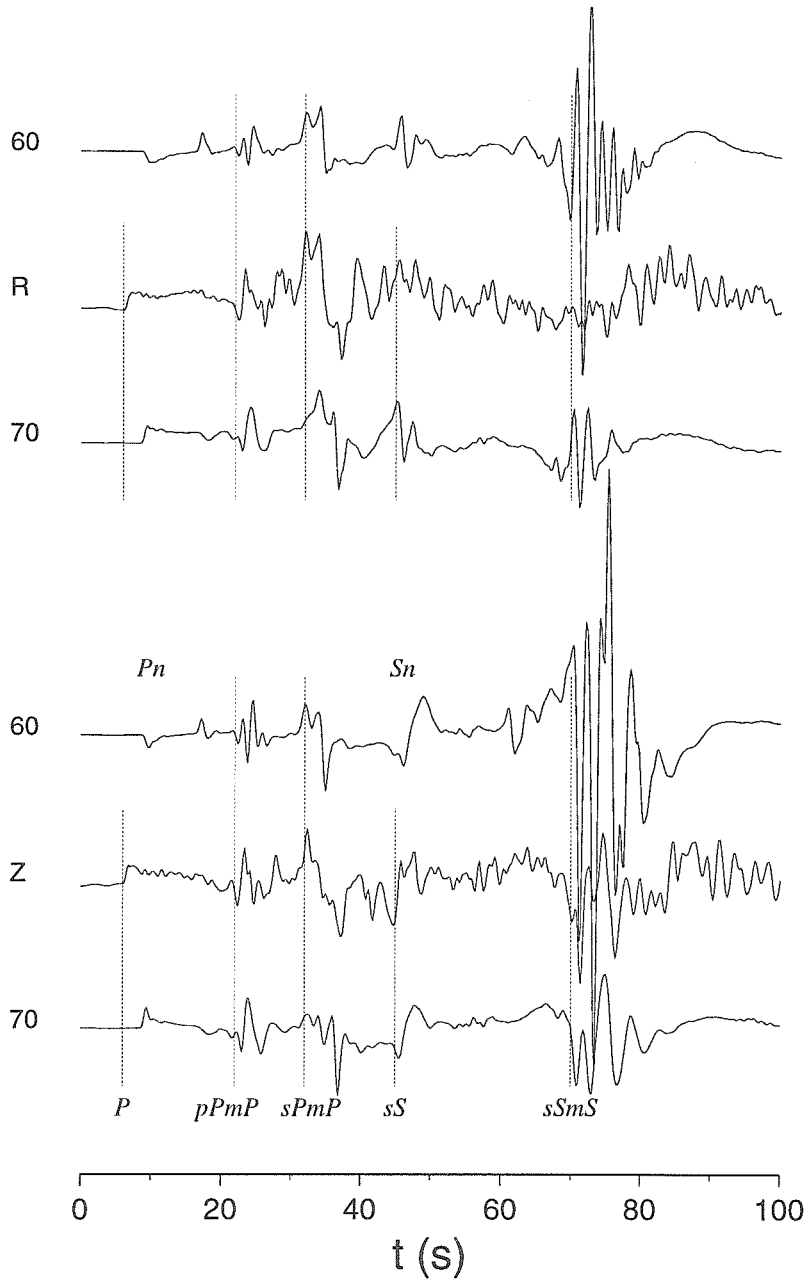

Figure 4.4: Comparison of the vertical and radial displacements from Event 355 at station LHSA with synthetics from a source above (60 km) and below (70 km) the Moho. The synthetics are constructed using the source mechanisms obtained from the waveform inversion at the corresponding depth.

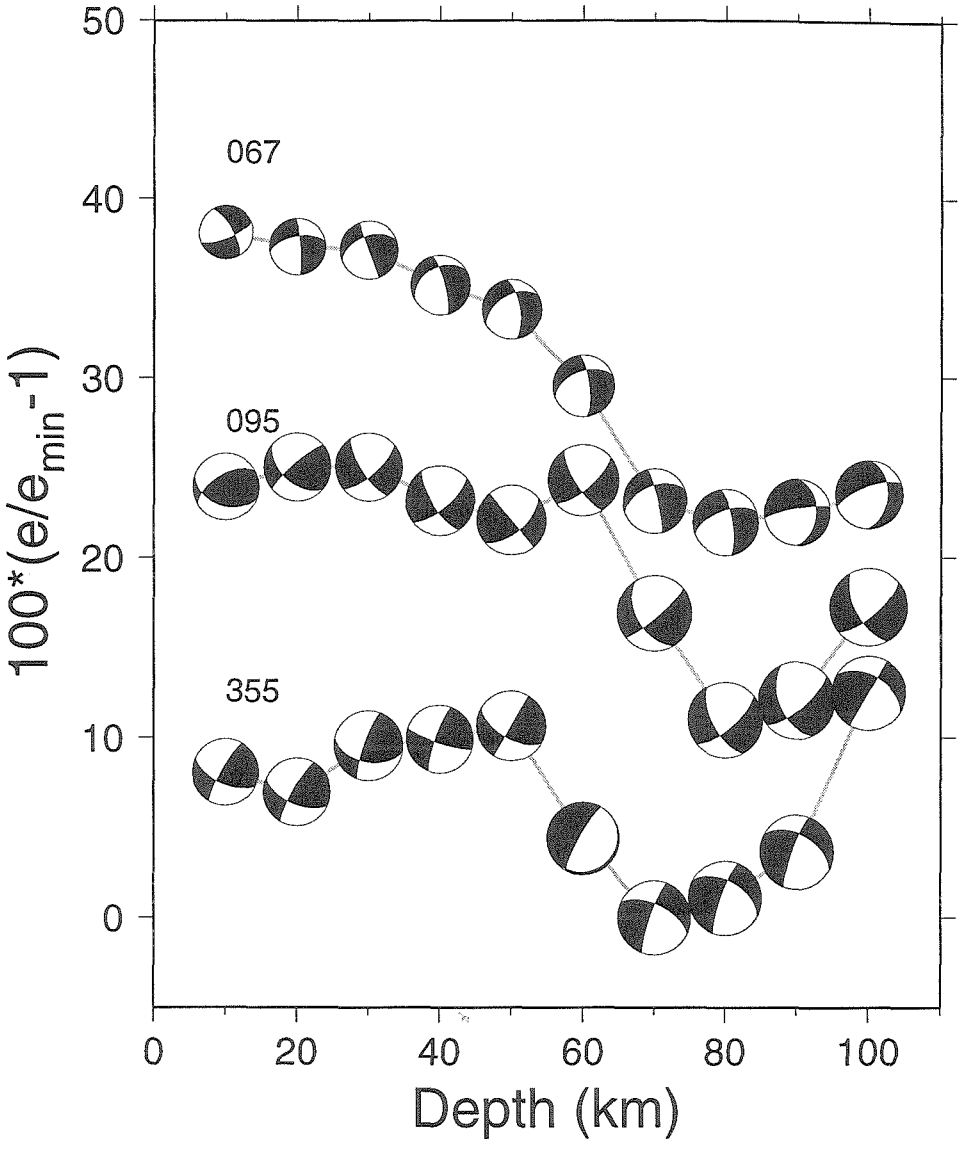

Figure 4.5: Waveform misfit as a function of focal depth. The misfit errors are normalized by the minimum. Curves for Events 095 and 067 are offset for display purpose.

Table 4.2: Focal depths and fault plane solutions from the waveform modeling

Event	P axis	T axis	h, km	M_0, 10^{16} Nm
355	154±6/28±20	251±7/13±15	70	1.41
067	213±6/34±11	118±8/ 8±11	80	0.25
095	8±6/35±11	102±9/ 5±14	80	2.00

P and T axes are given in form of azimuth/plunge in degrees.

strong strike-slip behavior with some normal faulting. They are quite different from the mechanisms of shallow events in the same area, which show consistent low-angle thrusting along the front of the Himalaya with slip vectors perpendicular to the mountain range [*Molnar and Chen*, 1983; *Baranowski et al.*, 1984; *Ni and Barazangi*, 1984; *Molnar and Lyon-Caen*, 1989]. The mechanism of the event near the suture zone is similar to the mechanism of the previous intermediate depth events nearby (Figure 4.1), except that it has more strike-slip component. The T axes are all horizontal in the EW direction and the P axes are roughly in the NS direction. This is consistent with a regional stress field produced by the indenting of the India continent.

4.4 Discussion

Focal depth determinations based on global network travel times have always been difficult because of the trade-off between the depth and origin time [*Zhao and Helmberger*, 1991]. This trade-off can be eliminated by the use of depth phases, pP and sP, but these phases become difficult to identify for magnitudes below 5, especially for strike-slip mechanisms. With broadband records at regional distances, the constraints on focal depths can be substantially improved. In particular, waveform modeling proves very effective in discriminating between crustal and sub-crustal events, due to their fundamental waveform differences. Moreover, our success in modeling the broadband waveforms at up to 1000 km distance range with a simple 1-D velocity model shows that to the first order the Tibetan Plateau has a relatively simple crustal

structure. We also emphasize that lateral variation does exist. For example, the tangential displacements at stations WNDO, ERDO, and BUDO are delayed about 5 s relative to the synthetics. These three stations are located in the north-central plateau where a mid-crustal low velocity zone is reported [*Brandon and Romanowicz*, 1986; *Zhu et al.*, 1995].

In summary, we have detected three intermediate depth earthquakes in the India-Tibet collision zone in a one-year time window. Taking into account three previous reports, it is reasonable to speculate that there are other unidentified intermediate depth earthquakes with moderate magnitudes in this area. The existence of intermediate depth earthquakes under the Himalaya and Indo-Zangbu suture indicates the temperatures of the mantle lithosphere in southern Tibet are relatively low. The small number of these events studied to date limits our ability to explore the details of structure and rheology of the lithospheric mantle, but we believe that with the installation and operation of the permanent CDSN station at Lhasa, more data will be available to shed light on questions about the tectonics in this continent-continent collision zone.

Chapter 5
Lateral Variation of the Lithospheric Structure of Tibet from Teleseismic Waveforms

5.1 Abstract

We present a teleseismic waveform study of the lithospheric structure beneath the Tibetan Plateau, using data collected during the 1991-1992 Sino-US Tibet seismic recording experiment. Crustal thickness at each of the 11 broadband stations is estimated from the differential travel time between the Moho P-to-S converted phase and direct P. We demonstrate that this estimation is not sensitive to the average crustal P or S velocity, but is strongly dependent on the Vp/Vs ratio. The ambiguity is removed by adding a secondary converted phase to the analysis so that both thickness and Vp/Vs ratio can be determined. We found crustal Vp/Vs ratios ranging from 1.75 to 2.0 and thicknesses from 55 to 80 km. On average the northern Tibetan crust is 20 km thinner and has a higher Vp/Vs ratio than the southern part. Teleseismic P and S arrival delays accurately measured by a multi-channel correlation technique exhibit large azimuthal and lateral variations. The delays after crustal correction indicate that the upper mantle velocities beneath the northern plateau are significantly slower too. The uniform surface elevation of Tibet coupled with the large variations of crustal thickness and upper mantle velocities suggests that the north-central plateau is supported partly by a hot upper mantle.

5.2 Introduction

The 1-D velocity model developed in Chapter 3 represents an average crustal structure of Tibet. Although good waveform fits are produced by this simple model using the CAP source estimation technique, large time-shifts are required for some event-station paths, which indicate lateral variation.

In this chapter, we will use teleseismic waveform data to investigate lateral variations of the crust and upper mantle beneath the Tibetan Plateau. Compared to regional waves, teleseismic waves have higher lateral resolution because of their steep incidence angle as they approach the station. A drawback is their poor vertical resolution. However, some features in the teleseismic waveforms can be used to alleviate this problem. Specifically, as teleseismic waves impinge on the crust, P-to-S or S-to-P conversions will occur at the crust-mantle boundary (Moho). These converted phases provide sampling paths within the crust and thus they can help to separate crustal anomalies from upper mantle anomalies. Here, we first use the teleseismic receiver function method to estimate the crustal thickness at each individual station. This estimation, derived from the time separation between the direct P and the Moho P-to-S conversion, is not sensitive to the average crustal P or S velocity, but is strongly dependent on the Vp/Vs ratio. For several stations where a secondary converted phase is identified, both crustal thickness and Vp/Vs ratio are determined. We also measure teleseismic P and S arrival delays using a multi-channel correlation technique to infer upper mantle velocity variations. Our results show that there are large lateral variations in both crustal structure and upper mantle velocities.

5.3 Crustal Thickness from Teleseismic P Waveforms

5.3.1 Teleseismic Receiver Function

When a teleseismic P wave impinges on the crust from underneath, part of the energy converts into a SV wave at the Moho. Because the incidence is nearly vertical, the converted SV wave has much stronger amplitude on the radial component. For this reason, the vertical component of teleseismic P records can be used as an effective source time function to isolate crustal response from the radial component [*Langston*, 1977]. The isolated response, called receiver function, is defined as:

$$r(t) = \int \frac{R(\omega)}{Z(\omega)} e^{i\omega t} d\omega, \tag{5.1}$$

where $Z(\omega)$ and $R(\omega)$ are spectra of vertical and radial components.

Computing receiver functions with the above definition involves spectrum division which is often numerically unstable because of limited signal bandwidth and noise. In practice, a water-level c is used to suppress "holes" in the spectrum $Z(\omega)$

$$r(t) = \int \frac{R(\omega)Z^*(\omega)}{|Z(\omega)|^2 + c} e^{i\omega t} d\omega. \tag{5.2}$$

Alternatively, the deconvolution can be done in the time-domain by solving the convolution equation:

$$Z(t) * r(t) = R(t),$$

which, when solved in the least-square sense, is reduced to

$$\begin{pmatrix} \sigma_0 & \sigma_1 & \dots & \sigma_m \\ \sigma_1 & \sigma_0 & & \\ \vdots & & \ddots & \\ \sigma_m & & & \sigma_0 \end{pmatrix} \begin{pmatrix} r_0 \\ r_1 \\ \vdots \\ r_m \end{pmatrix} = \begin{pmatrix} c_0 \\ c_1 \\ \vdots \\ c_m \end{pmatrix}, \tag{5.3}$$

where σ_i and c_i are auto- and cross-correlations of $Z(t)$ and $R(t)$. The matrix is in Toeplitz form so the linear equations can be solved very efficiently. Similar to the water-level c used in spectrum deconvolution, a penalty factor λ is used to stabilize the inversion. Correspondingly, (5.3) is modified as

$$\begin{pmatrix} \sigma_0 + \lambda & \sigma_1 & \dots & \sigma_m \\ \sigma_1 & \sigma_0 + \lambda & & \\ \vdots & & \ddots & \\ \sigma_m & & & \sigma_0 + \lambda \end{pmatrix} \begin{pmatrix} r_0 \\ r_1 \\ \vdots \\ r_m \end{pmatrix} = \begin{pmatrix} c_0 \\ c_1 \\ \vdots \\ c_m \end{pmatrix}. \tag{5.4}$$

In either frequency or time domain deconvolutions, a range of c or λ are tested and the best deconvolution result is selected. Both methods give similar results. We found that the time domain deconvolution often has slightly higher time resolution.

5.3.2 Estimates of Crustal Thickness Using Moho P-to-S Conversion

Because of the large velocity contrast at the crust-mantle boundary, the Moho P-to-S conversion is often the largest signal following the direct P in a receiver function. An example is shown in Figure 5.1 for a simplified one-layer crustal model. In this idealized case, both the primary converted phase Ps and the secondary $PpPms$ are clear and have comparable amplitudes. In reality, because the latter phase has a reflection at the surface and travels longer in the crust, it is more easily affected by lateral variation.

The time separation between Ps and P can be used to estimate crustal thickness,

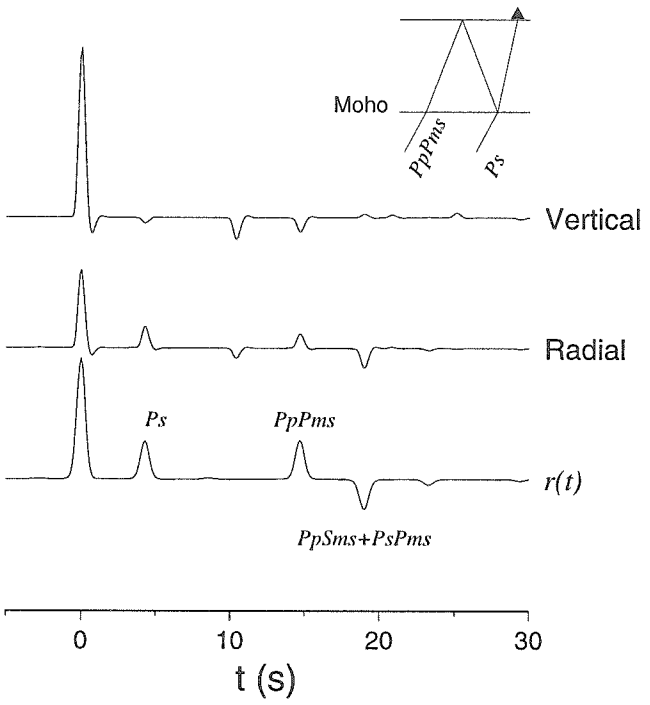

Figure 5.1: Vertical and radial responses for a one-layer crustal model and the corresponding receiver function $r(t)$. Several important phases are labeled and their ray paths are shown in the figure. Phase labeling follows standard convention, lower case letters denote upgoing travel paths, upper case letters denote downgoing travel paths, and m indicates reflection from the Moho.

given the average crustal velocities,

$$H = \frac{t_{Ps}}{\sqrt{\frac{1}{V_s^2} - p^2} - \sqrt{\frac{1}{V_p^2} - p^2}}; \tag{5.5}$$

where p is the ray parameter of the incident wave. An advantage of this method is that because the P-to-S conversion point is close to the station, the estimation is less affected by lateral variation and thus provides a good "point" measurement. One problem is the trade-off between thickness and average crustal velocities. However, since t_{Ps} represents the differential travel time of P and S waves in the crust, the dependence of H on Vp or Vs is not strong as long as the ratio of the two $\kappa = Vp/Vs$ remains constant.

For example, using a Vp of 6.3 km/s and Vs of 3.5 km/s for a 65 km thick crust, one gets

$$\Delta H = \frac{\partial H}{\partial V_p}\Delta V_p = 9.4\Delta V_p \text{ (km)},$$

which means that the uncertainty of H is less than 1 km for a 0.1 km/s uncertainty in Vp.

However, the thickness is highly dependent on the Vp/Vs, as shown by

$$\Delta H = \frac{\partial H}{\partial \kappa}\Delta \kappa = -79.7\Delta \kappa \text{ (km)},$$

i.e., a 0.1 change in κ can lead to about 8 km change in crustal thickness. This problem can be eliminated by using the secondary converted phase, $PpPms$, which provides an additional measurement

$$t_{PpPms} = H\left(\sqrt{\frac{1}{V_s^2} - p^2} + \sqrt{\frac{1}{V_p^2} - p^2}\right), \tag{5.6}$$

so one can get an estimate of κ

$$\kappa = \sqrt{\frac{(t_{Ps} + t_{PpPms})^2 + (2pH)^2}{(t_{Ps} - t_{PpPms})^2 + (2pH)^2}}. \tag{5.7}$$

Although it involves the unknown H, the dependence is very weak, as demonstrated by

$$\frac{\partial \kappa}{\partial H} = -2.7 \times 10^{-3} \mathrm{km}^{-1}$$

using the values above.

5.3.3 Data and Results

The one-year experiment has recorded more than 250 teleseismic events in the distance range between 30° and 95°. Many come from the western Pacific subduction zones. There are also a few from the Indian ocean and Mediterranean area, which provide a fairly good azimuthal coverage (Figure 5.2). To cut the P waveform from velocity records, a 150 s time window, starting 30 s before the P onset, is used. Then we perform the time-domain deconvolution to obtain receiver functions for both radial and tangential components. The receiver functions from events clustering within 5° to 10° in epicentral distances and 20° to 30° in azimuths are stacked to suppress noise. The stacked receiver functions within the same azimuth group are plotted as a function of ray parameter. This helps to identify the primary Moho converted phase Ps and the secondary converted phase $PpPms$ because these two have opposite move-out with ray parameter.

Receiver function profiles of all 11 stations are shown in Figure 5.3. There are two directions that have enough events spread from 30° to 95°: the NE and SE directions (Figure 5.2). All profiles shown in the figure are for the SE direction except for station MAQI where no Moho Ps is identified for that direction and events from the NE direction are used. For three stations in northern Tibet, TUNL, BUDO, and ERDO, the Moho Ps phase is missing for the NE direction although it is clear in

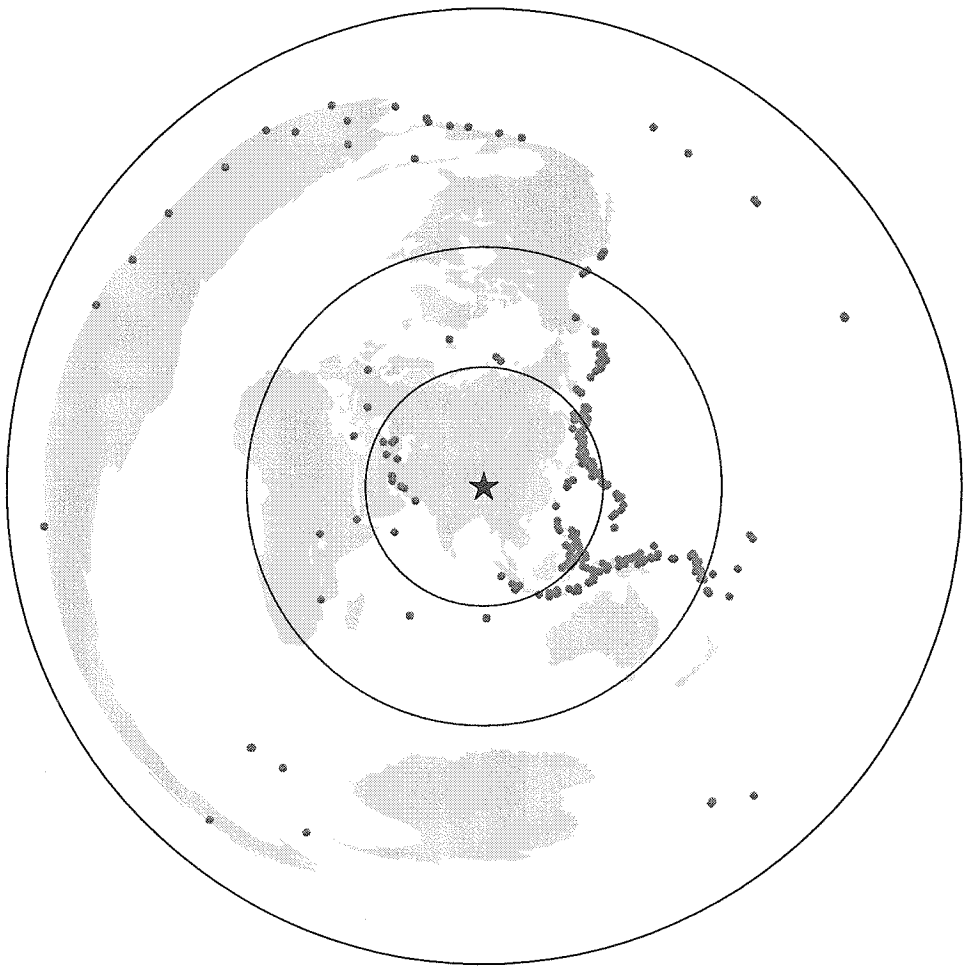

Figure 5.2: Azimuthal-equal distance projection of locations of teleseismic events recorded by the 1991-92 experiment. The distances of 30° and 90° are shown by the two inner circles.

the SE profiles. Receiver functions of these four stations also have large tangential amplitudes which indicate lateral variation. For the rest of the stations, clear Moho Ps is identified in profiles from both directions.

In addition to identifying Moho Ps, we are able to pick up the secondary conversion, $PpPms$, for eight stations (Figure 5.3). The delays of these converted phases with respect to the direct P are listed in Table 5.1, along with the estimated crustal Vp/Vs ratios. Four stations, LHSA, TUNL, USHU, and WNDO, have clear $PpPms$ phase with the expected move-out with ray parameter. At BUDO, $PpPms$ arrivals are apparent for small ray parameters but do not follow the move-out as ray parameters become larger (Figure 5.3). As we pointed out before, as ray parameter increases, so does the incidence angle and $PpPms$ travels longer in the crust and is more easily affected by lateral variation. For ERDO, there are two possible candidates for the $PpPms$, one at about 25 s and the other at about 30 s. The Vp/Vs ratios estimated from these two are 2.01 and 1.75 respectively. *Owens and Zandt* [1997] model broadband teleseismic SV waveforms at ERDO and find an extremely high crustal Vp/Vs ratio (1.98 to 2.08). As we will see later, teleseismic and regional S arrivals at ERDO are significantly delayed. Therefore, we believe that the earlier phase is $PpPms$.

Crustal thickness at each station is then estimated from t_{Ps} and Vp/Vs using Equation (5.5), assuming an average crustal P velocity of 6.3 km/s. As shown before, uncertainty associated with Vp is small. For stations SANG, XIGA and MAQI where Vp/Vs ratio can not be determined, the values at nearby stations are used. The results are listed in Table 5.1.

5.4 Teleseismic P and S Arrival Time Delays

Another useful observation from teleseismic events is their P and S arrival delays with respect to predictions of standard Earth models. Although travel time delay contains contributions from event mislocation, incorrect origin time, and heterogeneity outside the study area, these factors can be removed by using the relative delay with respect to a reference station or the array average because they are common to all stations.

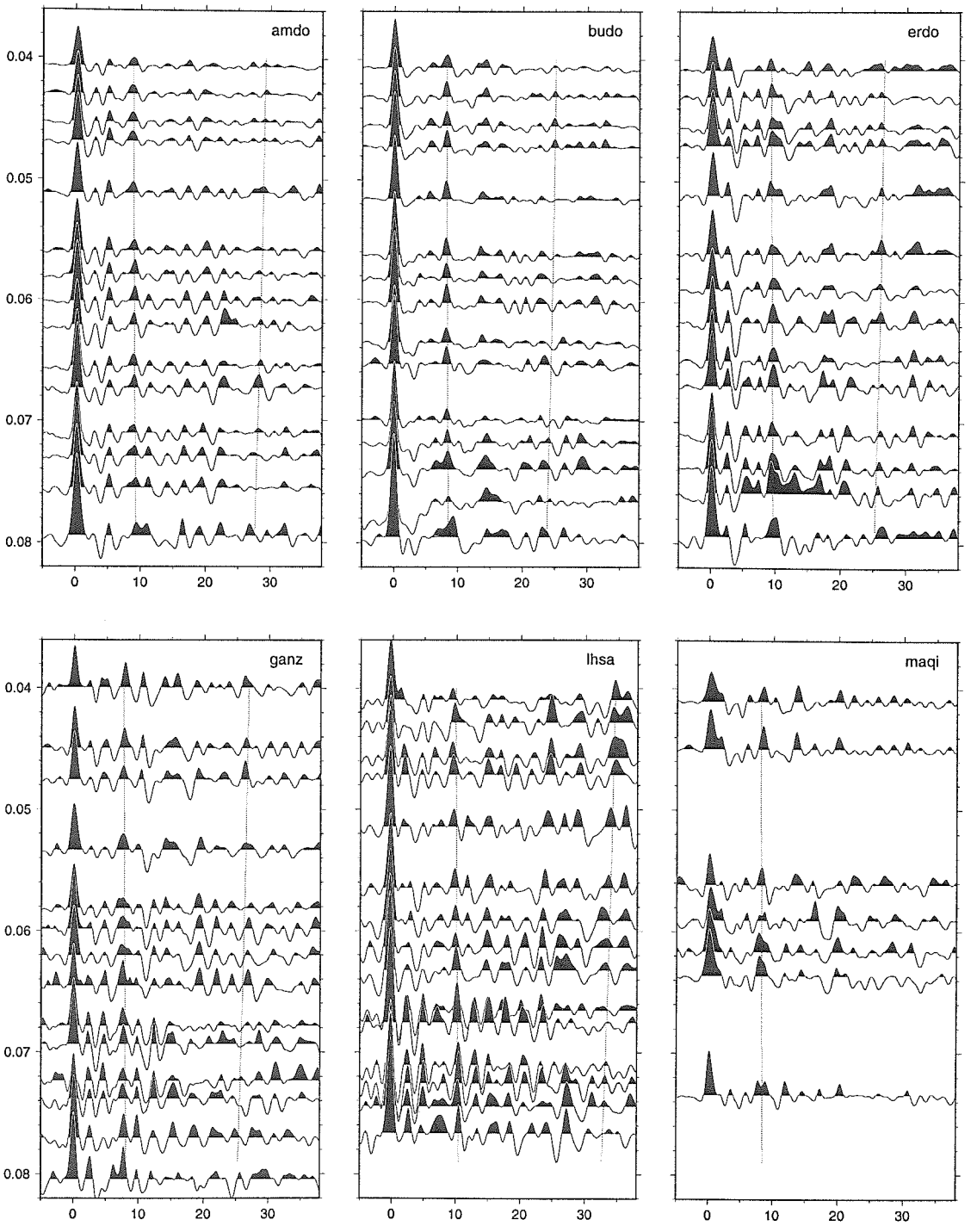

Figure 5.3: Receiver function profiles for all 11 stations. Vertical axes are ray parameter in s/km. Gray lines show Moho Ps, and the later $PpPms$. Note that these phases have small move-out with ray parameter, as indicated by the slopes of the gray lines.

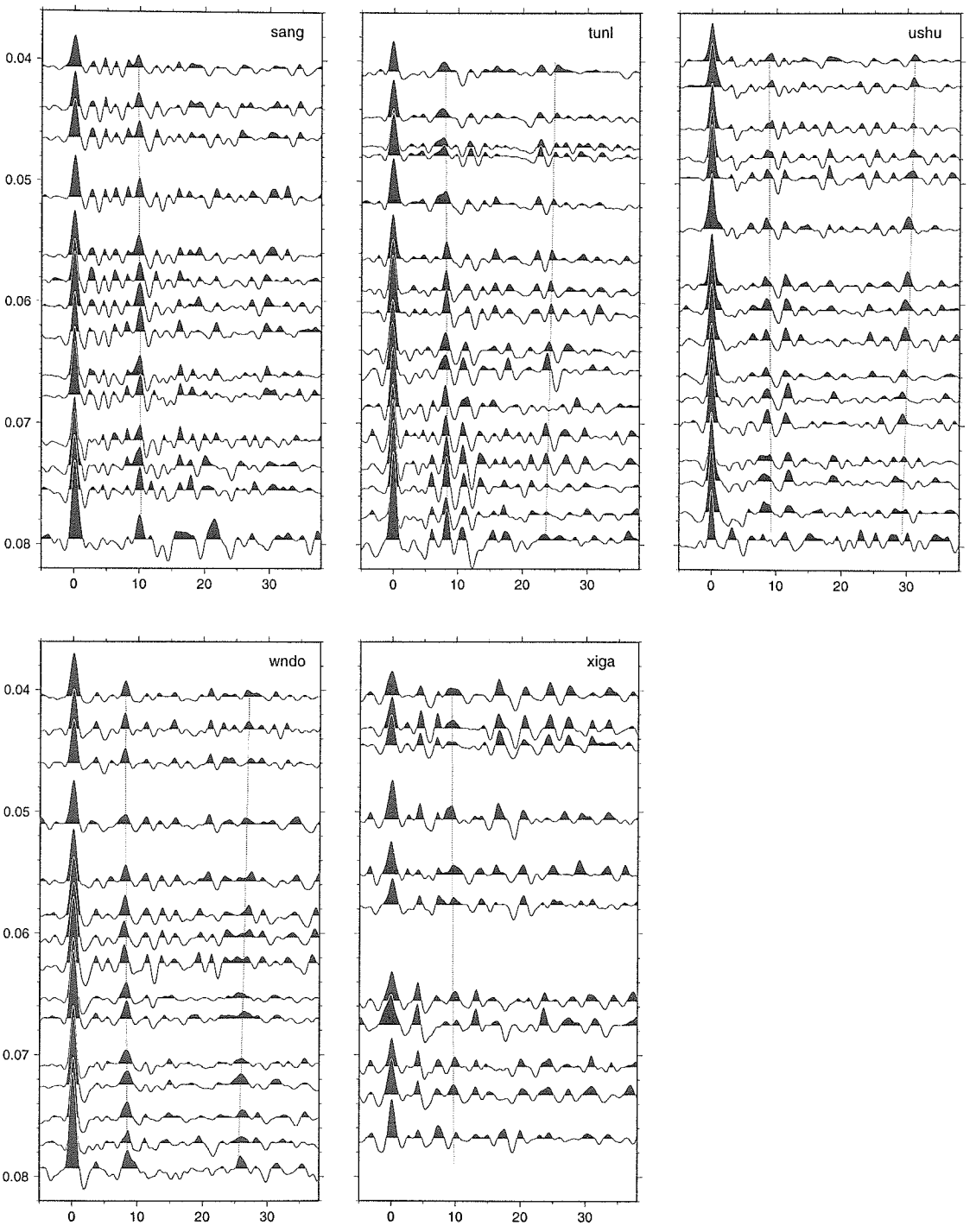

Figure 5.3: Continued from previous page.

Table 5.1: Delays of Ps and $PpPms$ with respect to the direct P. They are measured at ray parameter of 0.06 s/km. Vp/Vs and crustal thickness H are estimated using equations (5.7) and (5.5). For stations where t_{PpPms} is not available, Vp/Vs ratios of nearby stations are used.

Station	t_{Ps}, s	t_{PpPms}, s	Vp/Vs	σ	H, km
AMDO	9.0	28.5	1.82	0.284	66.4
BUDO	8.2	24.5	1.90	0.308	55.5
ERDO	9.4	26.0	2.01	0.336	56.5
GANZ	7.8	26.2	1.75	0.258	62.6
LHSA	10.1	33.7	1.76	0.262	80.3
MAQI	8.2		1.80	0.277	61.9
SANG	10.0		1.80	0.277	75.5
TUNL	8.2	24.4	1.90	0.308	55.1
USHU	9.0	30.3	1.75	0.258	72.5
WNDO	8.2	26.4	1.80	0.277	61.9
XIGA	9.5		1.76	0.262	75.2

σ: Poisson's ratio.

To ensure consistency in identifying P and S arrivals at all stations, we use a multi-channel correlation technique to align station recordings of each event with the P and S onsets. The corresponding time shift between any two stations is then an accurate measurement of relative delay. Figure 5.4 shows an example. We use the vertical component for P arrival time measurement and the SH component for S arrival times. Usually P signals are impulsive and the measurement error is estimated to be less than 0.2 s. S arrivals are longer period because of more severe attenuation. Their waveforms are also complicated by S-to-P precursors. Nevertheless, with the multi-channel correlation technique, S measurement error can be less than 0.5 s.

The azimuthal variations of relative P and S delays are presented in Figures 5.5 and 5.6 respectively. Figure 5.7 shows the P delay histograms. These plots indicate that there are strong lateral variations in the crust and upper mantle, especially for the S velocities. In terms of magnitude of travel time residuals, station ERDO is the most anomalous station for both P and S waves. Several stations show very rapid azimuthal variation, such as TUNL, WNDO, LHSA, and MAQI, suggesting that there are abrupt structural transitions near these stations.

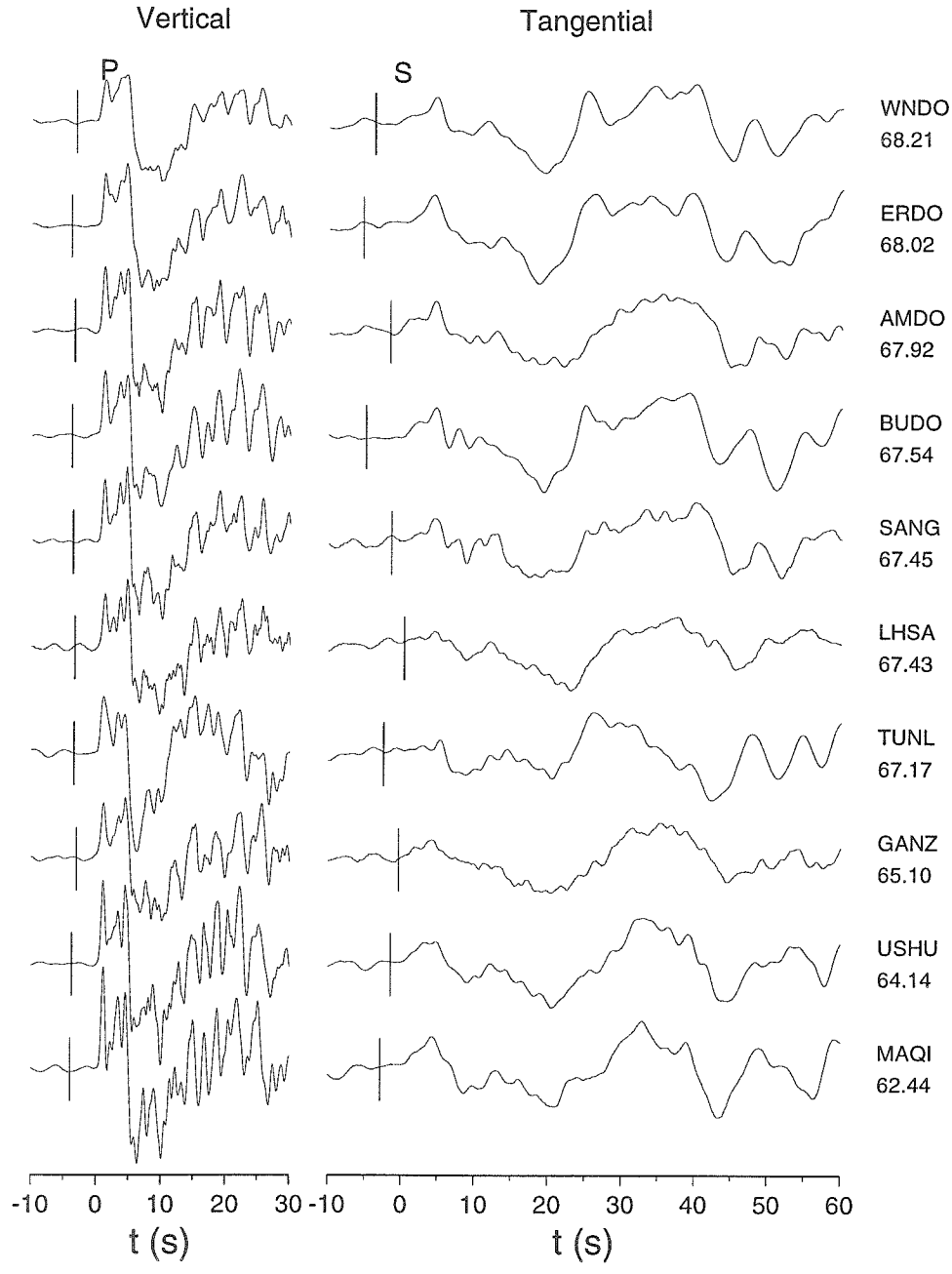

Figure 5.4: An example of velocity records of one teleseismic event; numbers below the station names are epicentral distances in degrees. These records are aligned with P and S arrivals. Vertical line on each trace is the P or S arrival time predicted by the IASPEI91 Earth model.

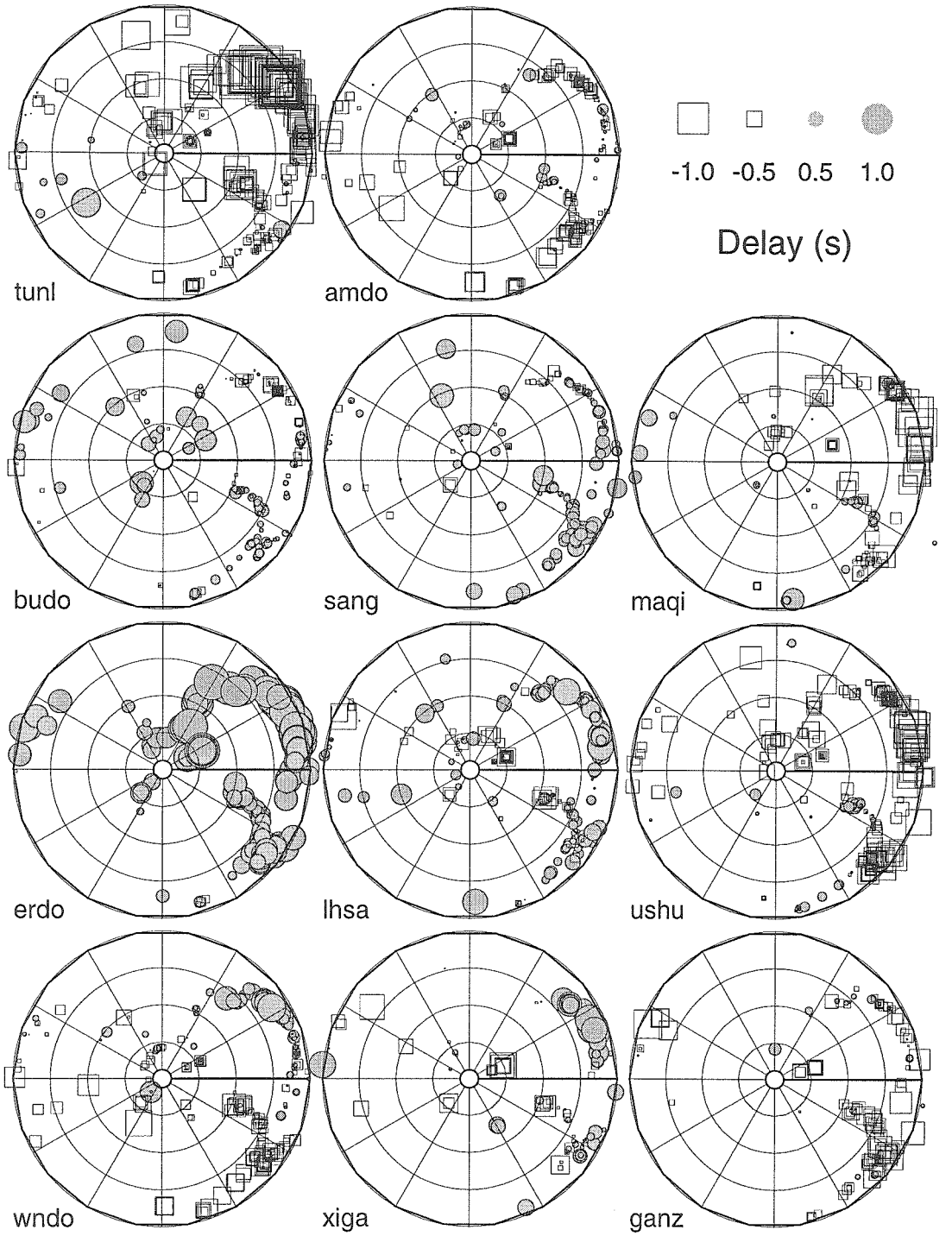

Figure 5.5: Teleseismic P arrival time residual as a function of azimuth and ray parameter. Ray parameters are zero in the center (vertical incidence) and 0.08 s/km at the edge. For each event, the array-averaged residual is subtracted to remove the uncertainties caused by event mislocation, incorrect origin time, and outside heterogeneities.

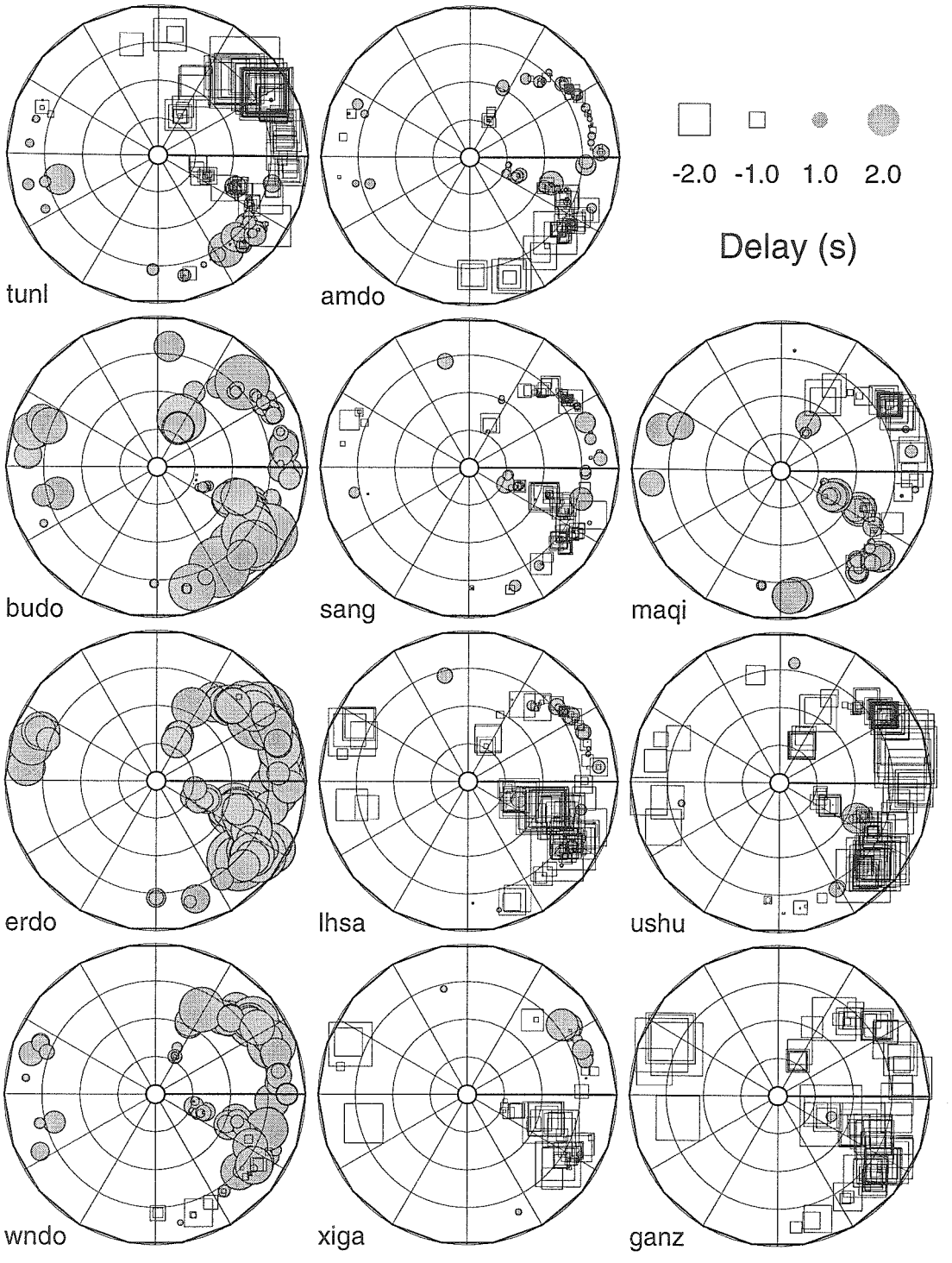

Figure 5.6: Teleseismic S arrival time residual as a function of azimuth and ray parameter. Ray parameters are zero in the center (vertical incidence) and 0.16 s/km at the edge. For each event, the array-averaged residual is subtracted to remove the uncertainties caused by event mislocation, incorrect origin time, and outside heterogeneities.

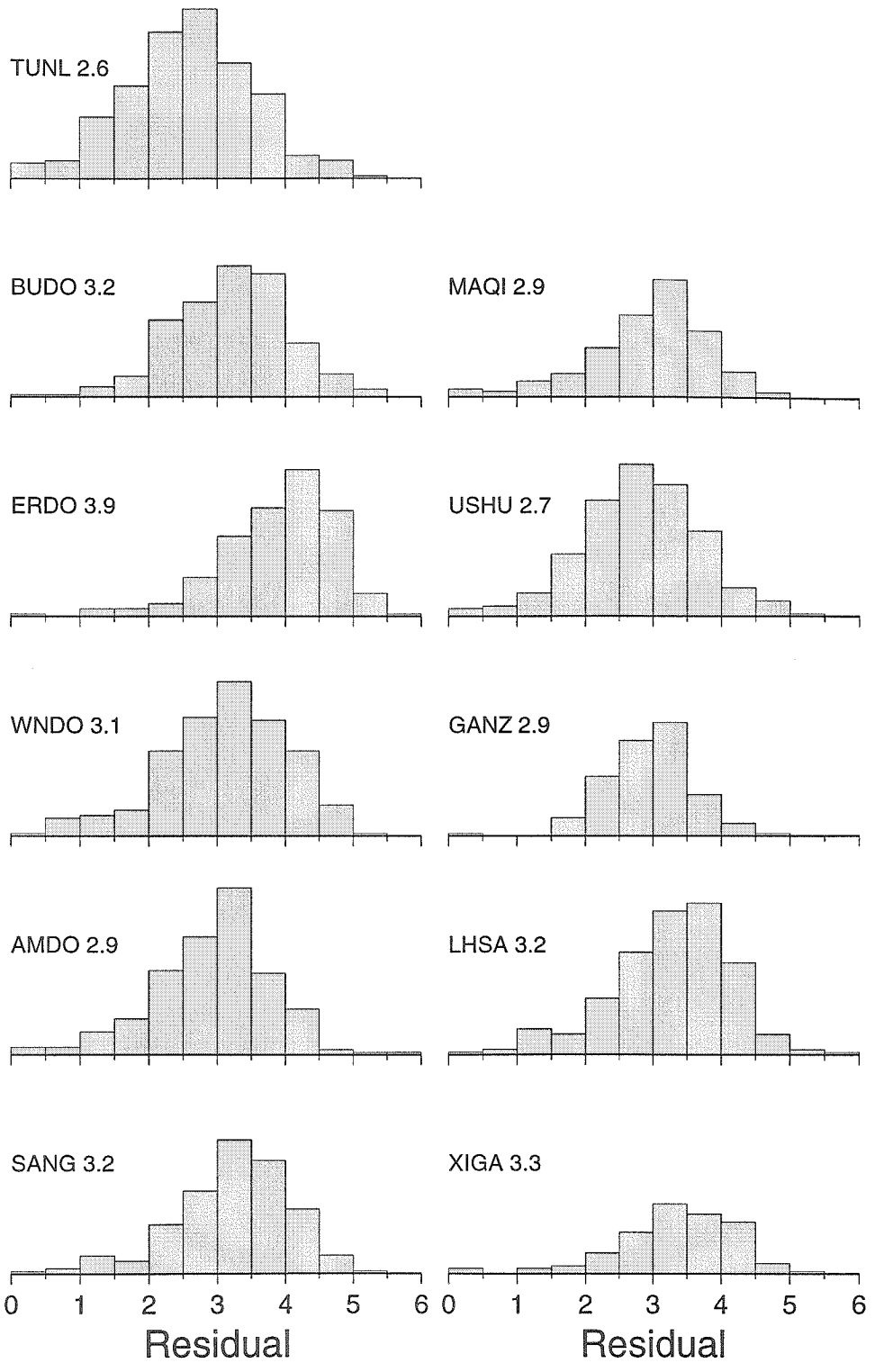

Figure 5.7: Histograms of teleseismic P delays with respect to the IASPEI91 model. Numbers next to the station names are average delays in seconds.

Part of the delay variation is caused by the crustal structural variation, as revealed by previous receiver function analysis. In order to separate the crustal effect from that of the upper mantle, we chose a station located at the center of the plateau, AMDO, as the reference station to calculate the relative delays of all other stations. A crustal thickness correction is applied using typical velocity contrasts between crust and upper mantle: 6.5 km/s to 8.1 km/s for P wave, and 3.7 km/s to 4.7 km/s for S wave. In addition to the thickness correction, the crustal S velocity difference is also corrected using the estimated Vp/Vs ratio at each station. The corrected delays, shown in Figure 5.8, should reflect the upper mantle velocity variation. It is very clear that the upper mantle velocities of northern Tibet are significantly slower than those of southern Tibet, as indicated by the larger delays at BUDO, ERDO, MAQI, and WNDO. Average S delays of the two regions differ by about 2.0 s, corresponding to a 4% velocity difference if it is assumed that the top 200 km of the upper mantle is involved.

5.5 Discussion and Conclusions

Figure 5.9 shows a cross section of crustal thickness, surface elevation and the free-air gravity anomaly along the approximate NS station profile. The small gravity anomaly indicates that the plateau is in isostatic equilibrium. It is interesting to note that, despite the uniform surface topography, there is a tremendous crustal thickness variation. On average the northern Tibetan crust is 20 km thinner than the southern part. There have been several studies indicating a thinner crust in the northern plateau. For example, *Brandon and Romanowicz* [1986] reported a 10 km crustal thinning of the Qiangtang block using pure-path phase velocity measurements of long-period Rayleigh waves. A similar result was reported by *McNamara et al.* [1995] from Pn intercept time difference. Recently, by modeling teleseismic shear-coupled P waves at SANG, WNDO, and ERDO, *Owens and Zandt* [1997] conclude that the crust is 10–20 km thinner in the northern plateau relative to the south. Our result is consistent with previous studies but shows more clearly the transition from the thin

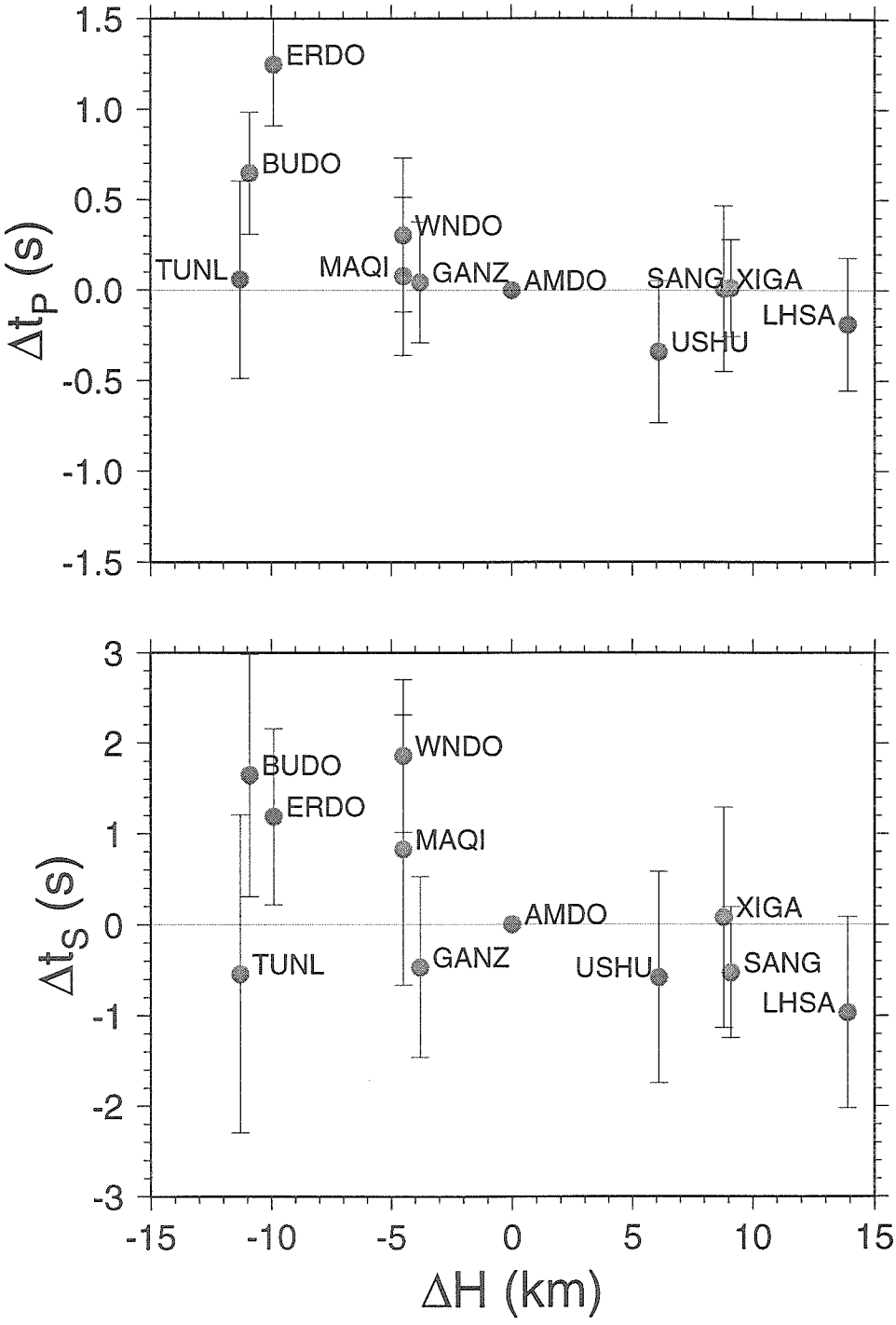

Figure 5.8: Teleseismic arrival delays after the crustal correction (see text). Station AMDO is used as the reference station.

crust to the thick crust (Figure 5.9). The transition seems gradual. However the sparse station distribution is unable to detect some possible abrupt thickness changes unless they occur right below a station, such as the Moho offset near TUNL discussed in Chapter 7.

Coupled with the crustal thickness change is the variation of upper mantle velocities, especially for the S velocity (Figure 5.8). It is suggested that the northern plateau is partly supported by the density of a hot upper mantle [*Molnar*, 1988; *Owens and Zandt*, 1997]. With the azimuthal variation of teleseismic S delays at individual stations (Figure 5.6), we can confine approximately the extent of the upper mantle low S velocity anomaly (Figure 5.10): its northern boundary should lie near TUNL, as delays flip sign for northern azimuth events. The southern boundary is located between WNDO and AMDO. To the east, the anomaly reaches MAQI but should be limited by USHU to the southeast. This area coincides with the zone of high-frequency Sn attenuation [*Ni and Barazangi*, 1983; *McNamara et al.*, 1995].

Our result shows a high Vp/Vs ratio (1.9–2.0) in the northern Tibetan crust. Similar high ratios are required by modeling shear-coupled P waves [*Owens and Zandt*, 1997]. Our Vp/Vs ratios are based on identifying the secondary teleseismic converted phase $PpPms$. There are some ambiguities on this phase at ERDO and BUDO. Although large teleseismic S delays exist for these stations, the low S velocity anomaly could lie in the upper mantle. As an attempt to constrain the structural variation in northern Tibet, we use the SH records of BUDO from the three sub-crustal earthquakes discussed in Chapter 3. The waveforms show clearly the direct S arrival (sS) and the crustal multiples ($sSmS$ and so on) (Figure 5.11). Because the hypocenters are nearly 1000 km from the station and are located only 10 to 20 km below the Moho, the direct S travels almost horizontally in the uppermost mantle before it enters the crust near BUDO. The first multiple $sSmS$, which shares the same path with sS in the uppermost mantle, has two additional ray legs sampling the crustal column beneath ERDO. Comparing the observed waveforms with synthetics shows that the $sSmS$ is delayed with respect to sS by 2.8 s while all later multiples are only delayed a few tenths of a second with respect to $sSmS$ (Figure 5.11). This indicates

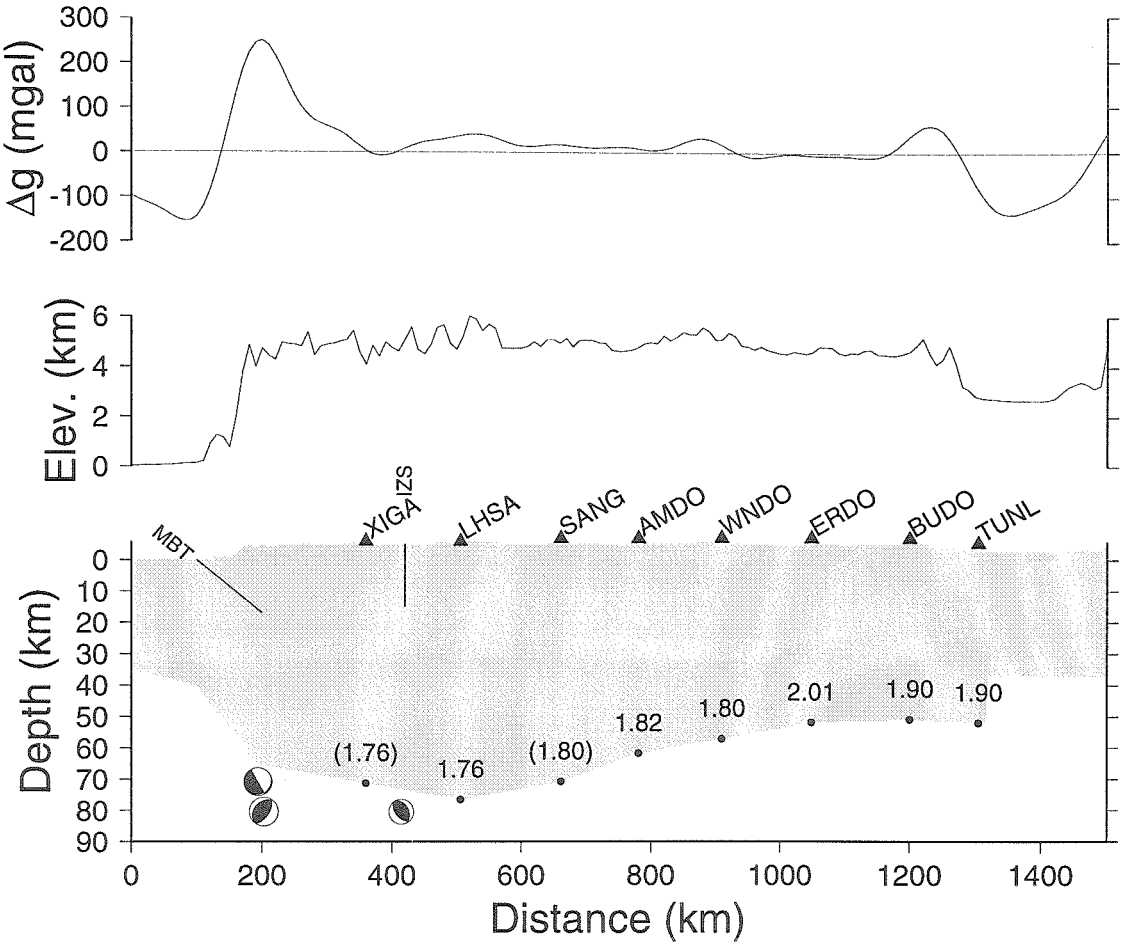

Figure 5.9: A cross section along the approximate NS station profile showing the free-air gravity anomaly (from EGM96 global model [*National Imagery and Mapping Agency, NASA/Goddard Space Flight Center*, 1997]), surface elevation, and the crustal thickness variations. The location of the profile is shown in Figure 4.1. Number above each data point is the Vp/Vs ratio from the receiver function analysis, except for those in parentheses where the values of nearby stations are used. MBT: Main Boundary Thrust; IZS: Indo-Zangbu Suture. Also shown in the figure are the source mechanisms of the three sub-crustal earthquakes discussed in Chapter 4. The Moho step beneath TUNL is discussed in Chapter 7.

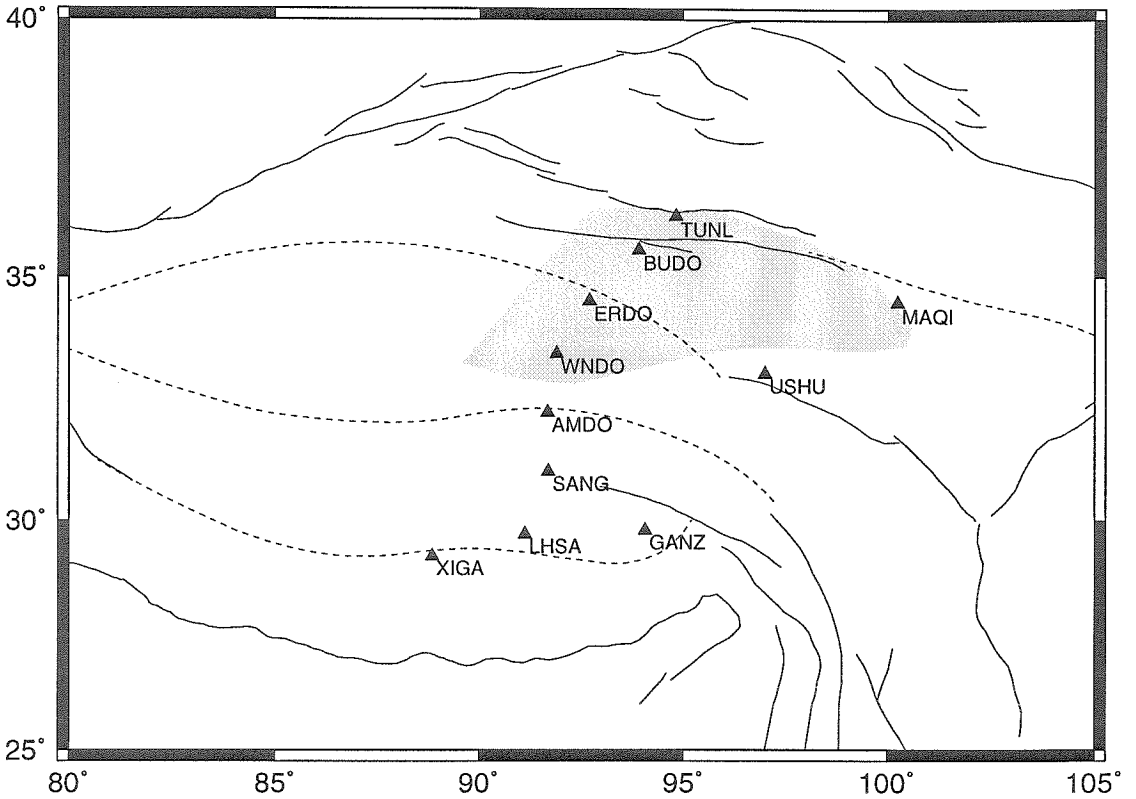

Figure 5.10: Map view of the upper mantle low velocity zone inferred from the azimuthal variation of teleseismic arrival delays (see text).

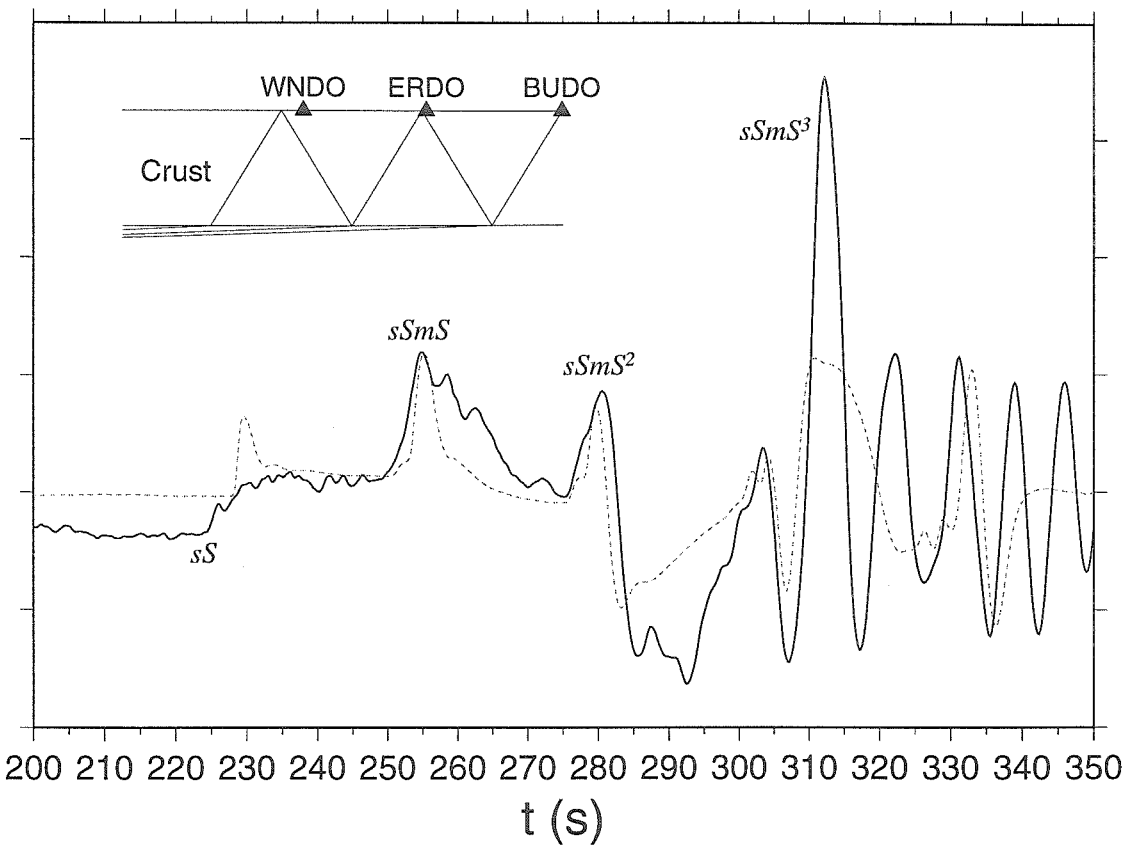

Figure 5.11: SH waveform of BUDO from a sub-crustal earthquake (Event 095). The synthetic (dashed line) is aligned with the data at the $sSmS$ arrival.

that the S velocity in the crustal column beneath ERDO is about 5% slower than the 1-D model, but the S velocity in the crust beneath WNDO and further south is only about 1% slower.

The high Vp/Vs ratios, and therefore high Poisson's ratio, in the northern Tibetan crust suggests high crustal temperatures and most likely partial melting [*Zhu et al.*, 1995; *Owens and Zandt*, 1997]. A hot mantle and partially molten middle-lower crust explains the observed high-frequency Sn attenuation and Cenozoic volcanism in north-central Tibet.

Chapter 6
Lateral Variation in Crustal Structure of the Northern Tibetan Plateau Inferred from Teleseismic Receiver Functions

6.1 Abstract

We investigate lateral variations in crustal structure across the northern boundary of the Tibetan Plateau using the receiver functions at three broadband stations deployed during the 1991-1992 Tibet PASSCAL experiment. The first 5 s of the receiver functions vary systematically with back-azimuth: the radial receiver functions are symmetric across the NS axis while the tangential receiver functions are anti-symmetric across this axis. This symmetry can be modeled by EW striking dipping interfaces in the upper-middle crust. The strike direction is consistent with the EW trend of surface geology. Modeling a P-to-S converted phase in the receiver functions at each station suggests that there is a mid-crustal low velocity layer with its upper boundary dipping 20° to 30° to the south. In addition, a shallow northwards-dipping interface is responsible for the "double-peaked" direct P arrivals in the radial receiver functions and large tangential motions at one of the stations. The low velocity layer, together with other geological and seismological observations, suggests that there is a hot, possibly partial melt zone in the middle crust of northern Tibet. Alternatively, dipping velocity interfaces might be associated with some buried thrust faults in the upper crust which accommodated crust shortening during the plateau formation.

6.2 Introduction

The Tibetan Plateau, bounded by the Kunlun mountains in the north and Himalayas in the south, with an average elevation of 5 km and an areal extent of nearly 3×10^6 km^2, has long been an interesting and challenging subject in the Geosciences. The uplift of the Tibetan Plateau is the result of the collision of the Indian plate with Eurasia which began during Middle Eocene, 45 million years ago. However, the details of the uplift mechanism remain controversial. Among the most popular uplift models are the underthrust model and its variants [*Argand*, 1924; *Zhao and Morgan*, 1985; *Beghoul et al.*, 1993], the crustal shortening and thickening model [*Dewey and Bird*, 1970; *Dewey and Burke*, 1973], and the lateral crustal extrusion model [*Molnar and Tapponnier*, 1977; *Tapponnier et al.*, 1982]. Due to insufficient information on the lithospheric structure of the plateau, it is difficult to discriminate among different uplift models.

Most geological and geophysical investigations on the plateau have been concentrated in southern Tibet, near the Himalayas. Comparatively, the structure near the northern boundary of the plateau was poorly resolved. Recently, in a joint research project conducted by the Institute of Geophysics, State Seismological Bureau, China, the University of South Carolina, and the State University of New York at Binghamton, 11 broadband three-component seismic recorders were deployed on the plateau for one year (Figure 3.2). Three stations, TUNL, BUDO and ERDO, placed across the northern boundary of the plateau, provided an opportunity to study the crustal and upper mantle structure of this area. We use teleseismic P waveforms to study the lateral variations of the crustal structure. We show that there is strong lateral variation in the crust of the northern plateau and that most of this variation is caused by EW striking dipping velocity interfaces in the upper-middle crust.

6.3 Receiver Functions and Dipping Interfaces

Teleseismic P waveforms contain information about near source and near receiver structure. Using the method of *Langston* [1979], the source and distant path effects can be removed from P waveforms by deconvolving the vertical from the horizontal components. The source-equalized teleseismic waveform is called the receiver function and is most sensitive to the P-to-S conversions from structures beneath the recording site [*Owens et al.*, 1984].

The radial receiver functions are often modeled by horizontally stratified velocity structure using a time-domain inversion technique [*Owens et al.*, 1984; *Ammon et al.*, 1990]. This method has been applied to numerous areas and is efficient in estimating the velocity-depth variation of the crust. However, if the tangential receiver function is comparable in amplitude to the radial receiver function, which indicates strong lateral heterogeneity beneath the site, modeling the details of the radial receiver function with horizontally stratified velocity will produce erroneous results.

One special case of lateral heterogeneity is a dipping planar velocity interface. In this case, both the radial and tangential receiver functions vary with back-azimuth in a predictable pattern. In Figure 6.1, we show theoretical receiver functions for a model that contains a mid-crustal low velocity layer with the upper boundary dipping 20° to the south. The interface is at depth of 20 km where the S velocity is 3.5 km/s above and 3.0 km/s below. Theoretical are calculated using a 3-D ray-tracing method of *Langston* [1977]. The ray parameter is 0.068 s/km, which corresponds to an epicentral distance of 50°. The waveform variation with back-azimuth is systematic: the radial receiver functions are symmetric across a line parallel to the dip direction of the interface, while the tangential receiver functions are anti-symmetric about this direction (indicated by arrow in Figure 6.1). The tangential receiver function is largest when the P wave approaches from the strike direction and is zero when the ray comes from a direction parallel to the dip direction. The P-to-S converted wave generated at the dipping interface is indicated in the figure. This negative-amplitude phase emerges for southern back-azimuths, has a maximum amplitude from the dip

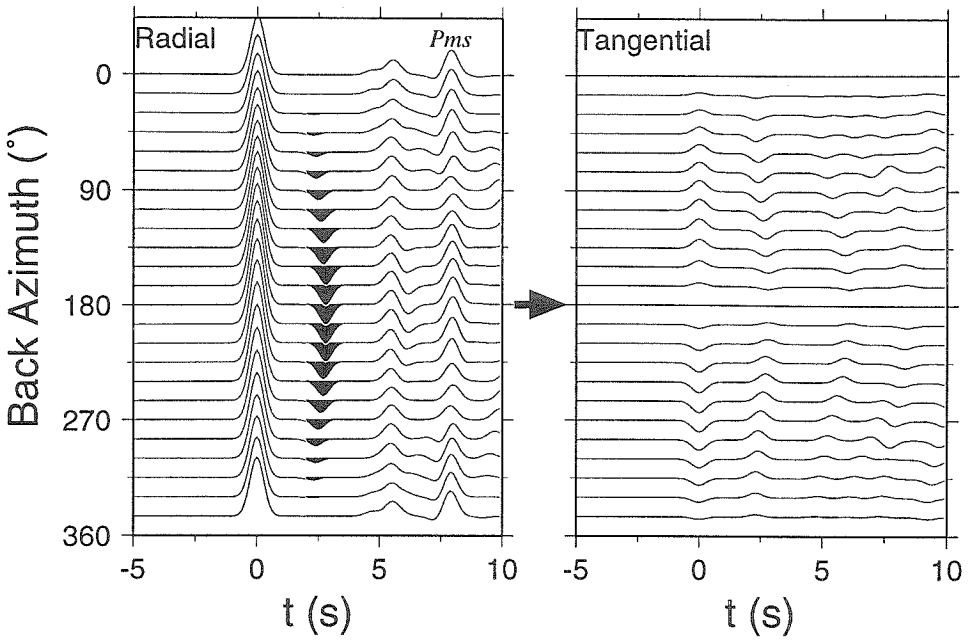

Figure 6.1: Theoretical receiver function for a model containing a mid-crustal low velocity layer with its upper boundary dipping 20° to the south. P-to-S converted phase from the dipping interface is indicated. *Pms* is the P-to-S converted wave from Moho.

direction, and vanishes gradually away from the dip direction.

Therefore, if a dipping interface is the major cause of lateral heterogeneity under a station, it is easy to determine the dip and strike directions by examining a back-azimuthal profile of receiver functions. The dip angle, velocity contrast, and the depth of the interface can be estimated by modeling the amplitude and arrival time of the converted phase from the interface. A trade-off, however, exists between the dip angle and the velocity contrast across the interface [*Owens and Crosson*, 1988]. In Figure 6.2a,b we show the variation of radial and tangential amplitudes of the P-to-S converted phases with back-azimuth at different dip angles. Figure 6.2c is the variation of maximum radial amplitude with velocity below the interface, while fixing the velocity above at 3.5 km/s. The dip angle controls the shape of the amplitude variation with back-azimuth and also affects the maximum radial amplitude, while the velocity difference across the interface contributes mainly to the maximum amplitude. However, to produce the same maximum amplitude with a velocity contrast differing by 0.1 km/s, the dip angles will differ more than 10° (Figure 6.2c), which

has an observable shape difference in the amplitude variation with back-azimuth (Figure 6.2a,b). Thus, if the data have sufficient back-azimuth coverage, reasonable constraints can be made on the dip angle and velocity contrast across the interface.

6.4 Receiver Function Variation with Back-azimuth

More than 300 teleseismic events ranging from 35° to 95° in epicentral distance were recorded during the experiment. Instrumentation details about the experiment can be found in *Owens et al.* [1993]. A preliminary study of the receiver functions at three sites (TUNL, WNDO and XIGA) located in the northern, central, and southern plateau showed the great thickness of the crust (60 to 80 km) and a difference in velocity structures between the north-central and southern Tibetan Plateau [*Zhu et al.*, 1993]. Large tangential motions were also observed at TUNL and XIGA.

Three stations, TUNL, BUDO, and ERDO, were located across the north boundary of the plateau which is defined by an EW striking left-lateral fault system, the Kunlun Fault System (Figure 3.2). The elevation increases from 3 km in the Qaidam Basin in the north to more than 4.5 km on the plateau. During several recent geotraverses some thrust faults were discovered in northern Tibet, for example, the South Qaidam Border Thrust Fault and Fenghuoshan thrust faults [*Kidd et al.*, 1988]. The surface geology in this area includes highly deformed Permian subduction-related rocks and Upper Paleozoic plutons [*Dewey et al.*, 1988].

Excellent back-azimuthal coverage enables us to study the lateral variations of the crustal structure using the variation of the receiver function waveforms. The three-component teleseismic recordings were cut with a time window of 180 s length beginning 60 s before the direct P arrival. The horizontal components were then rotated to radial and tangential directions and deconvolved with the vertical component in the frequency domain. A Gaussian parameter of 2.5 was used to exclude frequencies above 1 Hz. To stabilize the deconvolutions, we used a range of water-levels from

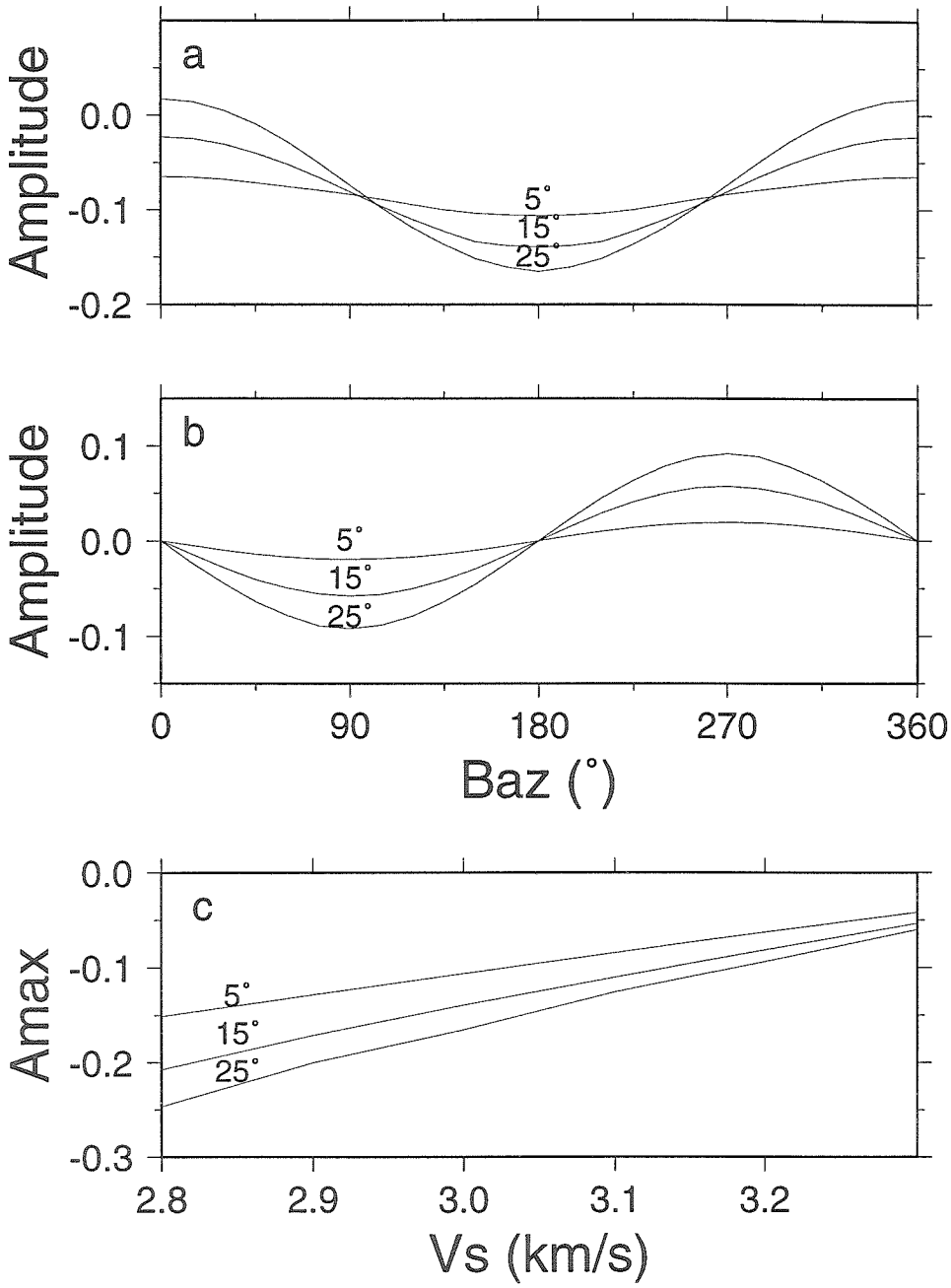

Figure 6.2: Azimuthal variation of radial (a) and tangential (b) amplitude of the converted phase from the dipping interface at different dip angles. (c) Variation of the maximum amplitude with velocity below the interface at different dip angles. The S velocity above the interface is fixed at 3.5 km/s.

Table 6.1: Back-azimuth and distance range of events in each stacking suite

BUDO					TUNL					ERDO				
ϕ	$\delta\phi$	Δ	$\delta\Delta$	N	ϕ	$\delta\phi$	Δ	$\delta\Delta$	N	ϕ	$\delta\phi$	Δ	$\delta\Delta$	N
5	0	46	0	1	6	2	45	1	2	27	2	94	10	4
27	2	92	10	5	29	10	89	27	8	43	10	61	20	11
44	10	58	21	12	45	7	58	17	11	58	10	44	8	30
59	12	42	9	34	59	7	42	8	33	70	6	39	1	5
79	10	38	3	21	66	8	38	4	15	79	6	39	3	8
89	4	42	5	7	80	8	37	4	25	89	9	44	9	5
102	9	50	3	4	90	8	40	5	12	112	9	75	26	22
114	9	73	32	29	102	10	49	3	6	128	12	47	21	31
130	15	47	22	34	114	10	76	32	27	143	6	50	4	4
145	5	50	4	2	128	9	45	22	24	161	0	42	0	1
164	9	42	6	6	136	12	47	12	25	164	0	39	0	2
181	0	51	0	2	152	8	48	2	4	179	0	50	0	2
211	0	58	0	1	167	2	41	1	8	210	0	57	0	1
243	0	40	0	1	182	0	52	0	2	272	6	33	3	2
255	0	51	0	1	212	0	59	0	1	287	0	37	4	2
267	1	32	1	2	243	0	41	0	1	292	2	45	11	3
275	0	36	0	1	255	0	60	14	2	303	0	53	0	1
289	6	42	18	6	267	1	33	1	2					
303	0	53	0	1	273	3	37	0	2					
346	0	55	0	1	285	1	38	4	2					
					294	12	46	15	5					
					346	0	54	0	1					
total				171					217					132

ϕ, Δ: back-azimuth and distance range in degrees; N: number of events.

0.1 to 0.0001. Details on the calculation of receiver functions are described elsewhere (e.g., *Langston* [1979]; *Owens et al.* [1984]).

For each station, the teleseismic events are divided into groups of back-azimuth range less than 10°, according to the waveform similarity of the receiver functions. We found that differences in epicentral distance do not strongly affect the waveforms, so some of the groups span a distance range of more than 20°. The receiver functions in each group are then stacked. The back-azimuthal/distance range and the number of events for each stacking suite are listed in Table 6.1.

Figure 6.3 shows the back-azimuthal profiles of the stacked receiver functions at

the three stations. It is clear that there is strong lateral variation in the upper-middle crust of this region as evidenced by the variation of radial receiver function waveform and large tangential motions at all three stations. Also, the waveforms vary with back-azimuth in the pattern predicted by dipping interfaces described above. Both the symmetry of radial receiver functions and the anti-symmetry of tangential receiver functions across a roughly NS direction are noticeable in the first five seconds of the waveforms. The tangentials are nearly zero in the NS direction (as indicated by the horizontal arrows in Figure 6.3) and the largest tangential motions are generated by P waves arriving from the east and west directions (back-azimuths of about 90° to 100° and 270° to 280°) with opposite polarities.

6.5 Dipping Velocity Interfaces Beneath Northern Tibet

A prominent feature in the radial receiver functions is a mid-crustal P-to-S converted phase observed in the back-azimuth range of about 100° to 300° (indicated with gray bars in Figure 6.3). This negative-polarity arrival is strongest at BUDO (time delay 3.3 s with respect to direct P arrival) and also can be identified at TUNL (2.4 s) and ERDO (3.8 s). Since there is no large converted phase before it, this phase is not a multiple converted phase. The negative polarity indicates that this phase is generated at the top of a low velocity layer. The amplitude variation of this phase with back-azimuth is caused by the southward dip of the interface (as demonstrated by the theoretical receiver functions in Figure 6.1).

We measured the amplitudes of this phase on both the radial and tangential receiver functions from different back-azimuths and fit them by trial-and-error forward modeling. From our preliminary receiver function analysis [*Zhu et al.*, 1993], we fixed the velocity above the interface at 3.5 km/s and varied the velocity below the interface from 2.8 km/s to 3.3 km/s. A range of dip angles from 5° to 35° were tested. We used the maximum radial amplitude to estimate the velocity contrast and used the shape of

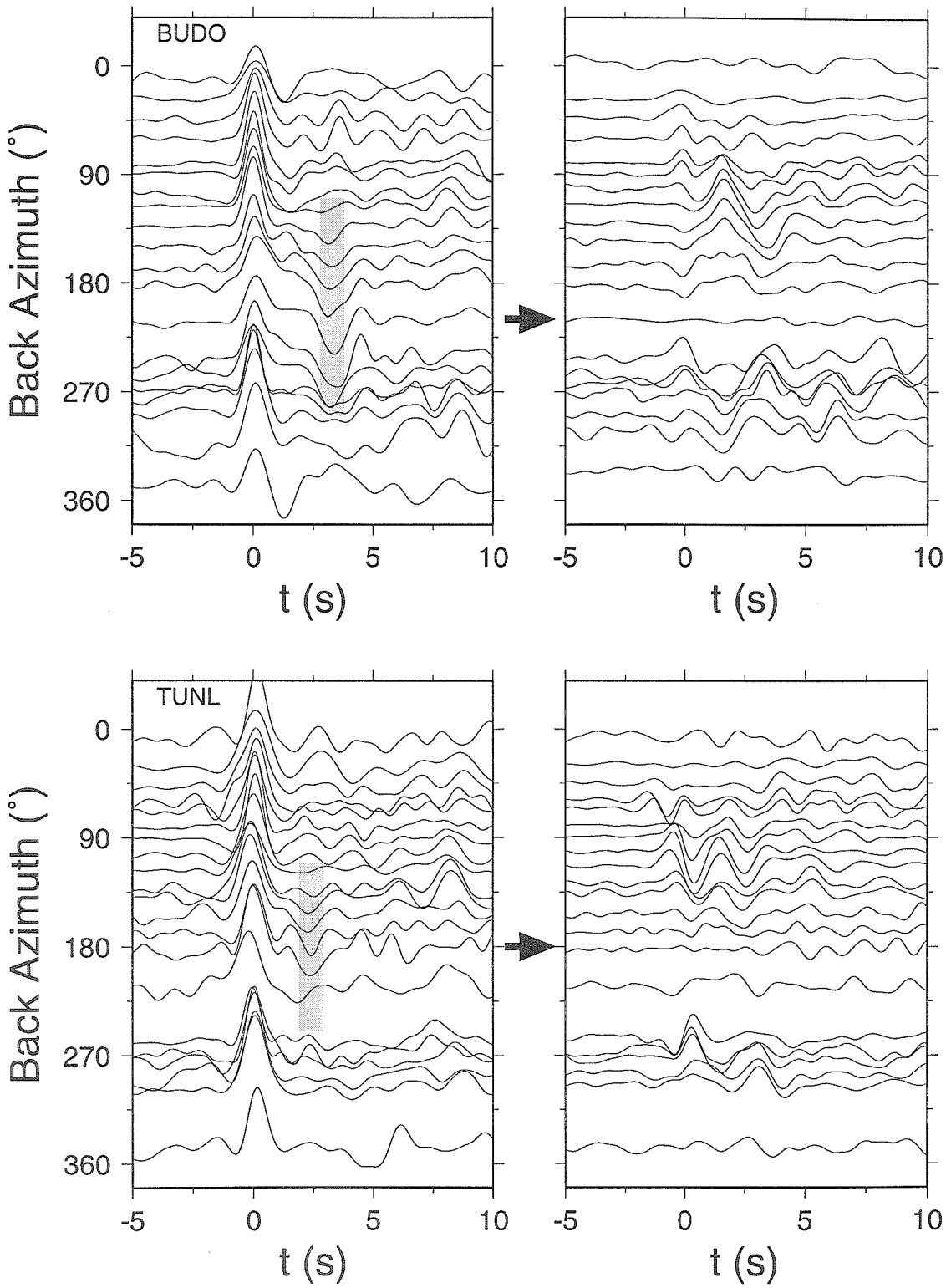

Figure 6.3: Receiver functions at stations BUDO, TUNL, and ERDO (on next page). Horizontal arrow points to the back-azimuth with minimum tangential energy.

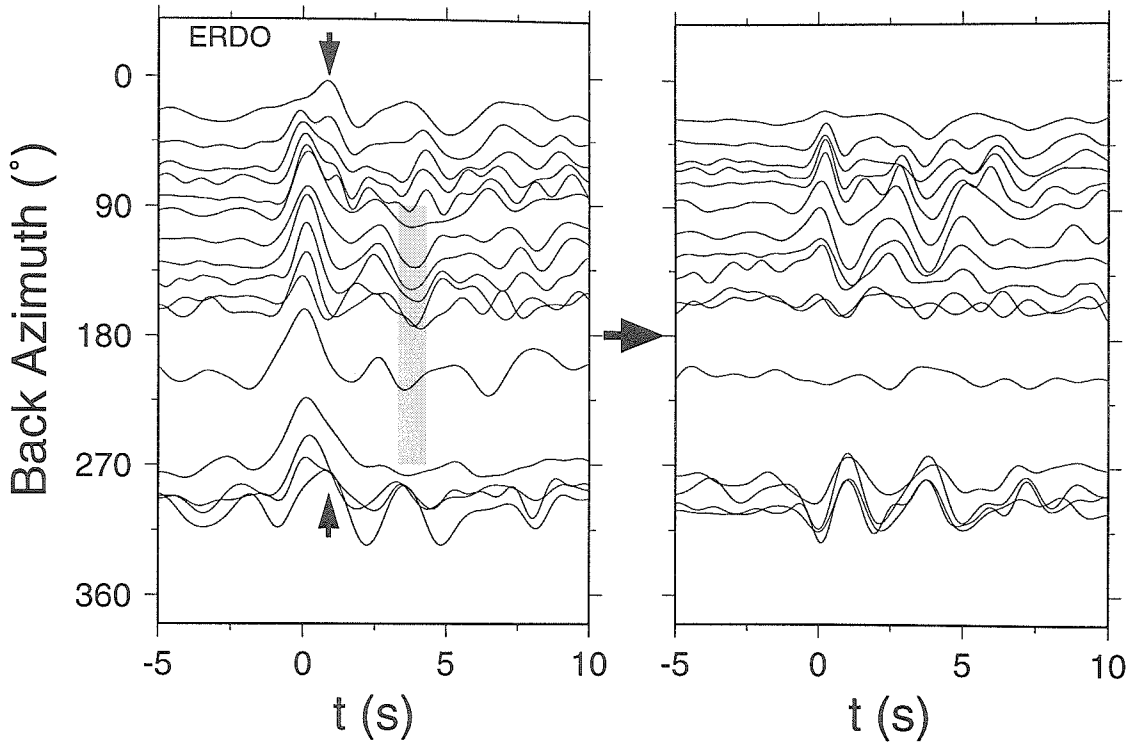

Figure 6.3: Continued from previous page. The apparent time shifts of direct P arrivals are indicated by the vertical arrows.

the amplitude variation with back-azimuth to estimate the dip angle and direction. The modeling results are listed in Table 6.2. Figure 6.4 presents the comparisons between data and the values predicted by the dipping models.

There is very good back-azimuth sampling at BUDO which leads to substantial constraints on the velocity below the interface (2.8-2.9 km/s), and the dip angle (20°-25°). The strike is N110°-120°E. Both the radial and tangential amplitude variations are well modeled by the dipping structure (Figure 6.4). For station TUNL, although the maximum amplitude of the converted phase at this site is less than that at BUDO, the amplitude has a very rapid variation with back-azimuth, implying steep dip angle. The velocity below the interface from the modeling is 3.0±0.1 km/s. Dip angle is 30°±5° with strike N90°±10°E. The actual dip angle seems to be even larger. However, with a planar dipping interface, a dip angle larger than 35° for the given velocity contrast will make the transmitted P at the interface turn into a head wave. Probably, a curved interface is needed to match the amplitude variation at TUNL. Data at ERDO are relatively scattered, especially on the tangential component. Part

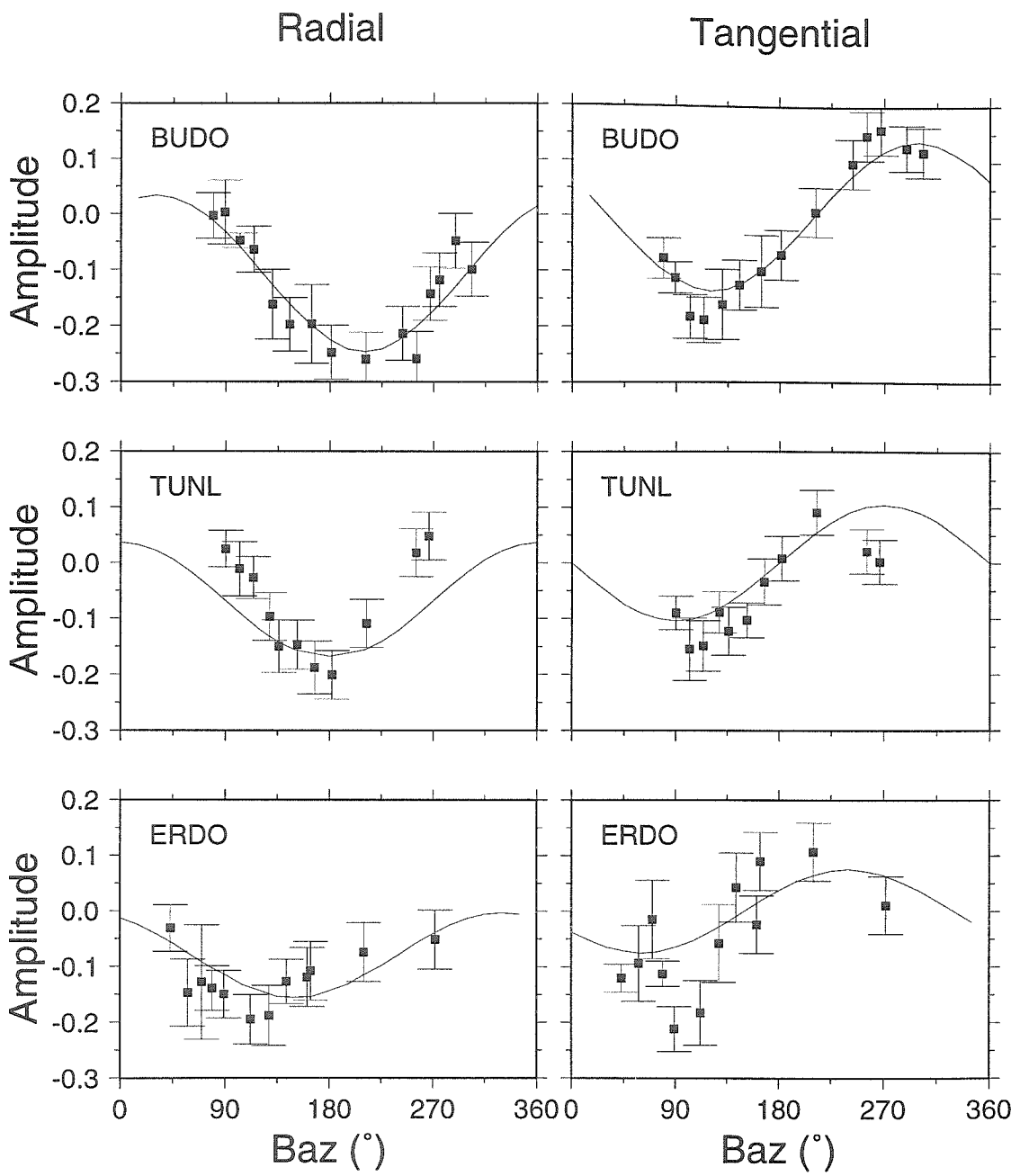

Figure 6.4: The amplitudes of the mid-crustal converted phases and theoretical modelings (solid lines). The modeling results are listed in Table 6.2.

Table 6.2: Velocity structures from the forward modeling

Layer	Th., km	V_p, km/s	V_s, km/s	dip	strike
		BUDO			
1	24	6.06	3.50	25	120
2	–	4.85	2.80		
		TUNL			
1	15	6.06	3.50	30	90
2	–	5.20	3.00		
		ERDO			
1	4	4.33	2.50	15	270
2	22	6.06	3.50	20	60
3	–	5.20	3.00		

of the reason is due to a shallow structure we will discuss later. The estimated velocity below the interface is 3.0±0.1 km/s and the dip angle is 20°±10° with strike N60°±20°E. Large uncertainty exists for this station. The depth of the dipping interface at each station is determined by the arrival time of the converted phase, after assuming an average upper crustal S velocity of 3.5 km/s and a normal V_p/V_s ratio. The results are 15 km for TUNL, 24 km for BUDO, and 26 km for ERDO.

Another feature of the radial receiver functions is an apparent time shift of direct P arrivals from back-azimuths of 30° and 315° at ERDO (indicated by the vertical arrows in Figure 6.3). This shift is produced by a shallowly dipping interface that reduces the direct P arrival amplitude and generates a large Ps wave that appears to be the first arrival, as discussed by *Owens and Crosson* [1988]. By adding a top layer beneath ERDO and adjusting the depth, dip and velocity contrast of the bottom boundary, we can model both the radial and tangential waveform of the first 2 to 3 s quite well (Figure 6.5). The shallow layer has a thickness of 4 km with bottom interface dipping 15° to the north (see Table 6.2).

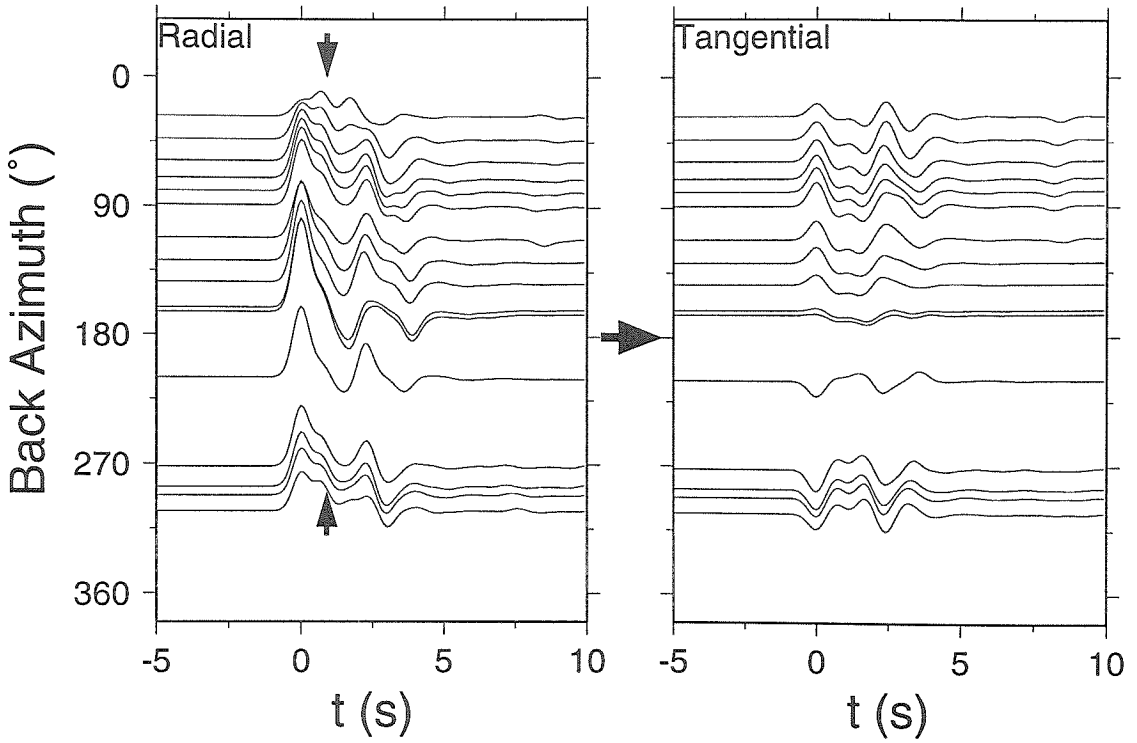

Figure 6.5: Theoretical receiver functions for station ERDO. Velocity model is listed in Table 6.2.

6.6 Low Velocities and High Temperature in the Northern Tibetan Plateau Crust

Our modeling shows that there is a low velocity layer (LVL) at depth range of 15 to 25 km in the crust of the northern Tibetan Plateau. Due to the difficulty of identifying the converted phase from the bottom of the LVL, we can not determine its thickness. The S velocity reduction of this layer could be as large as 15 to 20%. The LVL is consistent with previous results of surface wave studies that show that the plateau, especially the north-central part, has a very low average crustal velocity [*Romanowicz*, 1982; *Brandon and Romanowicz*, 1986].

Some interesting implication about the crustal structure can be derived from the LVL. Earthquake relocations showed that most of the seismicity in the Tibetan Plateau is confined to the top 5 to 10 km of the crust [*Molnar and Chen*, 1983; *Zhao and Helmberger*, 1991; *Randall et al.*, 1995]. It was estimated that earthquake cut-off

temperature for continental crust is about 250° to 450°C [*Chen and Molnar*, 1983]. Thus, shallow seismicity indicates high geothermal gradient. *Kern and Richter* [1981] calculated temperature derivatives of V_p and V_s from laboratory measurements and showed that in a warm geotherm situation, velocity inversion can occur for rocks rich in olivine or quartz. However, the total velocity decrease by a high temperature gradient is limited (less than 13%, *Meissner* [1986]). For a larger velocity reduction, almost necessarily partial melt is involved. Dehydration reactions could be another reason, but is less likely in our case.

Partial melting is consistent with the observation of high frequency S wave attenuation in north-central Tibet [*Barazangi and Ni*, 1982; *Ni and Barazangi*, 1983; *McNamara et al.*, 1995; *Zhu and Helmberger*, 1995]. It is also supported by abundant evidence for late-Cenozoic volcanism in the area. *Molnar et al.* [1987] reported discovery of a suite of igneous rocks that includes tourmaline-bearing granite, two-mica granite, and sanidine-bearing welded tuff near the Ulugh Muztagh area, northern Tibet. These very acidic rocks were believed to result from the melting of crustal rocks. Basaltic volcanic rocks were also reported [*Deng*, 1978], which suggests that an upper mantle component is also involved [*Molnar*, 1988].

High crustal temperatures could arise from the concentration of radiogenic crustal material as a result of crustal shortening during the formation of the plateau [*Zhao and Helmberger*, 1991], or due to the high heat flux from abnormal upper mantle under the north-central plateau [*Molnar*, 1988]. There is ample evidence for a hot upper mantle beneath this area, for instances, the high Sn attenuation and the low Pn velocities from recent tomography studies [*Zhao and Xie*, 1993; *McNamara et al.*, 1997].

6.7 Dipping Velocity Interfaces and Thrust Faults

The strikes of the dipping interfaces we obtained are consistent with the EW trend of surface geology. These interfaces may be associated with thrust faults observed in the brittle upper crust of the area. For example, the shallow northwards-dipping interface

under ERDO could be related to the Fenghuoshan thrust faults which run EW in the south of the station [*Kidd et al.*, 1988]. It is estimated that a significant amount of crust shortening occurred in the Tibetan Plateau as the Indian plate collided and indented into the Eurasian plate. Palaeomagnetic data provided a rough relative movement between the two plates and showed that about 2000 km of crustal shortening has occurred between the Indo-Zangbu collision suture and Siberia [*Patriat and Achache*, 1984; *Lin and Watts*, 1988]. Accommodating such a large amount of crustal shortening requires folding and thrust faulting within the plateau or along its north and south boundaries. Large-scale thrust faults exist along the Himalayan front and at the northwest boundary between the Tibetan Plateau and Tarim Basin. Recent geological expeditions also found evidence of thrust faults in northern Tibet [*Molnar et al.*, 1987; *Tapponnier et al.*, 1990].

6.8 Conclusions

In summary, the waveform variation of receiver functions with back-azimuth at three stations located in the northern Tibetan Plateau shows that there are strong lateral heterogeneities within the upper-middle crust in this region. The waveform variation pattern also indicates that they are mainly produced by EW striking dipping interfaces. The strike direction is consistent with the EW trend of surface geology. Modeling a negative-polarity P-to-S converted phase in the receiver functions at each station shows that there is a mid-crustal low velocity layer with the upper boundary dipping 20-30° to the south. The low velocity layer, together with other geological and seismological observations, suggests that there is a hot, possibly partial melt zone in the middle crust of northern Tibet. Alternatively, dipping velocity interfaces might be associated with some buried thrust faults in the upper crust which accommodated crustal shortening during the plateau formation.

Shallow and mid-crustal dipping interfaces have noticeable impact on the modeling of deep structure such as the Moho. As demonstrated in our theoretical receiver functions in Figure 6.1, the multiple converted phases of the dipping interface interfere

with the Moho Ps and the amplitude of Moho Ps varies with back-azimuth. For a crustal thickness of about 65 km, the predicted arrival time of Moho Ps is 7.5-8 s after the direct P arrival. However, at all three stations, we have not consistently observed Moho Ps on the receiver function profiles (Figure 6.3). As the receiver function method is being widely used for both permanent and portable stations, more attention should be given to these heterogeneity effects on the waveform modeling.

Chapter 7
Significant Moho Relief Across the Northern Margin of the Tibetan Plateau

7.1 Abstract

Teleseismic P waveforms recorded during the recent Sino-US and Sino-French seismic experiments on the Tibetan Plateau are analyzed to study the plateau's lithospheric structure. Anomalous "double-pulse" waveforms are systematically observed at one station located near the northern margin of plateau. The waveform distortion is highly azimuth dependent and occurs within 20 km from the edge of the plateau. All these suggest that the "double-pulse" is produced by multi-pathing of wave propagation through rapidly varying crustal structure. Modeling the three component data with an idealized 3-D Moho topography reveals 15 to 20 km Moho offset occurring in less than 5 km laterally beneath the station. This EW-striking offset apparently separates the thickened crust of the Tibetan Plateau from that of the Qaidam Basin to the north. Such a sharp and large Moho relief beneath the margin of the plateau provides important constraints on dynamic models of continental collision and plateau uplift.

7.2 Introduction

The Tibetan Plateau, the world's highest and largest elevated landmass, has been a longstanding and challenging subject of Earth science. Recently, a series of seismic experiments were conducted on the plateau which have provided an enriched data set for studying the plateau's lithospheric structure [*Owens et al.*, 1993; *Zhao et al.*,

1993; *Hirn et al.*, 1995; *Wittlinger et al.*, 1996; *Nelson et al.*, 1996]. Although it is now widely accepted that the uplift of the plateau is the result of its thickened crust in response to the India-Asia continental collision, the mechanism of thickening crust by collision is still under debate. Different models have been proposed, including underthrusting Indian crust under Asian crust [*Argand*, 1924; *Bird*, 1978; *Powell and Conaghan*, 1973, 1975; *Barazangi and Ni*, 1982], ejecting Indian crustal material into the Tibetan crust [*Zhao and Morgan*, 1985, 1987; *Westaway*, 1993], or shortening the Asian crust [*Dewey and Bird*, 1970; *Dewey and Burke*, 1973; *England and McKenzie*, 1982; *England and Houseman*, 1986; *Dewey et al.*, 1988]. A thorough understanding of the plateau's lithospheric structure can help to differentiate between these mechanisms.

The present plateau has a fairly uniform elevation of about 5 km surrounded by several low-altitude sedimentary basins: the Tarim Basin to the northwest, Qaidam Basin to the north, and Sichuan Basin to the east (Figure 7.1A). These basins are underlain by stable Precambrian cratons that have experienced no significant deformation since Paleozoic [*Dewey et al.*, 1988; *Marauyama et al.*, 1989; *Yin and Nie*, 1996]. Little is known about the lithospheric structures lying between the plateau and these cratons. Here we present an analysis of teleseismic P waveforms obtained during the 1991-1992 Sino-US and 1993 Sino-French seismological experiments. In particular, we show anomalous waveform shapes at one station located near the northern margin of plateau. Our waveform modeling indicates that there is a 15 to 20 km offset of the Moho over a lateral distance of less than 5 km under this station. This EW-striking offset apparently separates the thickened plateau crust from the Qaidam Basin crust. To our knowledge, such a large Moho relief has not been reported elsewhere.

7.3 Data and Results

During the 1991-1992 Sino-US Tibet seismic experiment, 11 broadband stations were deployed along and east of the Golmud-Lhasa highway [*Owens et al.*, 1993] (Figure 7.1A). More than 200 teleseismic events (distance range larger than 30°) were

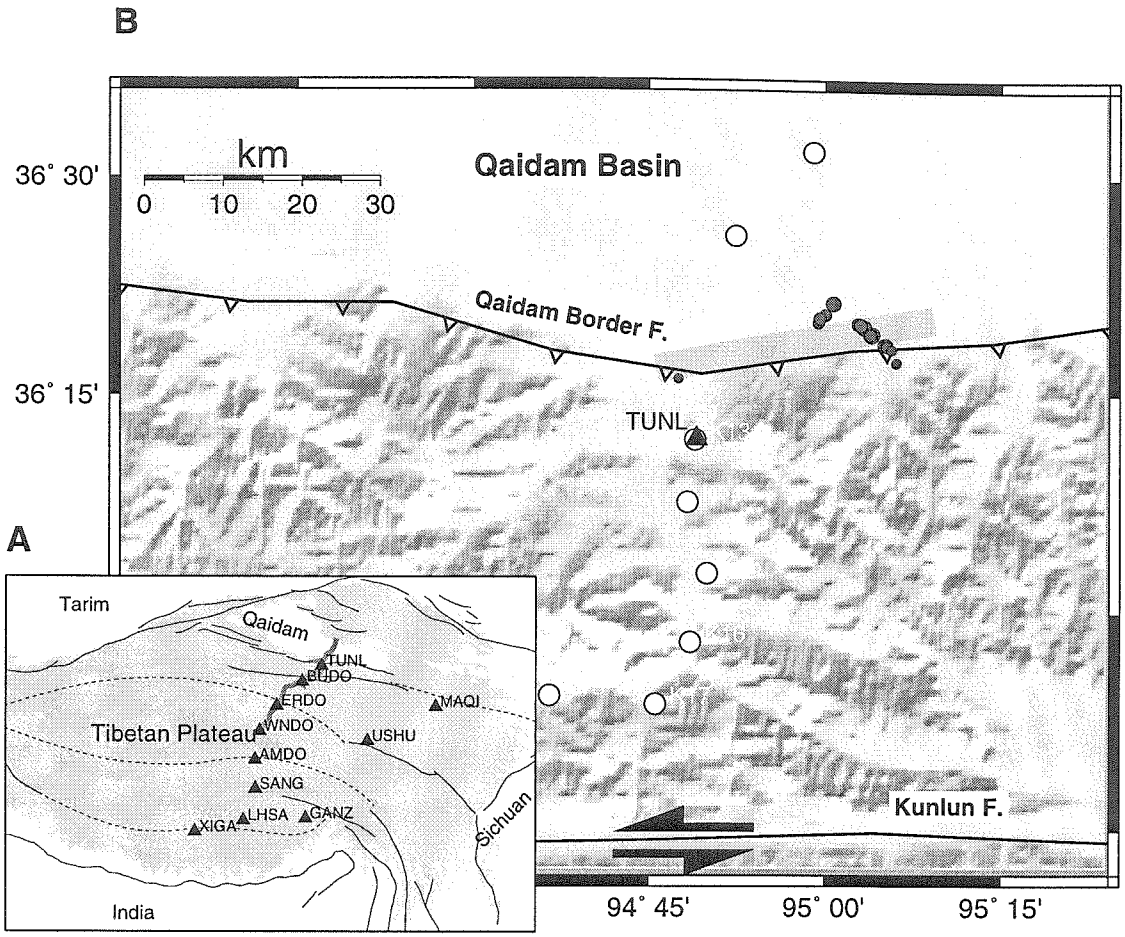

Figure 7.1: (A) Tectonic map of the Tibetan Plateau and surrounding areas. Shading indicates elevation above 3 km. Solid lines are major faults and dashed lines are sutures. Triangles are stations of the 1991-1992 Sino-US Tibet seismic experiment. The thickened gray line is the 1993 Sino-French profile of 50 short-period instruments. (B) A zoom-in of the northern Tibetan margin near station TUNL (triangle) which shows anomalous "double-pulse" P waveforms for events from certain azimuths (shown as gray dots, they are the projections of these events on to the horizontal plane 50 km below the station). Also shown in the figure are stations of the 1993 experiment (open circles). The absence of anomalous waveforms at stations K10 and K14 indicates that the velocity anomaly causing the distorted waveforms is less than 60 km deep and therefore can be best explained by a Moho offset (see text). The map view of the offset is represented by the thickened gray line.

recorded with good signal/noise ratios. For each event, we align the records of all stations with the onsets of the P wave to examine the waveform variation across the array. Generally, the vertical component of the teleseismic P wave is less sensitive to structure near the recording site, because of the wave's near vertical incidence. For this reason, it is often treated as an effective source time function of the earthquake in receiver function analyses [*Langston*, 1977]. However, if strong heterogeneity exists, a certain amount of waveform distortion can be expected. We notice that the vertical P waveforms at one station, TUNL, consistently show "double-pulse" arrivals for events from directions N45°E to N70°E. This station is located in the foothills of the Kunlun mountain range, which runs EW and marks the northern boundary of the Tibetan Plateau (Figure 7.1). Figure 7.2A shows a typical example. The waveforms are unfiltered vertical component of velocity records from an event occurring beneath Kuril Island (12/13/1991 08:00UTC, M_b 5.5 and depth at 49 km, from the International Seismological Centre Bulletin). Although the amplitudes vary from station to station, the P waveforms at most stations have a similar single-pulse shape, which is expected for these epicentral distances from an event at this depth. However, the waveform at TUNL consists of two pulses separated by about 1 s. Because the similarity of waveforms at other stations rules out the possibility of a complex event source time function, we conclude that the double pulses are caused by multi-pathing of wave propagation through some strong laterally varying receiver-side velocity structure.

We can estimate the depth, z, of the anomalous structure by examining the size of the Fresnel Zone, R, at the surface. From classic optics theory,

$$R = \sqrt{\lambda z}, \tag{7.1}$$

where λ is the wavelength which is about 10 km for teleseismic P waves. Unfortunately, the station spacing of the Sino-US experiment is larger than 100 km, so it can not further constrain the area where the "double pulse" waveform can be observed. However, in 1993 another seismic experiment was conducted by Chinese and French scientists in which 50 stations were deployed along a NS profile from the Qaidam

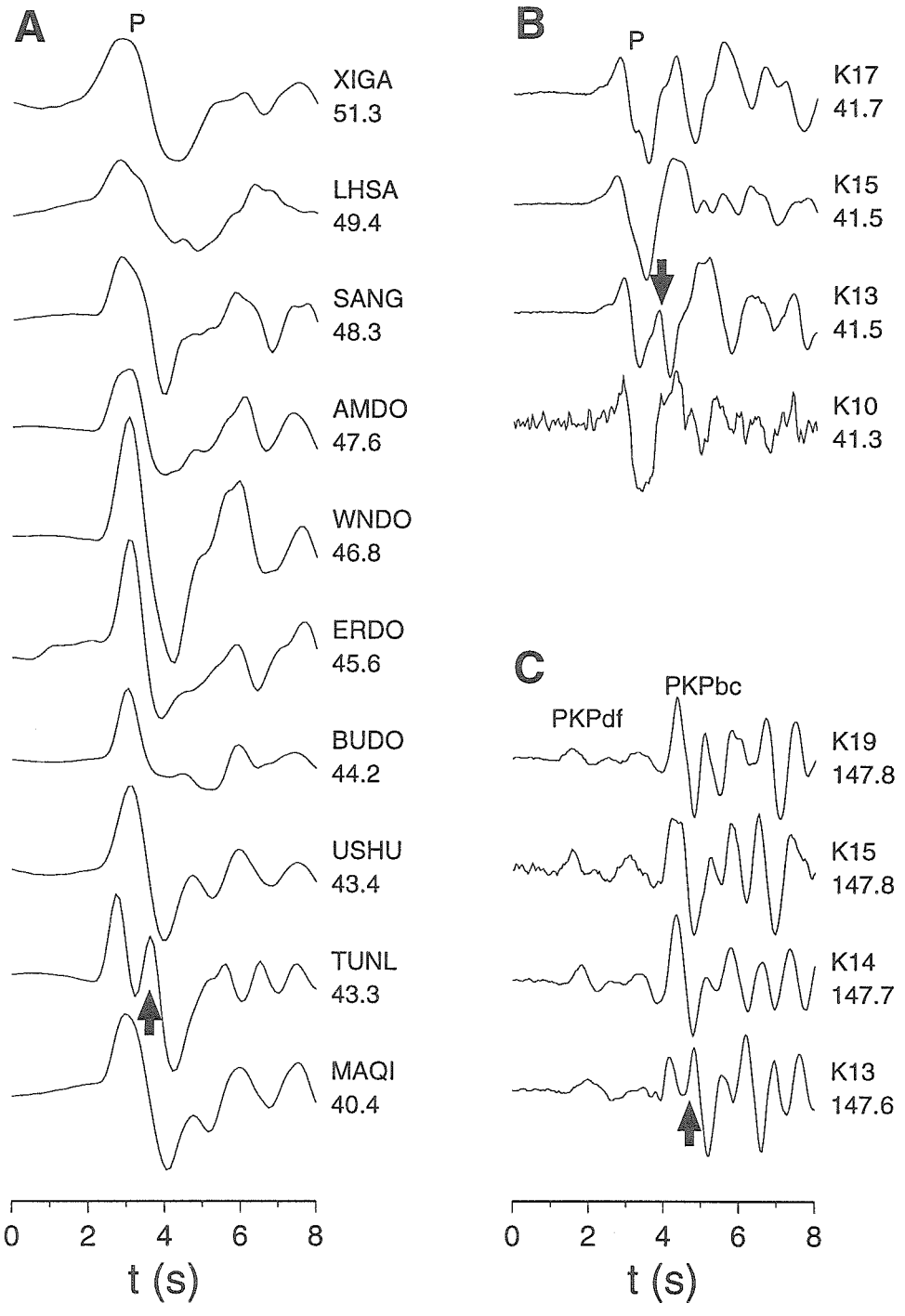

Figure 7.2: Vertical components of velocity records of three teleseismic events. A and B are from two events near the Kuril Island (azimuth 60° with respect to station TUNL/K13) and C is from a more distant event (azimuth 343°). In B and C normalized amplitudes are plotted because the station gain factors of the Sino-French experiment are not available, but in A relative amplitudes are plotted; The numbers under station names are epicentral distances in degrees. Arrows point to the anomalous "double-pulse" P waveform shape at station TUNL/K13.

Basin to central Tibet [*Wittlinger et al.*, 1996]. The experiment only lasted for three months and used mostly short-period instruments, so the number of useful records is limited. Despite these drawbacks the experiment did provide very good spatial coverage. As seen in Figure 7.1B, station K13 in this experiment was located at the same site as TUNL. The same "double-pulse" waveforms were observed at this station for events from a similar azimuth range. However, the nearby stations, K10, K14, K15, and K17, do not show the distortion (Figure 7.2BC). This helps us to narrow down the size of the Fresnel Zone to be less than 25 km (half of the distance between K10 and K14), which yields a depth estimate of the velocity anomaly to be less than 60 km.

Assigning the velocity anomaly to the crust would require an unrealistic lateral velocity variation of larger than 10%. On the other hand, because of the large velocity contrast across the crust-mantle boundary, an offset of the Moho can easily provide the desired lateral velocity variation (Figure 7.3). We use forward modeling to determine the location, orientation, height and width of the offset (Figure 7.4). Our calculation indicates that the occurrence of the second pulse and its relative amplitude are very sensitive to the azimuths of incoming rays and to the width of the offset. This strong dependence leads to very good constraints on the strike (N80°E) and the width (less than 5 km) of the offset. The height of the offset is mostly determined by the separation of the two pulses and thus trades off with the velocity contrast at the Moho and in the crust. Assuming the same crustal P velocity of 6.3 km/s for both the Tibetan Plateau and Qaidam Basin yields a 20 km offset. If we increase the P velocity of the lower crust of Qaidam to 6.7 km/s, a 15 km Moho offset is still required. The predicted P waveform from the Moho offset model fits the three components of observed waveforms quite well (Figure 7.4C).

There are several other pieces of evidence supporting a Moho offset between the Tibetan Plateau and the Qaidam Basin. First, the teleseismic P waves from events at the northern azimuths arrive about 1 to 2 s earlier at TUNL compared with those events from the southern azimuths (Figure 5.5). Secondly, the receiver function profile for the SE direction indicates that the crust is about 55 km thick south of the station

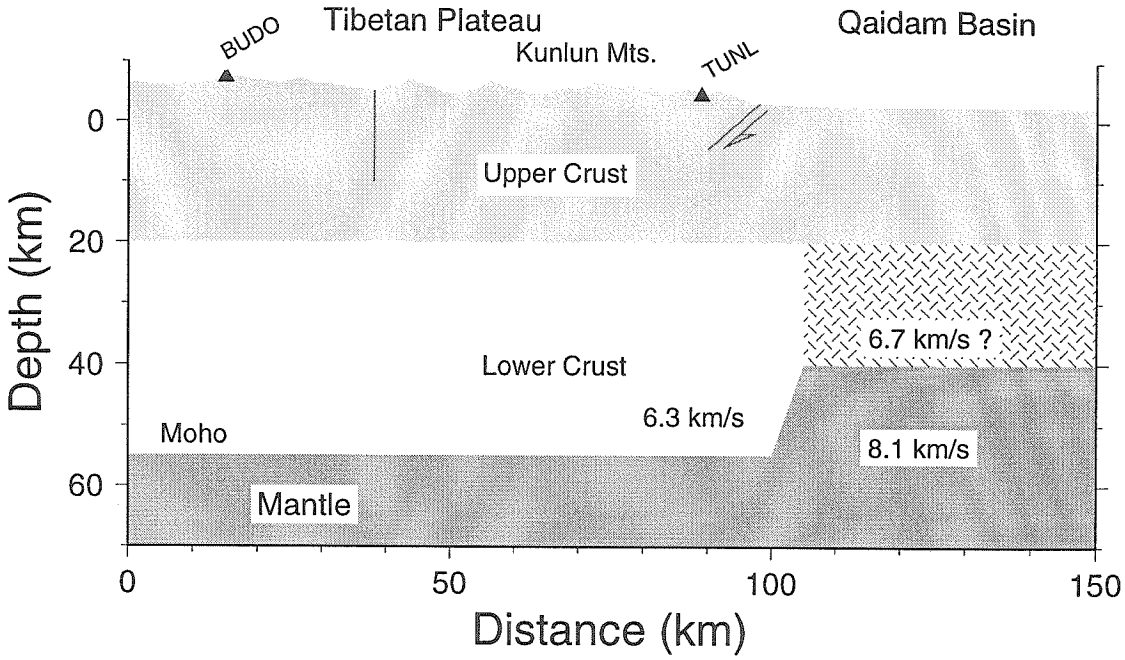

Figure 7.3: A NS cross section along the 95°E line of longitude showing the surface topography (exaggerated by factor of 2), major faults, and possible crustal structure used in modeling the waveform at TUNL. The division of the crust into the upper and lower parts at a depth of 20 km is approximate, but there is ample evidence indicating the existence of a low velocity lower crust in northern Tibet [*Ni and Barazangi*, 1983; *Brandon and Romanowicz*, 1986; *Molnar et al.*, 1987; *Zhu et al.*, 1993, 1995; *McNamara et al.*, 1995; *Owens and Zandt*, 1997]. The lateral velocity contrast caused by the Moho offset is responsible for causing multi-pathing propagation of incident teleseismic P waves and producing the "double-pulse" P waveform at station TUNL. The velocity difference of lower crust between the Tibetan Plateau and Qaidam Basin might also contribute to the separation of the two pulses, but can only account for a quarter of it assuming a 6.7 km/s lower crust under the Qaidam Basin.

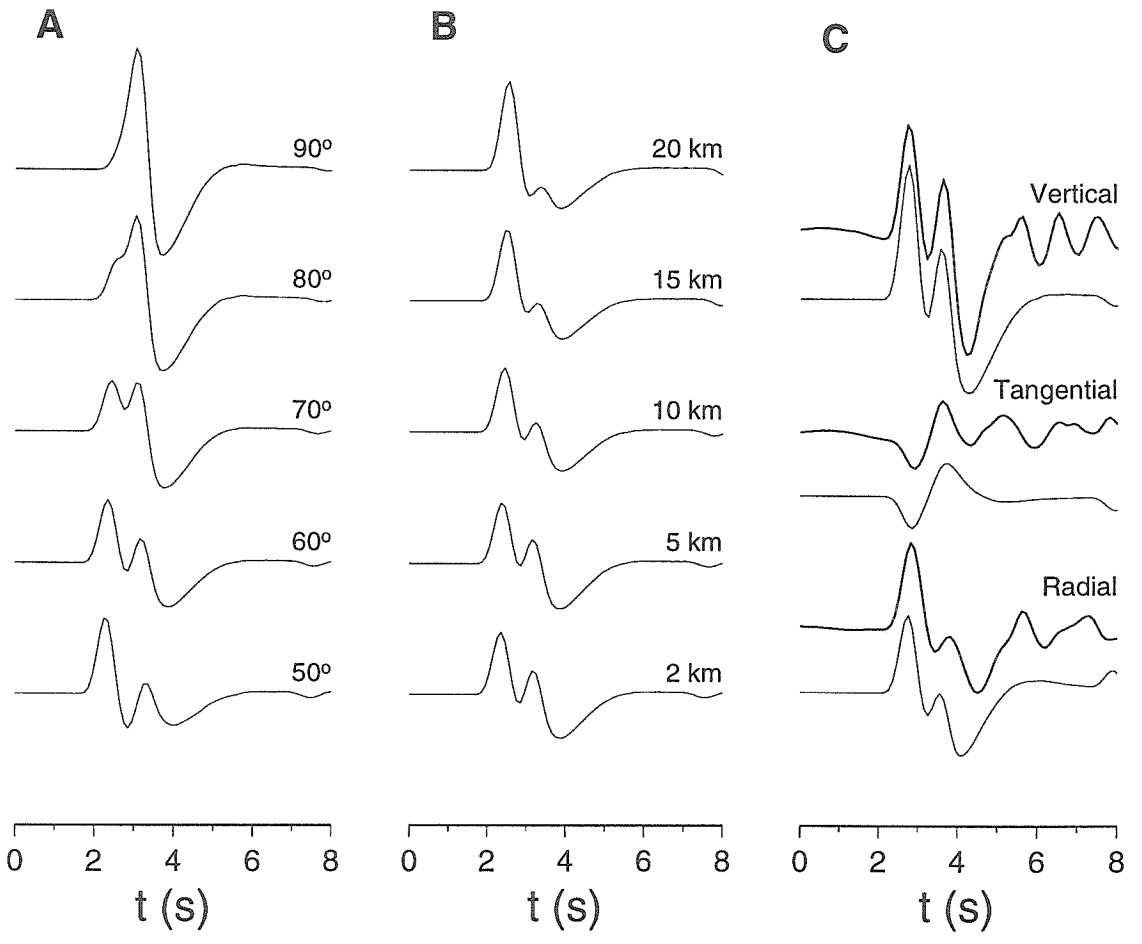

Figure 7.4: We use the Kirchhoff-Helmholtz integral to calculate the wave propagation through a 3-D Moho interface. This technique has been used to handle irregular velocity interfaces in a wide variety of geophysical problems [*Hilterman*, 1975; *Scott and Helmberger*, 1983; *Neele and Snieder*, 1992; *Vanderlee et al.*, 1994]. Our model setup and location of the receiver (TUNL) are illustrated in Figure 7.3, except that the whole crust is simplified as a layer with P velocity of 6.3 km/s. (A) Waveform variation as a function of azimuth (indicated by the number next to each trace). The strike of the offset is N80°E and its height and width are fixed as 20 km and 2 km respectively. (B) Sensitivity of waveform to the width of the offset, where the height of the offset is 20 km and the incoming teleseismic ray is from N60°E. Note that the amplitude of the second pulse decreases significantly as the offset width becomes larger than 5 km. (C) Comparison of observed three-component P waveform (heavy traces) with those predicted by our best Moho offset model: strike N80°E, width 2 km, and height 20 km.

(Figure 5.3), but no consistent Ps is observed for the NE direction, which suggests a disrupted Moho north of the station. The long-wavelength free-air gravity anomaly calculated from the global EGM96 model [*National Imagery and Mapping Agency, NASA/Goddard Space Flight Center*, 1997], while being very small over most part of the plateau, shows an oscillatory across the northern boundary (Figure 5.9). A similar change of the gravity anomaly occurs across the Himalayas where the crustal thickness decreases from 80 km in the plateau to 35 km in India.

7.4 Discussion

Although it has been known for some time that the Tibetan Plateau has an abnormally thick crust, the rapid transition of crustal thickness from the plateau to surrounding regions, as revealed by the Moho offset, is of considerable interest and may provide important information about the crustal deformation and rheology. The offset is located directly underneath the northern boundary of the plateau where the surface elevation increases abruptly from 3 km to more than 5 km. Such a good correlation between the surface topography and the Moho depth indicates that the plateau is supported by its thick low-density crust. On the other hand, the Moho offset apparently has no connection to the faults on the surface (Figure 7.3), which implies that the deformation in the upper and lower crust is decoupled. Increasing numbers of seismological observations have shown the existence of partial melt within the lower crust in central and northern Tibet [*Ni and Barazangi*, 1983; *Brandon and Romanowicz*, 1986; *Molnar et al.*, 1987; *Zhu et al.*, 1993, 1995; *McNamara et al.*, 1995; *Owens and Zandt*, 1997]. As a consequence, the deformations of the lower crust are most likely in the form of ductile flow. In contrast, the Qaidam Basin block, a Precambrian craton which was accreted to Eurasia in Paleozoic [*Dewey et al.*, 1988; *Yin and Nie*, 1996], is probably colder and stronger than the Tibetan crust. As the Indian plate moves northward, the Qaidam lower crust acts as a rigid block to resist the flow of Tibetan lower crustal material [*Zhao and Morgan*, 1985; *Westaway*, 1993]. Similar blockages by other Precambrian cratons surrounding the plateau may play

an important role in the evolution of the plateau by confining the deformation of Tibetan crust to a limited volume.

The existence of an abrupt change of Moho topography also raises concern about 3-D seismic tomography studies which usually assume a flat Moho as their starting model and invert travel time residuals for velocity perturbations in the crust and mantle. Our waveform analysis shows that a large portion of the travel time residuals is produced by the Moho offset, and if ignored, this structure could be easily mapped into the upper mantle velocity variation because of the embedded poor vertical resolution in teleseismic travel time inversions. Whereas the "double-pulse" waveforms at station TUNL represent an extreme case of distortion by abrupt structural variation, smoothly varying Moho topography will modulate waveforms in a more subtle way, either sharpening or broadening the P waveform pulse, as seen at other stations in Figure 7.2A. With the ever increasing deployments of broadband arrays in tectonically interesting regions, the use of waveform data in addition to travel time measurements can not be overemphasized.

Appendix A
Kirchhoff Diffraction Theory and the Application to Modeling Moho Topography

A.1 Kirchhoff Diffraction Theory

Green's Theorem states that

$$\iiint_V (\phi\nabla^2\psi - \psi\nabla^2\phi)\, dV = \iint_S (\phi\frac{\partial\psi}{\partial n} - \psi\frac{\partial\phi}{\partial n})\, dS, \tag{A.1}$$

where S is the surface surrounding a volume V with the norm direction outward (Figure A.1).

If both ϕ, ψ satisfy the wave equation in V

$$\begin{aligned} \nabla^2\phi &= \frac{1}{c^2}\frac{\partial^2\phi}{\partial^2 t}, \\ \nabla^2\psi &= \frac{1}{c^2}\frac{\partial^2\psi}{\partial^2 t}, \end{aligned}$$

and furthermore if the medium in V is homogeneous, a well-known solution is

$$\psi(\mathbf{x}, t; \xi, \tau) = \frac{\delta(t-\tau)}{4\pi|\mathbf{x}-\xi|},$$

substituting them in (1) gives Kirchhoff's formulae

$$\phi(\mathbf{x}, t) = \frac{1}{4\pi}\iint_S \left\{\frac{1}{r}\frac{\partial\phi}{\partial n} - \frac{\partial\frac{1}{r}}{\partial n}\phi + \frac{1}{cr}\frac{\partial r}{\partial n}\frac{\partial\phi}{\partial t}\right\} dS, \tag{A.2}$$

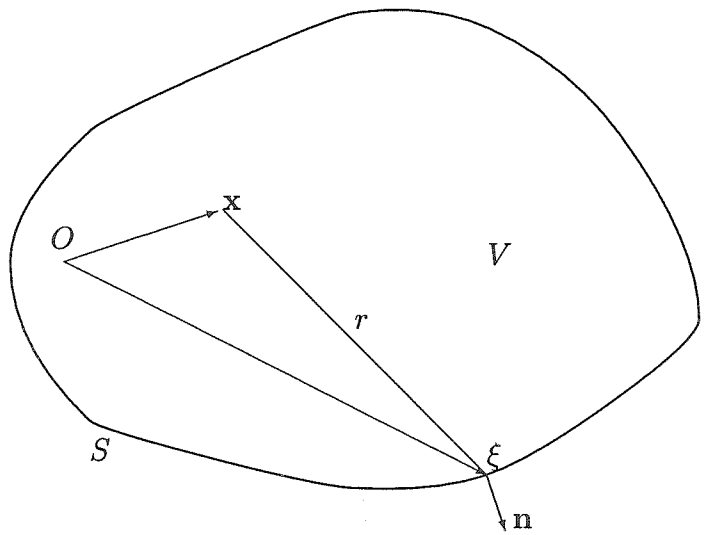

Figure A.1: Representing potential at any point $\mathbf{x}$ inside V with the potential on boundary S.

where $r = |\mathbf{x} - \xi|$ and all terms are evaluated at retarded time $t - r/c$. Equation (A.2) means that once we know values of ϕ and $\frac{\partial \phi}{\partial n}$ on S we can determine the wavefield at any point in V.

A.2 Effect of Moho Topography on Teleseismic Waveform

For a teleseismic wave impinging on the crust, the incident wavefield can be approximated as a plane wave

$$\phi_0(\mathbf{x}, t) = f(t - \mathbf{p}_0 \cdot \mathbf{x}),$$

where $\mathbf{p}_0$ is the incident wave vector. Using the transmission coefficient, the potential on the Moho (crustal side) is

$$\phi(\xi, t) = T f(t - \mathbf{p}_0 \cdot \xi).$$

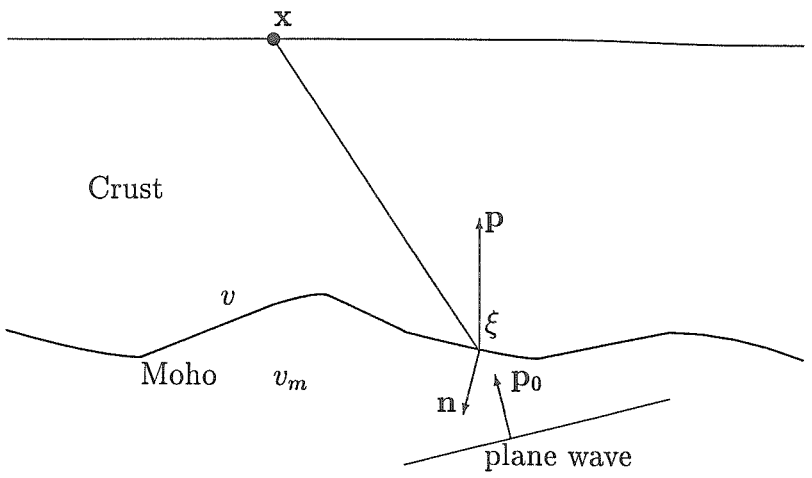

Figure A.2: Modeling Moho topography using teleseismic waveform.

The evaluation of $\frac{\partial \phi}{\partial n}$ on the Moho needs a little more caution. Locally, the transmitted wave near the Moho can also be approximated as a plane wave too

$$\phi(\mathbf{x}, t) = g(t - \mathbf{p} \cdot \mathbf{x}),$$

here $\mathbf{p}$ is the wave vector of the transmitted wave which can be obtained using Snell's law:

$$\mathbf{p} = \mathbf{p}_0 - \left(\mathbf{p}_0 \cdot \mathbf{n} + \sqrt{(\frac{1}{v})^2 - (\frac{1}{v_m})^2 + (\mathbf{p}_0 \cdot \mathbf{n})^2} \right) \mathbf{n}.$$

From the expression of $\phi(\mathbf{x}, t)$, one has

$$\frac{\partial \phi(\mathbf{x}, t)}{\partial x_i} = -g'(t - \mathbf{p} \cdot \mathbf{x})\, p_j \frac{\partial x_j}{\partial x_i} = -g'(t - \mathbf{p} \cdot \mathbf{x})\, p_i.$$

So

$$\left. \frac{\partial \phi}{\partial n} \right|_{\mathbf{x}=\xi} = -g'(t - \mathbf{p} \cdot \xi)\, \mathbf{p} = -T\, f'(t - \mathbf{p}_0 \cdot \xi)\, \mathbf{p}.$$

Substituting them into (A.2) we get the potential at the receiver

$$\phi(\mathbf{x},t) = \frac{1}{4\pi}\iint\limits_{Moho} T\left\{\frac{\gamma_i n_i}{r^2}f(t-\tau) + \frac{n_i}{vr}(\gamma_i - vp_i)f'(t-\tau)\right\}\cdot dS, \tag{A.3}$$

where $\gamma_i = r_i/r$ and $\tau = \mathbf{p}_0\cdot\xi + r/v$.

In order to get the displacement from the potential, one can calculate the derivative ϕ with respect to $\mathbf{x}$. For P potential

$$\begin{aligned} u_i(\mathbf{x},t) &= \frac{\partial\phi(\mathbf{x},t)}{\partial x_i} \\ &= \frac{1}{4\pi}\iint\limits_{Moho} T\left\{q^1{}_i f(t-\tau) + q^2{}_i f'(t-\tau) + q^3{}_i f''(t-\tau)\right\}\, dS, \end{aligned}$$

with

$$\begin{aligned} q^1{}_i &= \frac{1}{r^3}(3\gamma_i\gamma_j - \delta_{ij})n_j, \\ q^2{}_i &= \frac{1}{vr^2}(3\gamma_i\gamma_j - \delta_{ij} - vp_j\gamma_i)n_j, \\ q^3{}_i &= \frac{1}{v^2 r}(\gamma_j - vp_j)n_j\gamma_i. \end{aligned}$$

For SV and SH potentials, it will be more complicated. An alternative is to convert the potential from each surface element into the displacement before the summation. The conversion can be done conveniently using the receiver functions given by *Helmberger* [1983]. For whole space, the receiver functions are

$$\begin{aligned} \mathbf{P} &= \mathbf{p}, \\ \mathbf{SV} &= \frac{1}{p_r}(\mathbf{p}\times\mathbf{e}_z)\times\mathbf{p}, \\ \mathbf{SH} &= \frac{p}{p_r}\mathbf{p}\times\mathbf{e}_z. \end{aligned}$$

For half space and steep incident angles, the receiver functions differ from the whole space case by a factor of 2 approximately.

Appendix B

A Modified First-motion Approximation of the Generalized Ray Theory

In the generalized ray theory (GRT), the potential from a generalized ray in a layered medium can be expressed as [*Helmberger*, 1983]

$$\phi(t) = J(t) * \frac{1}{\sqrt{t}}, \tag{B.1}$$

where

$$J(t) = Im\left\{\sqrt{p}G(p)\frac{dp}{dt}\right\}, \tag{B.2}$$

here $G(p)$ is the total reflection/transmission coefficient associated with the ray; and

$$t = px + \sum \eta h.$$

Calculating $J(t)$ numerically along the Cagniard-deHoop contour is complicated by the fact that there is a singularity at $t = t_0$ (see Figure B.1) where

$$\left.\frac{dt}{dp}\right|_{t=t_0} = 0.$$

On the other hand, the contour near p_0 has the largest contribution to the response. Therefore, very dense sampling is needed around p_0, which is computationally intense. Besides, no matter how densely the contour is sampled, the singularity often introduces large numerical inaccuracy.

A solution is to represent the singular behavior of $J(t)$ near t_0 analytically with a function $J_0(t)$ such that we can evaluate a regular function $J(t) - J_0(t)$ along the

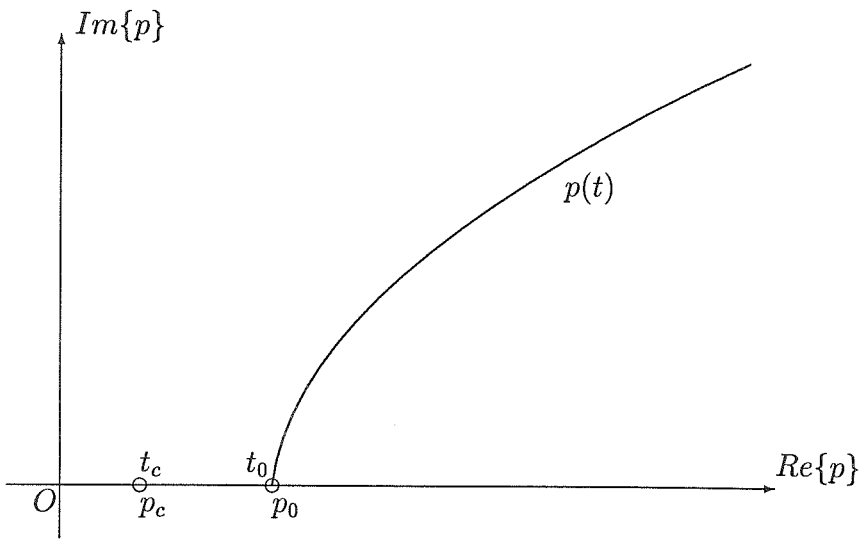

Figure B.1: Cagniard-deHoop contour. $p = p_0$ corresponds to $t = t_0$ of the geometrical ray arrival time.

contour without worrying about the singularity at t_0. The full response is obtained by adding the contribution from $J_0(t)$ later (which we call it the first-motion response).

Using the Taylor expansion, $\frac{dp}{dt}$ near t_0 is approximated as

$$\frac{dp}{dt} = \frac{i\sqrt{\frac{1}{2}\left|\frac{d^2p}{dt^2}\right|_{p=p_0}}}{\sqrt{t-t_0}},$$

so

$$J_0(t) = \begin{cases} \frac{Re\{C\}}{\sqrt{t-t_0}} & t > t_0 \\ \frac{Im\{C\}}{\sqrt{t_0-t}} & t < t_0 \end{cases}, \tag{B.3}$$

where

$$C = \frac{\sqrt{p}G(p)}{\sqrt{2\left|\frac{d^2p}{dt^2}\right|_{p=p_0}}}.$$

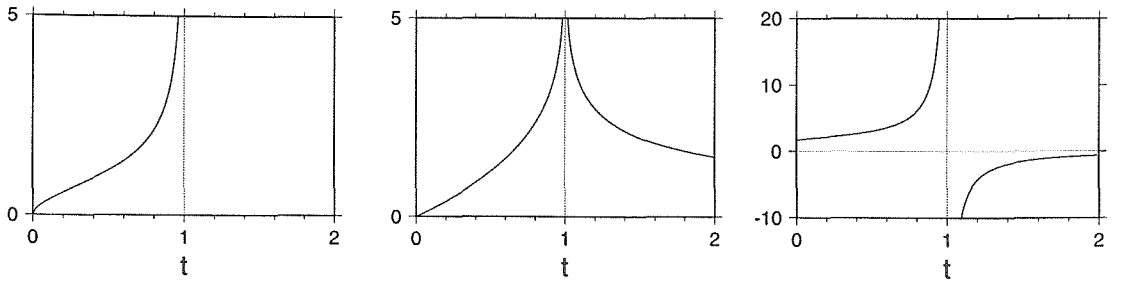

(a) $J_0(t)$ (b) $\phi_0(t) = J_0(t) * \frac{1}{\sqrt{t}}$ (c) $\phi_0'(t)$

Figure B.2: Behaviors of different function $J_0(t)$, $\phi_0(t)$, and $\phi_0'(t)$ near $t = t_0$. Normalized time is used.

For pre-critical angle reflection ($p_c > p_0$), C is real. The response

$$\phi_0(t) = C\frac{H(t-t_0)}{\sqrt{t-t_0}} * \frac{1}{\sqrt{t}} = \pi C H(t-t_0).$$

For post-critical angle reflection (i.e., $p_c < p_0$), one needs to take into account the contribution of $J_0(t)$ between $t_c \leq t \leq t_0$ where t_c corresponds to the head wave arrival time. *Mellman and Helmberger* [1978] gave an approximation of $J(t)$ near t_c.

$$J(t) \sim \sqrt{t-t_c}.$$

By combining the behaviors of $J(t)$ at t_c and t_0 together, we define the first-motion approximation of $J(t)$ between t_c and t_0 as

$$J_0(t) = Im\{C(p_0)\}\left(\frac{1}{\sqrt{t_0-t}} + \frac{\sqrt{t-t_c}}{t_0-t_c} - \frac{1}{\sqrt{t_0-t_c}}\right),$$

or

$$J_0(t) = \frac{1}{\sqrt{1-\tau}} + \sqrt{\tau} - 1, \tag{B.4}$$

using the normalized time $\tau = \frac{t-t_c}{t_0-t_c}$ and omitting the constant $\frac{Im\{C(p_0)\}}{\sqrt{t_0-t_c}}$. It is shown in Figure B.2.

The first-motion approximation response from $J_0(t)$ is

$$\begin{aligned}
\phi_0(t) &= J_0(t) * \frac{1}{\sqrt{t}} \\
&= \int_0^{min(1,t)} \left(\frac{1}{\sqrt{1-u}} + \sqrt{u} - 1 \right) \frac{du}{\sqrt{u-t}} \\
&= \ln \left| \frac{\sqrt{t}+1}{\sqrt{t}-1} \right| + \int_0^{min(1,t)} \frac{\sqrt{u}-1}{\sqrt{t-u}} du \\
&= \ln \left| \frac{\sqrt{t}+1}{\sqrt{t}-1} \right| - \left(\sqrt{u(t-u)} + t \cos^{-1} \sqrt{\frac{u}{t}} - 2\sqrt{t-u} \right) \Bigg|_{u=0}^{u=min(1,t)} \\
&= \ln \left| \frac{\sqrt{t}+1}{\sqrt{t}-1} \right| + \frac{\pi}{2} t - 2\sqrt{t} + \left(\sqrt{t-1} - t \tan^{-1} \sqrt{t-1} \right) H(t-1).
\end{aligned}$$

We can see that $\phi_0(t)$ has a logarithm singularity at t_0.

Most of time, we need to calculate the derivative of the potential response which is

$$\phi_0'(t) = \frac{\sqrt{t}}{1-t} + \frac{\pi}{2} - \tan^{-1} \sqrt{t-1} H(t-1). \tag{B.5}$$

Because of the singularity at t_0, when evaluating $\phi_0(t)$ with a sampling interval of Δ, it is better to sample

$$\begin{aligned}
g_0(t) &= J_0(t) * \sqrt{t} \\
&= \sqrt{t} - \frac{2}{3} t^{3/2} + \frac{\pi}{8} t^2 + \frac{t-1}{2} \ln \left| \frac{\sqrt{t}+1}{\sqrt{t}-1} \right| \\
&\quad + \left(\frac{\sqrt{t-1}}{4} + \frac{5}{12} (t-1)^{3/2} + \frac{t^2}{8} \left[\tan^{-1} \frac{2-t}{2\sqrt{t-1}} - \frac{\pi}{2} \right] \right) H(t-1),
\end{aligned}$$

and then use the relation

$$\phi_0'(t) = 2 g_0''(t)$$

to obtain $\phi_0'(i\Delta)$ using the second-order finite-difference.

Appendix C

Sampling Function

There are many situations in seismology where one needs to discrete a function that has certain kind of discontinuity. Some examples are Dirac $\delta(t-\tau)$, Heviside $H(t-\tau)$, and Ramp $R(t-\tau)$. In order to properly represent these functions with a discrete series of sampling interval Δ, some precautions need to be taken around the discontinuity $t = \tau$. One solution is to convolve the function with a sampling function to reduce the order of discontinuity.

An often used sampling function is the triangle function

$$s(t) = \begin{cases} \frac{1}{\Delta}(1 - \frac{|t|}{\Delta}) & \text{if } |t| < \Delta \\ 0 & \text{otherwise.} \end{cases}$$

The values for points left and right of discontinuity $t = \tau$ for above discontinuous functions using the triangle sampling function are given in Table C.1.

Table C.1: Sampling discontinuous functions with the triangle sampling function

function	left	right
$\delta(t-\tau)\Delta$	x	x
$H(t-\tau)$	$0.5x^2$	$1-0.5x^2$
$R(t-\tau)/\Delta$	$\frac{1}{6}x^3$	$1-x+\frac{1}{6}x^3$

x: distance between τ and the other point normalized by Δ.

Appendix D

Source Mechanisms and Depths of Southern California Earthquakes

Table D.1: Source mechanisms and depths of southern California earthquakes from the waveform inversion

SCSN Location and Origin Time						Inversion Result		
Date	o, GMT	Lat./Long.	h	M_l	Q	$\phi/\delta/\lambda$	M_w	h
90/10/18	17:21:56.1	33.64/-117.88	3.2	3.8	A	100/10/000	3.7	8
90/12/17	17:44:21.2	34.21/-117.02	6.0	3.7	A	160/30/-90	3.5	5
91/05/04	18:28:18.8	37.54/-118.43	6.0	4.0	B	210/60/010	3.6	5
91/05/20	15:00:53.4	33.78/-116.93	12.8	3.7	A	140/70/-90	3.6	11
91/06/28	14:43:54.5	34.26/-118.00	10.5	5.4	A	240/50/070	5.5	11
91/06/28	17:00:55.6	34.25/-117.99	9.5	4.3	A	240/50/040	4.1	11
91/06/29	17:53:52.0	34.91/-116.58	6.0	4.0	A	070/90/-40	3.7	8
91/07/03	09:14:04.8	37.62/-118.92	6.0	4.0	A	120/50/-60	3.6	5
91/07/05	17:41:57.1	34.50/-118.56	10.9	4.1	A	110/50/080	3.8	14
91/07/19	02:41:36.8	33.21/-115.97	3.1	4.0	A	070/40/060	3.8	8
91/08/11	06:09:53.5	37.63/-118.84	6.0	4.1	A	330/60/-50	3.7	8
91/10/12	14:39:32.1	33.89/-116.16	2.9	4.0	A	070/60/-20	3.8	5
91/12/04	07:10:57.6	33.07/-116.80	14.9	4.2	A	240/70/030	3.8	17
91/12/04	08:17:03.5	34.18/-117.02	10.7	4.0	A	230/80/-20	3.7	17
91/12/20	10:38:29.4	35.53/-117.37	7.9	4.1	A	080/80/-20	4.0	14
92/02/19	11:19:24.9	36.03/-117.89	2.9	4.0	A	260/80/020	3.9	5

continued on next page

continued from previous page

92/02/22	03:32:20.6	36.03/-117.90	0.9	3.6	A	270/80/010	3.5	5
92/03/03	08:07:49.5	35.76/-118.03	4.0	3.7	A	030/60/-50	3.7	8
92/03/04	19:06:27.0	32.97/-118.79	6.0	4.2	B	020/50/090	4.1	17
92/03/05	18:24:22.8	35.22/-119.37	23.8	3.8	A	100/40/080	3.5	8
92/03/16	19:20:22.3	36.00/-117.88	1.1	3.6	A	040/30/-60	3.6	8
92/03/17	11:56:35.9	36.01/-117.88	2.6	3.9	A	060/60/-10	3.7	8
92/04/10	20:13:23.0	33.38/-116.30	12.1	3.5	A	070/60/070	3.6	11
92/04/15	19:05:47.2	34.29/-117.56	3.3	3.5	A	200/60/-20	3.4	8
92/04/23	02:25:29.9	33.96/-116.32	11.5	4.6	A	260/80/010	4.2	17
92/04/24	03:29:59.6	34.03/-116.33	0.2	3.6	A	240/50/-30	3.5	5
92/05/02	12:46:41.4	33.99/-116.29	4.0	4.1	A	070/70/000	3.8	8
92/05/02	19:10:23.7	33.99/-116.29	3.7	3.6	A	060/70/-30	3.5	8
92/05/04	01:16:02.6	33.94/-116.34	5.8	4.2	A	240/40/010	4.0	8
92/05/04	16:19:49.7	33.94/-116.30	12.4	4.8	A	080/80/-30	4.7	20
92/05/06	02:38:43.3	33.94/-116.31	6.8	4.7	A	010/80/-80	4.5	17
92/05/06	05:10:43.9	33.94/-116.32	6.4	3.6	A	250/30/010	3.3	8
92/05/06	17:41:19.2	33.95/-116.32	5.1	3.6	A	190/60/-60	3.4	11
92/05/12	02:31:27.9	33.98/-116.26	0.2	4.4	A	060/80/-30	4.2	8
92/05/18	00:22:34.2	33.95/-116.36	7.7	3.7	A	250/70/-30	3.6	14
92/05/18	15:44:18.0	33.95/-116.34	6.6	5.0	A	240/50/-20	4.6	14
92/05/19	12:15:27.6	33.94/-116.34	4.8	3.5	A	210/50/-50	3.0	8
92/05/24	12:22:25.8	32.82/-116.17	11.9	4.0	A	250/80/-20	3.6	8
92/05/31	11:38:45.3	34.58/-116.84	2.5	3.6	A	270/60/020	3.5	8
92/06/11	00:24:19.2	34.17/-116.35	0.8	4.4	A	090/70/010	4.1	8
92/06/24	08:04:44.6	34.41/-116.81	1.1	3.6	A	060/60/020	3.6	8
92/06/28	05:54:41.1	34.20/-116.44	0.2	3.6	A	080/60/000	3.7	8
92/06/28	12:36:40.6	34.13/-116.43	7.4	5.3	C	050/60/-60	5.2	14

continued on next page

continued from previous page

92/06/28	14:43:21.9	34.16/-116.85	11.1	5.5	B	230/40/030	5.2	17
92/06/28	15:24:29.4	34.21/-116.76	6.0	4.7	A	040/60/-30	4.8	8
92/06/28	17:01:31.9	34.18/-116.92	13.7	5.1	A	240/30/050	4.6	14
92/06/28	17:39:51.9	34.38/-116.47	6.0	4.0	A	310/60/030	3.8	8
92/06/28	17:48:32.4	34.22/-116.75	1.2	4.4	A	230/50/000	4.3	8
92/06/28	19:42:14.5	34.19/-116.44	2.3	3.7	A	220/20/-20	3.6	8
92/06/28	20:23:18.4	34.12/-116.43	2.3	3.6	A	340/10/000	3.2	5
92/06/28	21:13:16.5	34.10/-116.43	3.8	4.6	A	110/50/090	4.3	8
92/06/28	22:13:12.0	34.06/-116.36	7.0	4.0	B	230/60/020	3.8	11
92/06/29	04:16:42.6	35.02/-117.20	3.5	4.1	A	020/90/080	3.9	8
92/06/29	04:41:54.8	34.13/-116.40	3.0	3.7	A	310/50/040	3.5	14
92/06/29	05:36:44.5	34.60/-116.64	6.0	3.7	A	010/70/000	3.5	5
92/06/29	14:31:30.4	34.08/-116.39	4.9	4.6	A	040/50/-70	4.3	11
92/06/29	14:41:26.0	34.12/-117.00	4.7	4.6	A	210/60/010	4.6	8
92/06/29	14:54:06.9	34.10/-116.42	3.7	4.2	A	050/70/-40	3.7	8
92/06/29	16:41:41.9	34.25/-116.72	1.6	4.5	A	070/50/010	4.6	8
92/06/29	20:07:35.4	33.89/-116.29	2.5	4.1	A	060/80/-20	3.7	5
92/06/29	22:52:16.1	34.16/-118.17	3.2	3.9	A	080/80/020	3.6	5
92/06/30	05:33:48.0	34.22/-116.75	1.6	3.9	A	230/70/010	3.7	5
92/06/30	07:36:28.2	34.16/-116.43	0.5	3.7	A	110/80/-20	3.3	5
92/06/30	08:57:44.2	34.57/-116.41	6.0	3.6	A	260/30/040	3.4	8
92/06/30	11:30:29.2	34.09/-116.42	11.6	4.4	A	070/90/010	4.0	14
92/06/30	12:14:49.7	34.09/-116.42	11.9	4.2	A	040/70/-10	3.9	14
92/06/30	12:26:19.3	34.02/-116.35	0.8	3.8	A	040/70/-30	3.7	8
92/06/30	12:34:54.5	34.32/-116.45	4.6	4.3	A	180/50/-80	3.9	8
92/06/30	13:05:36.4	35.68/-117.61	4.7	4.6	A	040/80/010	4.5	8
92/06/30	14:38:11.6	34.00/-116.36	0.9	4.9	A	240/60/-30	5.0	8

continued on next page

continued from previous page

92/06/30	16:45:28.4	34.11/-116.40	3.9	3.8	A	220/70/-20	3.7	14
92/06/30	17:26:30.2	34.64/-116.66	6.0	4.4	A	040/60/-30	3.9	5
92/06/30	20:05:06.6	33.99/-116.36	0.6	4.1	A	050/50/-60	3.8	8
92/07/01	10:32:52.3	34.97/-116.94	0.2	4.3	A	060/90/-10	4.1	8
92/07/01	17:45:46.8	34.28/-116.69	5.9	4.5	B	210/60/-10	4.1	8
92/07/01	20:53:56.8	34.28/-116.73	1.4	4.0	A	050/80/-20	3.8	8
92/07/02	04:26:53.5	34.96/-116.79	2.5	3.6	A	080/80/020	3.3	11
92/07/02	05:16:32.2	34.38/-116.45	0.7	4.0	A	060/60/-10	3.8	8
92/07/02	06:13:43.5	34.13/-116.86	7.9	3.6	A	020/50/-10	3.4	8
92/07/02	06:24:57.1	34.26/-116.74	3.3	3.7	A	060/60/050	3.4	8
92/07/02	12:17:41.1	34.58/-116.57	0.0	3.5	A	190/50/-80	3.5	14
92/07/02	13:00:04.9	35.03/-116.97	3.7	3.5	A	250/50/020	3.3	11
92/07/02	21:03:22.5	34.20/-116.78	2.4	3.6	A	030/60/000	3.4	5
92/07/02	22:25:29.1	35.67/-117.62	5.3	4.3	A	220/80/020	3.9	8
92/07/03	04:15:50.4	34.21/-116.77	10.9	4.2	A	330/50/-40	3.5	17
92/07/03	09:49:32.7	34.97/-116.94	3.8	3.9	A	240/60/010	3.6	8
92/07/03	10:40:07.6	34.20/-116.87	3.7	3.8	A	030/70/010	3.6	8
92/07/03	12:15:42.5	34.18/-116.81	10.0	3.6	A	050/90/060	3.4	20
92/07/03	12:32:24.4	34.54/-116.53	4.6	3.5	A	060/80/040	3.2	8
92/07/03	17:17:06.4	34.26/-116.89	7.6	4.1	A	220/60/000	3.8	11
92/07/05	05:49:38.2	33.94/-116.40	3.2	4.1	A	250/80/010	4.0	8
92/07/05	10:36:19.1	34.62/-116.34	7.8	3.7	A	250/70/-40	3.4	8
92/07/05	10:55:43.3	35.03/-116.97	0.8	4.6	A	240/70/010	4.5	8
92/07/05	21:18:27.1	34.58/-116.32	0.1	5.4	A	080/50/030	5.3	11
92/07/05	22:33:45.5	34.58/-116.30	0.0	4.5	C	090/60/030	4.4	11
92/07/06	04:48:34.5	34.05/-116.43	10.2	3.6	A	060/50/-20	3.3	5
92/07/06	12:00:59.2	34.09/-116.37	1.7	4.4	A	060/90/010	4.2	8

continued on next page

continued from previous page

92/07/07	04:48:52.6	34.25/-116.71	1.3	3.9	A	070/60/020	3.8	11
92/07/07	08:21:03.1	34.07/-116.38	3.2	4.2	A	240/80/-20	3.9	14
92/07/07	22:09:28.3	34.34/-116.47	2.5	4.4	A	310/70/040	4.1	8
92/07/08	02:23:11.3	34.58/-116.33	6.0	4.9	A	080/70/030	4.5	8
92/07/09	01:43:57.6	34.24/-116.84	0.0	4.9	A	240/40/060	5.2	5
92/07/10	01:29:40.0	34.23/-116.85	0.5	4.2	A	250/50/060	4.3	5
92/07/10	02:41:14.4	34.12/-116.39	3.4	3.9	A	030/50/-30	3.7	11
92/07/10	16:01:37.5	34.47/-116.51	1.9	3.5	A	100/60/-10	3.5	14
92/07/10	16:14:02.8	34.96/-116.79	2.3	3.6	A	080/50/020	3.3	8
92/07/11	07:21:36.3	34.45/-116.50	1.7	3.6	A	290/60/010	3.5	11
92/07/11	18:14:16.1	35.21/-118.07	10.7	5.7	A	030/80/030	5.1	14
92/07/12	05:35:13.4	34.55/-116.54	8.7	3.9	A	070/60/000	3.7	17
92/07/13	00:11:51.1	34.33/-116.67	0.0	3.9	A	060/50/-10	3.9	8
92/07/13	05:00:00.8	34.09/-116.41	3.3	3.8	A	030/70/-90	3.7	11
92/07/13	08:25:37.7	35.99/-118.36	0.1	3.5	A	210/70/-60	3.4	8
92/07/13	09:51:03.5	34.97/-116.94	3.7	3.7	A	090/90/020	3.8	8
92/07/13	10:09:18.0	34.97/-116.94	2.8	3.8	A	250/70/020	3.7	8
92/07/14	00:24:59.1	35.99/-118.36	0.0	3.6	A	220/50/-30	3.4	8
92/07/14	13:04:02.6	34.19/-116.80	1.7	3.5	A	230/80/020	3.4	8
92/07/14	15:09:15.7	34.22/-116.77	2.0	3.8	A	280/40/060	3.7	5
92/07/14	20:36:51.5	34.65/-116.64	7.1	3.8	A	130/70/-80	3.4	8
92/07/15	00:18:56.9	34.33/-116.46	0.0	3.9	A	110/70/-30	3.8	5
92/07/15	12:45:21.0	34.12/-116.38	1.7	3.8	A	060/80/020	3.5	8
92/07/16	17:19:17.4	34.44/-116.45	2.7	3.8	A	110/50/050	3.5	11
92/07/18	00:06:11.2	34.10/-116.42	2.6	4.0	A	050/70/-30	3.6	11
92/07/18	06:58:40.3	37.49/-118.93	6.0	3.9	B	210/70/-50	3.7	8
92/07/19	12:44:16.3	34.93/-116.91	0.0	3.6	A	080/80/020	3.6	5

continued on next page

continued from previous page

92/07/20	04:08:22.6	34.20/-116.43	0.4	4.1	A	220/40/-10	4.0	8
92/07/20	04:48:01.5	34.97/-116.94	4.6	4.6	A	260/80/-10	4.4	8
92/07/20	07:10:13.2	34.28/-116.44	0.0	3.6	A	230/50/-40	3.3	2
92/07/20	10:35:11.5	34.98/-116.94	4.4	3.7	A	080/80/000	3.7	11
92/07/20	13:13:19.4	34.99/-116.95	0.0	4.6	A	070/80/010	4.5	5
92/07/21	13:30:01.7	34.15/-116.85	11.9	3.7	A	030/90/020	3.4	14
92/07/21	21:10:29.0	34.22/-116.77	1.9	4.1	A	240/50/010	3.9	8
92/07/21	22:03:36.6	32.81/-118.47	6.0	3.9	C	220/80/020	3.9	14
92/07/21	23:22:10.2	34.13/-116.60	1.7	3.9	A	200/40/-60	4.1	11
92/07/23	07:37:25.6	34.17/-116.81	6.1	3.6	B	180/50/-70	3.4	14
92/07/24	07:23:56.1	34.49/-116.48	9.0	4.0	A	200/40/-60	3.6	14
92/07/24	18:14:36.3	33.90/-116.28	8.2	4.9	A	080/90/-40	4.8	17
92/07/25	04:31:59.9	33.94/-116.31	4.7	4.8	A	250/30/-20	4.6	11
92/07/25	10:27:10.4	34.27/-116.92	5.3	3.9	A	040/80/-10	3.6	8
92/07/25	17:02:20.2	33.94/-116.30	6.4	3.9	A	260/30/-40	3.5	11
92/07/27	20:40:08.8	32.61/-115.63	15.9	4.1	A	030/80/-10	3.5	8
92/07/28	18:27:03.9	34.11/-116.41	0.0	4.6	A	060/60/-30	4.6	8
92/07/31	18:03:52.4	34.10/-116.42	0.1	4.0	A	060/50/-50	3.9	8
92/07/31	22:37:16.9	34.33/-116.46	7.6	3.6	A	230/50/-20	3.4	11
92/08/04	19:06:12.3	34.10/-116.38	0.0	4.0	A	060/70/-10	3.9	5
92/08/05	15:41:54.4	34.65/-116.53	4.2	4.1	A	230/20/020	3.8	8
92/08/05	17:26:10.9	34.10/-116.45	8.4	3.6	B	250/20/-20	3.4	8
92/08/05	22:22:40.8	34.98/-116.95	0.0	4.7	A	240/80/020	4.5	8
92/08/07	00:43:28.4	34.27/-116.77	1.7	4.0	A	050/70/-20	3.7	8
92/08/08	15:37:43.3	34.38/-116.46	2.8	4.5	A	090/60/020	4.3	11
92/08/11	06:11:17.2	34.06/-116.37	0.7	4.2	A	060/70/000	3.9	8
92/08/14	14:43:44.5	34.09/-116.37	0.9	3.9	A	060/80/-20	3.6	8

continued on next page

continued from previous page

92/08/15	00:19:22.6	33.93/-116.31	4.9	3.5	A	270/40/-30	3.3	11
92/08/15	08:24:14.7	34.09/-116.40	0.4	4.8	A	240/80/000	4.4	8
92/08/15	18:18:06.2	34.12/-116.99	4.1	3.7	A	230/30/000	3.9	5
92/08/16	06:30:59.5	34.03/-116.68	10.1	3.8	A	040/80/060	3.6	14
92/08/17	20:41:52.1	34.19/-116.86	11.3	5.1	A	040/70/050	4.8	17
92/08/18	09:46:40.7	34.20/-116.86	12.1	4.2	A	060/40/070	3.9	17
92/08/23	06:40:44.5	35.03/-116.99	3.9	4.1	A	240/60/000	3.8	11
92/08/24	12:43:03.6	34.95/-116.78	6.0	3.7	A	260/60/020	3.4	8
92/08/24	13:51:46.0	34.27/-116.77	1.8	4.3	A	070/70/010	4.2	8
92/08/26	13:21:57.5	34.06/-116.37	0.0	3.8	A	060/80/-10	3.7	5
92/08/27	01:44:37.7	34.94/-116.79	1.3	3.5	A	270/70/040	3.3	8
92/08/27	02:53:35.2	34.98/-116.97	6.0	3.6	A	090/60/040	3.5	8
92/08/30	08:15:12.5	34.01/-118.37	14.4	3.6	A	260/50/030	3.4	8
92/08/31	09:25:40.6	34.46/-116.47	11.0	4.4	A	270/50/-20	3.9	14
92/09/01	12:17:24.8	34.60/-116.32	0.0	4.0	A	300/50/070	3.7	5
92/09/03	06:17:38.4	34.37/-116.44	3.5	3.8	A	110/80/-20	3.4	8
92/09/04	15:02:58.3	36.14/-117.87	3.5	3.9	A	030/90/000	3.8	11
92/09/05	03:29:27.1	34.10/-116.42	3.4	3.9	A	040/70/010	3.6	8
92/09/06	17:51:06.7	34.02/-117.19	6.1	3.6	A	060/60/-40	3.3	8
92/09/09	11:41:36.0	35.07/-117.00	0.6	3.6	A	210/50/-20	3.4	5
92/09/09	11:44:55.0	35.08/-117.00	0.4	4.2	A	250/40/030	4.1	5
92/09/09	12:50:45.1	33.95/-116.33	5.2	4.3	A	230/70/-20	4.2	17
92/09/09	12:52:56.2	33.95/-116.33	5.1	3.5	A	250/60/000	3.4	8
92/09/13	11:46:20.0	36.74/-116.20	6.0	4.7	D	220/50/-50	4.0	11
92/09/15	08:47:11.3	34.06/-116.36	8.3	5.1	A	240/80/000	5.1	11
92/09/16	12:27:22.0	34.05/-116.39	1.0	3.8	A	050/80/010	3.7	8
92/09/18	12:53:35.5	34.05/-116.38	1.4	3.9	A	060/90/030	3.9	8

continued on next page

continued from previous page

92/09/22	18:52:33.3	35.11/-116.72	7.1	4.0	A	280/70/000	3.9	8
92/09/28	12:07:26.2	34.13/-116.40	0.9	3.5	A	030/50/-50	3.4	2
92/10/02	07:19:57.3	34.60/-116.64	3.4	4.6	A	190/60/010	4.4	8
92/10/06	21:32:04.1	34.20/-116.44	1.1	3.7	A	310/60/-30	3.4	5
92/10/11	12:38:12.4	34.94/-116.80	2.7	4.5	A	250/80/020	4.4	8
92/10/17	20:15:55.7	35.07/-116.99	0.0	3.6	A	250/60/010	3.4	5
92/11/14	07:17:16.4	34.97/-116.94	4.5	3.5	A	260/60/-10	3.5	8
92/11/24	09:06:27.0	34.14/-116.88	9.6	3.8	A	040/60/000	3.9	20
92/11/25	02:40:24.9	35.04/-116.98	3.7	4.1	A	260/60/020	3.9	8
92/11/25	07:50:35.0	34.16/-116.42	1.1	3.8	A	070/80/020	3.8	8
92/11/26	21:41:17.2	34.98/-116.95	0.0	4.0	A	250/80/020	3.7	5
92/11/27	16:00:57.5	34.34/-116.90	1.5	5.4	A	220/70/030	5.1	8
92/11/27	18:32:25.0	34.36/-116.90	1.0	4.1	A	280/50/090	4.0	5
92/11/29	14:21:20.5	34.37/-116.88	3.4	4.0	A	050/80/-10	4.0	5
92/12/04	02:08:57.5	34.37/-116.90	3.0	5.3	A	260/50/070	5.0	5
92/12/04	05:25:11.2	34.38/-116.92	2.7	4.7	A	080/40/080	4.3	5
92/12/04	12:59:42.1	34.36/-116.91	0.7	4.3	A	100/40/080	4.1	5
92/12/07	03:33:31.5	34.36/-116.92	1.1	4.0	A	100/40/090	3.8	5
92/12/07	07:50:33.3	35.07/-116.99	3.5	3.8	A	260/60/030	3.7	5
92/12/11	01:38:34.2	34.27/-116.40	2.7	4.1	A	220/80/-10	3.9	5
92/12/13	04:14:03.7	34.98/-116.95	4.2	3.8	A	250/40/000	3.8	11
92/12/21	11:44:02.9	34.09/-116.42	3.6	4.0	A	050/70/020	3.6	8
92/12/27	00:18:38.0	34.35/-116.89	4.4	3.8	A	220/60/-10	3.5	5
92/12/28	18:00:29.2	33.95/-116.31	4.5	3.8	A	100/40/020	3.5	8
93/02/11	12:39:37.0	35.03/-116.97	3.3	4.5	A	240/60/010	4.2	11
93/02/11	15:54:05.4	35.02/-116.97	4.2	3.5	A	100/60/090	3.3	8
93/02/15	07:59:33.2	34.40/-116.46	6.0	4.2	A	240/60/000	4.0	14

continued on next page

continued from previous page

93/03/16	07:50:13.5	34.22/-116.76	1.8	3.5	A	240/90/040	3.5	11
93/03/20	06:56:55.4	34.01/-117.22	9.1	3.8	A	020/30/-50	3.8	11
93/05/12	00:46:55.4	34.97/-116.96	0.1	3.8	A	270/50/040	3.6	5
93/05/17	23:20:50.2	37.17/-117.77	6.0	6.2	D	020/50/-80	6.0	17
93/05/18	01:03:07.7	37.15/-117.76	6.0	4.7	D	240/30/-50	4.6	8
93/05/18	05:10:48.0	37.16/-117.78	6.0	3.5	D	040/30/-70	3.6	11
93/05/18	17:09:05.9	34.29/-117.48	10.2	3.7	A	260/70/040	3.6	11
93/05/18	23:48:55.2	37.06/-117.76	6.0	4.8	D	050/50/-50	4.9	11
93/05/19	03:20:58.9	37.14/-117.78	6.0	4.4	D	200/70/-80	4.4	17
93/05/20	01:17:55.6	37.20/-117.73	6.0	4.0	D	060/80/-40	4.1	14
93/05/20	20:14:14.5	36.10/-117.70	0.8	4.5	A	220/70/-20	4.5	8
93/05/28	04:47:40.6	35.15/-119.10	21.4	5.2	A	210/50/010	4.6	17
93/05/31	08:55:30.0	34.12/-117.00	5.7	4.1	A	210/50/-10	4.1	11
93/06/22	23:08:10.9	34.63/-116.62	7.8	3.8	A	100/60/070	3.5	11
93/08/11	05:48:21.9	37.56/-118.92	6.0	4.4	A	170/70/-50	3.9	5
93/08/21	01:46:38.4	34.03/-116.32	9.1	5.0	A	020/50/-90	4.4	14
93/09/06	08:25:23.1	34.14/-116.84	9.6	4.0	A	210/90/-30	3.7	11
93/09/06	10:32:33.1	35.98/-118.36	0.0	3.7	A	240/50/-50	3.5	8
93/09/06	22:30:12.9	32.36/-115.35	6.0	3.8	B	030/90/-20	3.7	11
93/09/07	12:59:21.8	32.36/-115.36	6.0	3.7	C	210/40/-30	3.7	8
93/09/07	16:41:52.6	34.27/-116.45	0.4	3.5	A	240/40/-40	3.3	5
93/10/04	02:57:36.7	34.01/-116.34	1.7	3.6	A	070/70/-30	3.5	11
93/10/21	14:37:11.6	36.16/-118.03	0.0	3.8	A	020/50/-70	3.8	8
93/10/22	16:30:53.4	36.05/-117.97	0.0	3.7	A	100/80/-20	3.6	2
93/10/26	09:24:07.4	34.95/-116.65	6.0	4.0	A	060/40/020	3.7	8
93/12/03	01:51:24.8	34.26/-116.72	1.6	3.8	A	090/30/030	3.7	11
93/12/08	09:06:28.8	35.01/-116.97	2.3	3.7	A	250/60/030	3.7	8

continued on next page

continued from previous page

93/12/20	17:37:02.5	32.37/-115.36	6.0	4.0	B	020/90/-10	3.9	8
94/01/17	15:54:10.8	34.38/-118.63	13.0	4.9	A	070/60/080	4.6	17
94/01/17	17:56:08.2	34.23/-118.57	19.2	4.6	A	290/20/080	4.4	20
94/01/17	18:20:23.7	34.28/-118.47	11.4	3.5	A	150/50/090	3.4	14
94/01/17	19:35:34.3	34.31/-118.46	2.3	4.0	A	300/90/-40	4.0	17
94/01/17	19:43:53.4	34.37/-118.64	13.9	4.1	A	080/60/090	4.1	11
94/01/17	20:02:05.4	34.41/-118.56	0.0	3.9	A	290/10/080	3.9	11
94/01/17	20:05:27.5	34.33/-118.52	1.9	3.8	A	210/50/-50	3.7	14
94/01/17	20:11:49.3	34.32/-118.50	2.2	3.8	A	290/80/060	3.7	8
94/01/17	20:46:02.4	34.30/-118.57	9.5	4.9	A	030/30/-50	4.8	17
94/01/17	22:19:24.0	34.37/-118.62	11.7	3.9	A	070/50/060	3.9	17
94/01/17	22:31:53.3	34.34/-118.44	0.0	4.1	A	080/30/080	4.1	17
94/01/17	23:33:30.7	34.33/-118.70	9.8	5.6	A	100/60/080	5.9	14
94/01/18	04:01:26.7	34.36/-118.62	0.9	4.3	A	090/50/080	4.3	11
94/01/18	04:31:19.7	34.36/-118.45	4.9	3.8	A	220/60/010	3.8	14
94/01/18	05:49:43.4	34.30/-118.45	6.7	3.9	B	330/20/080	3.7	14
94/01/18	06:29:02.2	34.30/-118.45	8.1	3.8	A	090/40/070	3.7	11
94/01/18	07:23:56.0	34.33/-118.62	14.8	4.0	A	260/30/090	4.1	17
94/01/18	11:35:09.9	34.22/-118.61	12.1	4.2	A	070/60/-30	4.1	11
94/01/18	13:24:44.1	34.32/-118.56	1.7	4.3	A	050/50/000	4.2	8
94/01/18	15:19:54.3	34.21/-118.61	8.7	3.9	A	250/60/010	3.9	14
94/01/18	15:23:46.9	34.38/-118.56	7.7	4.9	A	290/50/080	4.8	14
94/01/18	15:51:44.9	34.24/-118.47	12.5	4.0	A	110/40/090	3.8	14
94/01/18	16:23:34.7	34.37/-118.57	1.3	3.9	A	090/40/090	3.9	11
94/01/18	18:03:55.7	34.33/-118.45	6.1	3.6	A	130/40/080	3.5	8
94/01/19	04:40:48.0	34.36/-118.57	2.6	4.4	A	290/40/070	4.3	11
94/01/19	07:14:06.2	34.29/-118.47	11.6	4.0	A	230/50/070	3.6	14

continued on next page

continued from previous page

94/01/19	09:13:10.9	34.30/-118.74	13.0	4.1	A	290/70/070	4.1	14
94/01/19	14:09:14.8	34.22/-118.51	17.5	4.5	A	110/50/070	4.2	20
94/01/19	14:46:35.2	34.29/-118.47	6.1	3.9	B	120/50/090	3.9	11
94/01/19	15:03:47.6	34.29/-118.46	8.5	3.6	A	090/50/070	3.5	8
94/01/19	19:50:09.0	34.28/-118.45	10.0	3.7	A	290/40/070	3.6	14
94/01/19	21:09:28.6	34.38/-118.71	14.4	5.1	A	100/40/090	5.1	14
94/01/21	18:39:15.3	34.30/-118.47	10.6	4.5	A	130/60/080	4.5	11
94/01/21	18:52:44.2	34.30/-118.45	7.6	4.3	A	090/50/080	4.1	11
94/01/21	18:53:44.6	34.30/-118.46	7.7	4.3	A	100/50/090	4.2	11
94/01/23	08:55:08.7	34.30/-118.43	6.0	4.1	A	110/50/080	4.0	8
94/01/24	02:41:02.7	34.25/-118.47	13.0	3.6	A	120/30/090	3.7	14
94/01/24	04:15:18.8	34.35/-118.55	6.5	4.6	A	280/40/090	4.4	11
94/01/24	05:50:24.3	34.36/-118.63	12.1	4.3	A	080/60/070	4.1	11
94/01/24	05:54:21.1	34.36/-118.63	10.9	4.2	A	060/60/050	4.1	11
94/01/26	12:28:47.2	34.30/-118.47	10.0	3.8	A	000/20/-50	3.7	11
94/01/27	17:19:58.8	34.27/-118.56	14.9	4.6	A	130/80/-70	4.3	17
94/01/28	20:09:53.4	34.38/-118.49	0.7	4.2	A	110/30/070	4.2	8
94/01/29	11:20:36.0	34.31/-118.58	1.1	5.1	A	060/50/010	5.1	8
94/01/29	12:16:56.3	34.28/-118.61	2.7	4.3	A	230/80/010	4.1	8
94/02/01	08:01:52.0	37.31/-118.36	6.0	4.0	B	220/50/-50	3.9	8
94/02/03	16:23:35.4	34.30/-118.44	9.0	4.0	A	280/60/070	3.9	8
94/02/06	13:19:27.0	34.29/-118.48	9.3	4.1	A	110/50/060	3.9	8
94/02/11	14:07:53.1	34.33/-118.48	5.0	3.7	A	310/60/080	3.7	14
94/03/20	21:20:12.3	34.23/-118.47	13.1	5.2	A	100/50/070	5.1	14
94/03/23	02:59:14.1	31.74/-116.19	10.0	4.7	A	020/50/050	4.7	14
94/04/06	19:01:04.1	34.19/-117.10	7.3	4.8	A	210/90/-10	4.4	11
94/05/04	04:09:12.4	34.33/-118.46	5.3	3.8	A	140/50/060	3.7	11

continued on next page

continued from previous page

94/05/16	08:40:46.8	34.33/-118.62	14.4	3.8	A	120/60/090	3.6	14
94/05/19	06:12:44.5	34.32/-118.44	8.1	3.7	A	090/60/070	3.7	8
94/05/25	12:56:57.1	34.31/-118.39	7.0	4.4	A	260/40/050	4.4	11
94/06/02	03:27:14.4	34.28/-118.46	11.3	3.8	A	120/70/080	3.7	14
94/06/15	05:59:48.6	34.31/-118.40	7.4	4.1	A	110/50/070	4.0	8
94/06/16	16:24:27.5	34.27/-116.40	3.4	5.0	A	230/80/000	4.7	8
94/06/29	07:34:35.2	34.27/-116.41	1.0	3.5	A	060/30/040	3.2	5
94/07/11	06:50:49.7	34.26/-118.69	15.8	3.8	A	230/70/020	3.6	14
94/08/01	21:34:31.1	34.64/-116.52	9.1	4.9	A	090/90/000	4.2	11
94/08/03	12:40:13.7	34.33/-118.46	7.4	3.5	A	260/60/050	3.4	8
94/08/07	15:10:26.0	33.99/-116.27	7.0	4.0	A	080/90/020	3.7	8
94/08/11	02:22:53.5	32.34/-115.28	6.0	4.6	C	040/30/-40	4.2	14
94/08/15	08:07:32.9	33.81/-116.20	7.0	3.8	A	210/60/-50	3.7	8
94/10/03	14:00:47.6	32.03/-114.94	5.0	4.9	A	050/80/-20	4.9	20
94/10/19	00:49:58.8	35.51/-117.49	3.4	4.2	A	250/70/070	3.8	8
94/11/20	04:31:43.5	34.01/-116.32	6.3	4.2	A	070/80/-30	3.8	8
94/12/06	03:36:24.3	34.29/-118.39	8.3	3.7	A	080/30/050	3.8	14
94/12/06	03:48:34.5	34.29/-118.39	9.0	4.5	A	100/40/070	4.5	11
94/12/20	10:27:47.8	35.91/-120.48	14.0	4.9	B	050/70/-10	4.8	20
95/02/19	21:24:18.1	34.05/-118.92	15.6	4.4	A	250/70/030	3.9	8
95/02/19	22:54:53.3	34.05/-118.92	15.6	3.8	A	250/40/060	3.7	17
95/03/01	15:56:35.8	33.74/-118.61	14.4	3.7	A	120/90/060	3.6	20
95/03/05	02:48:47.9	37.60/-118.82	6.0	4.4	A	180/80/-10	3.8	11
95/04/04	05:08:15.9	34.27/-117.47	9.5	3.7	A	100/60/060	3.6	14
95/04/15	22:00:46.3	34.32/-118.53	4.7	3.5	A	110/50/090	3.5	8
95/05/07	11:03:33.0	33.90/-116.29	10.7	4.8	A	090/70/030	4.6	11
95/06/26	08:40:28.9	34.39/-118.67	13.3	5.0	A	090/40/090	4.8	14

continued on next page

continued from previous page

95/07/28	07:07:30.4	33.54/-116.69	8.6	3.6	A	240/70/-10	3.4	8
95/08/17	22:39:59.0	35.78/-117.66	5.6	5.4	A	040/40/-40	5.3	11
95/08/25	02:59:35.0	35.03/-116.96	6.5	3.5	A	070/80/020	3.4	11
95/08/30	15:29:54.6	35.79/-117.64	5.0	4.2	A	050/50/-60	4.3	5
95/08/30	15:54:22.5	35.80/-117.64	3.4	4.0	A	030/40/-70	3.9	2
95/08/31	01:58:58.8	35.79/-117.64	5.2	3.9	A	080/60/-10	3.8	8
95/09/05	20:27:18.4	34.20/-116.44	0.0	4.5	A	060/90/-10	4.3	5
95/09/11	18:37:23.7	35.79/-117.66	6.6	4.3	A	050/70/-40	3.9	11
95/09/20	23:27:36.3	35.76/-117.64	5.4	5.8	A	060/80/-10	5.4	14
95/09/21	07:57:41.3	35.76/-117.63	5.4	4.1	A	060/80/-50	3.9	8
95/09/21	23:48:39.2	35.76/-117.64	5.4	4.0	A	250/70/-10	4.0	8
95/09/25	04:47:29.2	35.81/-117.62	9.4	5.0	A	010/60/-10	4.5	14
95/09/28	11:36:28.4	35.81/-117.64	4.4	3.5	A	020/40/-70	3.6	5
95/10/02	00:10:53.6	35.81/-117.65	4.7	3.8	A	210/40/-80	3.6	2
95/10/05	16:42:19.0	34.24/-118.68	14.1	3.7	A	230/70/000	3.6	8
95/10/18	12:42:04.8	35.74/-117.63	3.7	4.2	A	190/80/050	4.2	14
95/10/22	14:41:03.8	34.14/-116.43	2.3	3.8	A	250/40/010	3.6	8
95/12/02	00:29:08.6	35.78/-117.69	5.8	3.7	A	240/70/-30	3.6	8
95/12/25	23:40:07.7	33.19/-115.61	4.2	3.8	A	080/70/-20	3.9	8
95/12/31	21:48:23.1	35.10/-118.31	7.9	4.0	A	200/70/-40	3.9	8
96/01/05	11:57:40.1	33.94/-116.37	6.9	3.8	B	210/40/-70	3.6	8
96/01/07	10:32:46.4	36.47/-117.62	6.0	3.8	B	220/80/-50	3.7	11
96/01/07	14:32:53.1	35.77/-117.65	5.9	5.2	A	060/70/-20	5.0	11
96/01/07	16:04:14.9	35.77/-117.64	5.4	3.5	A	240/40/-30	3.6	8
96/01/08	08:57:11.0	35.76/-117.62	3.9	4.1	A	060/90/-20	3.9	5
96/01/08	10:52:28.9	35.78/-117.64	5.1	4.3	A	020/40/-70	4.5	8
96/01/08	14:49:04.1	35.78/-117.64	4.9	3.7	A	200/50/-60	3.6	8

continued on next page

continued from previous page

96/01/08	22:40:36.0	35.77/-117.65	5.5	3.6	A	220/60/-20	3.5	8
96/01/12	00:35:06.0	35.79/-117.66	5.6	3.6	A	060/50/-40	3.5	5
96/01/13	17:55:23.4	34.36/-118.45	4.3	3.5	A	020/80/-40	3.4	8
96/01/25	05:35:12.7	34.16/-116.45	1.9	3.5	A	280/40/-20	3.4	11
96/01/26	13:06:02.8	35.79/-117.67	5.7	4.2	A	060/70/-30	3.9	8
96/01/30	18:34:10.9	34.34/-118.48	10.7	3.8	A	240/60/050	4.0	14
96/02/04	06:28:47.6	35.03/-116.96	3.7	3.6	A	060/80/040	3.5	8
96/02/09	12:14:12.7	34.37/-116.46	0.9	3.6	A	260/80/-40	3.7	8
96/02/15	20:16:12.4	37.62/-118.88	6.0	4.0	B	090/50/-50	3.7	8
96/02/17	01:03:48.8	37.63/-118.88	6.0	4.0	B	340/60/-80	3.8	11
96/03/17	03:18:23.0	37.63/-118.94	6.0	3.8	A	030/90/010	3.4	2
96/03/20	05:03:09.3	31.90/-115.81	5.0	4.4	A	080/40/080	4.0	8
96/03/29	18:14:49.8	37.63/-118.84	6.0	4.3	A	010/90/000	3.7	2
96/03/31	19:18:07.1	37.63/-118.87	6.0	3.7	B	020/80/-10	3.5	5
96/03/31	19:27:38.8	37.63/-118.87	5.5	4.3	C	020/90/-30	3.6	2
96/04/01	04:13:37.0	37.64/-118.83	6.0	4.3	A	170/30/-70	3.9	14
96/04/08	23:46:41.3	34.38/-116.46	1.2	3.9	A	070/50/-60	3.9	8
96/05/01	19:49:56.4	34.35/-118.70	14.4	4.1	A	080/60/080	3.9	14
96/05/22	05:54:12.1	33.13/-115.64	0.1	3.5	A	270/40/-50	3.6	17
96/07/07	06:27:06.1	31.54/-115.68	6.0	4.3	D	220/60/-60	3.7	11
96/08/14	03:05:27.5	34.60/-116.28	6.0	4.3	C	270/80/020	4.0	5
96/10/23	22:09:29.4	34.48/-119.35	14.5	4.2	A	260/50/050	3.8	8
96/11/27	01:42:43.8	33.95/-116.31	6.0	4.1	A	270/40/000	4.1	8
96/11/27	20:17:24.1	36.08/-117.65	1.2	5.3	A	240/70/010	4.9	11

ϕ, δ: strike and dip of the fault plane in degrees; λ: rake of the slip in degrees.

h: source depth in kms.

Bibliography

Ammon, C. J., G. E. Randall, and G. Zandt, On the nonuniqueness of receiver function inversions, *J. Geophys. Res.*, *95*, 15,303–15,318, 1990.

Argand, E., La tectonique de L'Asie, in *Proceedings of the 13th Int. Geol. Congr., Brussels*, pp. 171–372, 1924.

Baranowski, H., H. Armbruster, L. Seeber, and P. Molnar, Focal depths and fault plane solutions of earthquakes and active tectonics of the Himalaya, *J. Geophys. Res.*, *89*, 6919–6928, 1984.

Barazangi, M., and J. Ni, Velocities and propagation characteristics of Pn and Sn beneath the Himalayan arc and Tibetan plateau: Possible evidence for underthrusting of Indian continental lithosphere beneath Tibet, *Geology*, *10*, 179–185, 1982.

Beghoul, N., M. Barazangi, and B. Isacks, Lithospheric structure of Tibet and western North America, mechanisms of uplift and a comparative study, *J. Geophys. Res.*, *98*, 1997–2016, 1993.

Bird, P., Initiation of intracontinental subduction in the Himalayas, *J. Geophys. Res.*, *83*, 4975–4987, 1978.

Brandon, C., and B. Romanowicz, A 'no-lid' zone in the central Chang-Tang platform of Tibet: Evidence from pure path phase velocity measurement of long period Rayleigh waves, *J. Geophys. Res.*, *91*, 6547–6546, 1986.

Chen, W. P., A brief update on the focal depths of intracontinental earthquakes and their correlation with heat flow and tectonic age, *Seismol. Res. Lett.*, *59*, 263–272, 1988.

Chen, W. P., and P. Molnar, Constraints on the seismic wave velocity structure beneath the Tibetan Plateau and their tectonic implication, *J. Geophys. Res.*, *86*, 5937–5962, 1981.

Chen, W. P., and P. Molnar, Focal depths of intracontinental and intraplate earthquakes and their implications for the thermal and mechanical properties of the lithosphere, *J. Geophys. Res.*, *88*, 4183–4214, 1983.

Chen, W. P., J. L. Nabelek, T. J. Fitch, and P. Molnar, An intermediate depth earthquake beneath Tibet: Source characteristics of the event of September 14, 1976, *J. Geophys. Res.*, *86*, 2863–2876, 1981.

Deng, W. A., A preliminary study on the petrology and petrochemistry of Quaternary volcanic rocks of northern Tibet autonomous region, *Acta Geol. Sinica*, *52*, 148–162, 1978.

Dewey, J. F., and J. M. Bird, Mountain belts and the new global tectonics, *J. Geophys. Res.*, *75*, 2625–2647, 1970.

Dewey, J. F., and K. Burke, Tibetan, Variscan and Precambrian basement reactivation: Products of a continental collision, *J. Geol.*, *81*, 683–692, 1973.

Dewey, J. F., R. M. Shackleton, C. Chang, and Y. Sun, The tectonic evolution of the Tibetan plateau, *Phil. Trans. R. Soc. Lond.*, *A327*, 379–413, 1988.

Doser, D. I., and H. Kanamori, Depth of seismicity in the Imperial Valley region 1977-1983 and its relationship to heat flow, crustal structure, and the October 15, 1979, earthquake, *J. Geophys. Res.*, *91*, 675–688, 1986.

Dreger, D. S., and D. V. Helmberger, Determination of source parameters at regional distances with three-component sparse network data, *J. Geophys. Res.*, *98*, 8107–8125, 1993.

Dziewonski, A. M., and J. H. Woodhouse, An experiment in systematic study of

global seismicity: Centroid-moment tensor solutions for 201 moderate and large earthquakes of 1981, *J. Geophys. Res.*, *88*, 3247–3271, 1983.

Ekstrom, G., A broadband method of earthquake analysis, Ph.D. thesis, Harvard Univ., Cambridge, Mass., 1987.

England, P. C., and G. A. Houseman, Finite strain calculations of continental deformation II: Application to the India-Asia plate collision, *J. Geophys. Res.*, *91*, 3664–3676, 1986.

England, P. C., and D. P. McKenzie, A thin viscous sheet model for continental deformation, *Geophys. J. R. astr. Soc.*, *70*, 295–321, 1982.

Fan, G., J. F. Ni, and T. C. Wallace, Active tectonics of the Pamirs and Karakorum, *J. Geophys. Res.*, *99*, 7131–7160, 1994.

Fan, G. W., and T. C. Wallace, The determination of source parameters for small earthquakes from a single very broadband seismic station, *Geophys. Res. Lett.*, *18*, 1385–1388, 1991.

Fielding, E., B. Isacks, M. Barazangi, and C. Duncan, How flat is Tibet, *Geology*, *22*, 163–167, 1994.

Harrison, T. M., P. Copeland, W. Kidd, and A. Yin, Raising Tibet, *Science*, *255*, 1663–1670, 1992.

Hauksson, E., H. Kutton, H. Kanamori, L. Jones, J. Mori, S. Hough, and G. Roquemore, Preliminary report on the 1995 Ridgecrest earthquake sequence in eastern California, *Seismol. Res. Lett.*, *66*, 54–60, 1995.

Helmberger, D. V., Theory and application of synthetic seismograms, in *Earthquakes: Observation, Theory and Interpretation*, pp. 174–222, Soc. Italiana di Fisica, Bolgna, Italy, 1983.

Helmberger, D. V., and G. R. Engen, Modeling the long-period body waves from shallow earthquakes at regional ranges, *Bull. Seismol. Soc. Am.*, *70*, 1699–1714, 1980.

Helmberger, D. V., and S. D. Malone, Modeling local earthquakes as shear dislocations in a layered half space, *J. Geophys. Res.*, *80*, 4881–4888, 1975.

Hilterman, F. J., Amplitudes of seismic waves – a quick look, *Geophysics*, *40*, 745–762, 1975.

Hirn, A., A. Nercessian, M. Sapin, G. Jobert, Z. X. Xu, E. Y. Gao, D. Y. Lu, and J. W. Teng, Lhasa block and bordering sutures - a continuation of a 500-km Moho traverse through Tibet, *Nature*, *307*, 25–27, 1984a.

Hirn, A., et al., Crustal structure and variability of the Himalayan border of Tibet, *Nature*, *307*, 23–25, 1984b.

Hirn, A., et al., Seismic anisotropy as an indicator of mantle flow beneath the Himalaya and Tibet, *NATURE*, *375*, 571–574, 1995.

Jobert, N., B. Journet, G. Jobert, A. Hirn, and S. K. Zhong, Deep-structure of southern Tibet inferred from the dispersion of Raeyleigh-waves through a long-period seismic network, *Nature*, *313*, 386–388, 1985.

Kawakatsu, H., Automatic near-realtime CMT inversion, *Geophys. Res. Lett.*, *22*, 2569–2572, 1995.

Kern, H., and A. Richter, Temperature derivatives of compressional and shear wave velocities in crustal and mantle rocks at 6 kbar confining pressure, *J. Geophys.*, *49*, 47–56, 1981.

Kidd, W. S., Y. Pan, C. Chang, M. P. Coward, J. F. Dewey, A. Gansser, P. Molnar, R. M. Shackleton, and Y. Sun, Geological mapping of the 1985 Chinese-British Tibetan (Xizang-Qinghai) plateau geotraverse rout, *Phil. Trans. R. Soc. Lond.*, *A327*, 287–305, 1988.

Langston, C. A., The effect of planar dipping structure on source and receiver responses for constant ray parameter, *Bull. Seismol. Soc. Am.*, *67*, 1029–1050., 1977.

Langston, C. A., Structure under Mount Rainier, Washington, inferred from teleseismic body waves, *J. Geophys. Res.*, *84*, 4749–4762, 1979.

Lin, J., and D. Watts, Palaeomagnetic results from the Tibetan plateau, *Phil. Trans. R. Soc. Lond.*, *A327*, 239–262, 1988.

Lu, D., and X. Wang, The crust structure and deep internal process in the Tuotuohe area of the north Qinghai-Xizang Plateau, *Bull. of the Chinese Academy of Geol. Sci.*, *21*, 227–237, 1990.

Lyon-Caen, H., Comparison of the upper mantle shear wave velocity structure of the Indian Shield and the Tibetan Plateau and tectonic implications, *Geophys. J. R. astr. Soc.*, *86*, 727–749, 1986.

Marauyama, S., J. G. Liou, and T. Seno, Mesozoic and Cenozoic evolution of Asia, in *The evolution of the Pacific ocean margins*, edited by Z. Ben-Avraham, pp. 75–99, Oxford University Press, 1989.

Marone, C., and C. Scholz, The depth of seismic faulting and the upper transition from stable to unstable slip regimes, *Geophys. Res. Lett.*, *15*, 621–624, 1988.

McNamara, D. E., T. J. Owens, and W. R. Walter, Observations of regional phase propagation across the Tibetan plateau, *J. Geophys. Res.*, *100*, 22215–22229, 1995.

McNamara, D. E., W. R. Walter, T. J. Owens, and C. J. Ammon, Upper–mantle velocity structure beneath the Tibetan plateau from Pn travel–time tomography, *J. Geophys. Res.*, *102*, 493–505, 1997.

Meissner, R., *The continental crust, a geophysical approach*, Academic Press, 1986.

Meissner, R., and J. Strehlau, Limits of stresses in continental crust and their relationship to the depth-frequence distribution of shallow earthquakes, *Tectonics*, *1*, 73–89, 1982.

Mellman, G. R., and D. V. Helmberger, A modified first-motion approximation for the synthesis of body-wave seismograms, *Geophys. J. R. astr. Soc.*, *54*, 129–140, 1978.

Molnar, P., A review of geophysical constraints on the deep structure of the Tibetan plateau, the Himalaya and the Karakoram, and their tectonic implications, *Phil. Trans. R. Soc. Lond.*, *A326*, 33–88, 1988.

Molnar, P., and W. P. Chen, Focal depths and fault plane solutions of earthquakes under the Tibetan plateau, *J. Geophys. Res.*, *88*, 1180–1196, 1983.

Molnar, P., and H. Lyon-Caen, Fault plane solutions of earthquakes and active tectonics of the Tibetan plateau and its margins, *Geophys. J. Int.*, *99*, 123–153, 1989.

Molnar, P., and P. Tapponnier, Cenozoic tectonics of Asia: Effects of a collision, *Science*, *189*, 419–426, 1975.

Molnar, P., and P. Tapponnier, Relation of eastern China to the India-Eurasia collision: Application of slip-line field theory to large-scale continental tectonics, *Geology*, *5*, 212–216, 1977.

Molnar, P., B. C. Burchfiel, Z. Zhao, K. Liang, S. Wang, and M. Huang, Geologic evolution of Northern Tibet: Results of an expedition to Ulugh Muztagh, *Science*, *235*, 249–253, 1987.

Molnar, P., P. England, and J. Martinod, Mantle dynamics, uplift of the Tibetan plateau, and the Indian monsoon, *Rev. Geophys.*, *31*, 357–396, 1993.

Nabelek, J., and G. Xia, Moment-tensor analysis using regional data: Application to the 25 March, 1993, Scotts Mills, Oregon, earthquake, *Geophys. Res. Lett.*, *22*, 13–16, 1995.

National Imagery and Mapping Agency, NASA/Goddard Space Flight Center, WGS 84 EGM96 (complete to degree and order 360), 1997.

Neele, F., and R. Snieder, Topography of the 400-km discontinuity from observations of long-period P400P phases, *Geophys. J. Int.*, *109*, 670–682, 1992.

Nelson, K. D., et al., Partially molten middle crust beneath southern Tibet - synthesis of project INDEPTH results, *SCIENCE*, *274*, 1684–1688, 1996.

Ni, J., and M. Barazangi, High-frequency seismic-wave propagation beneath the Indian shield, Himalayan arc, Tibetan plateau and surrounding regions – high uppermost mantle velocities and efficient Sn propagation beneath Tibet, *J. Geophys. Res.*, *72*, 665–689, 1983.

Ni, J., and M. Barazangi, Seismotectonics of the Himalayan collision zone: Geometry of the underthrusting Indian plate beneath the Himalaya, *J. Geophys. Res.*, *89*, 1147–1163, 1984.

Owens, T. J., and R. S. Crosson, Shallow structure effects on broadband teleseismic P waveforms, *Bull. Seismol. Soc. Am.*, *77*, 96–108, 1988.

Owens, T. J., and G. Zandt, Implications of crustal property variations for models of Tibetan plateau evolution, *Nature*, *387*, 37–43, 1997.

Owens, T. J., G. Zandt, and S. R. Taylor, Seismic evidence for ancient rift beneath the Cumberland plateau, Tennessee: A detailed analysis of broadband teleseismic P waveforms, *J. Geophys. Res.*, *89*, 7783–7795, 1984.

Owens, T. J., G. E. Randall, F. T. Wu, and R. S. Zeng, PASSCAL instrument performance during the Tibetan plateau passive seismic experiment, *Bull. Seismol. Soc. Am.*, *83*, 1959–1970, 1993.

Patriat, P., and J. Achache, India Eurasia collision chronology has implications for crustal shortening and driving mechanism of plates, *Nature*, *311*, 615–621, 1984.

Patton, H. J., Reference point method for determining the source and path effects of surface waves, *J. Geophys. Res.*, *85*, 821–848, 1980.

Patton, H. J., and G. Zandt, Seismic moment tensors of western U.S. earthquakes and implication for the tectonic stress field, *J. Geophys. Res.*, *96*, 18245–18259, 1991.

Polet, J., and H. Kanamori, Automated CMT inversion using surface waves (abstract), *Eos, Trans. AGU*, *77(46)*, Fall Meeting Suppl., 1995.

Powell, C. M., and P. J. Conaghan, Plate tectonics and the Himalayas, *Earth Planet. Sci. Lett.*, *20*, 1–12, 1973.

Powell, C. M., and P. J. Conaghan, Tectonic models of the Tibetan Plateau, *Geology*, *3*, 727–731, 1975.

Randall, G. E., C. J. Ammon, and T. J. Owens, Moment-tensor estimation using regional seismograms from portable network deployments, *Geophys. Res. Lett.*, *22*, 1665–1668, 1995.

Ritsema, J., and T. Lay, Rapid source mechanism determination of large ($M_w \geq 5$) earthquakes in the western United States, *Geophys. Res. Lett.*, *20*, 1611–1614, 1993.

Romanowicz, B., Constraints on the structure of the Tibet plateau from pure path phase velocities of Love and Rayleigh-waves, *J. Geophys. Res.*, *87*, 6865–6883, 1982.

Saikia, C. K., and L. J. Burdick, Fine-structure of Pnl waves from explosion, *J. Geophys. Res.*, *96*, 14383–14401, 1991.

Scott, P., and D. V. Helmberger, Applications of the Kirchhoff–Helmholtz integral to problems in seismology, *Geophys. J. R. astr. Soc.*, *72*, 237–254, 1983.

Scrivner, C. W., and D. Helmberger, Preliminary work on an early warning and rapid response program for moderate earthquakes, *Bull. Seismol. Soc. Am.*, *85*, 1257–1265, 1995.

Sengor, A. M. C., and A. Natalin, Paleotectonics of Asia: fragments of a synthesis, in *Tectonic evolution of Asia*, edited by A. Yin and T. M. Harrison, pp. 486–640, Cambridge University Press, 1996.

Sibson, R., Roughness at the base of the seismogenic zone: Contributing factors, *J. Geophys. Res.*, *89*, 5791–5799, 1984.

Sipkin, S. A., Estimation of earthquake source parameters by the inversion of waveform data: Global seismicity, 1981-1993, *Bull. Seismol. Soc. Am.*, *76*, 1515–1541, 1986.

Song, X. J., D. V. Helmberger, and L. Zhao, Broadband modeling of regional seismograms: The Basin and Range crustal structure, *Geophys. J. Int.*, *125*, 15–29, 1996.

Tapponnier, P., G. Peltzer, A. Y. Ledain, R. Armijo, and P. Cobbold, Propagating extrusion tectonics in Asia: New insight from simple experiments with plasticine, *Geology*, *10*, 611–616, 1982.

Tapponnier, P., B. Meyer, J. P. Avouac, G. Peltzer, and Y. Gaudemer, Active thrusting and folding in the Qilian-Shan, and decoupling between upper crust and mantle in northeastern Tibet, *Earth Planet. Sci. Lett.*, *97*, 382–403, 1990.

Teng, J., S. Xiong, Z. Yin, Z. Xu, X. Wang, and D. Lu, Structure of the crust and upper mantle pattern and velocity distribution characteristic at northern region of the Himalayan mountains, *Acta Geophys. Sinica*, *26*, 525–540, 1983.

Thatcher, W., and T. C. Hanks, Source parameters of southern California earthquakes, *J. Geophys. Res.*, *78*, 8547–8576, 1973.

Thio, H. K., and H. Kanamori, Moment-tensor inversions for local earthquakes using surface waves recorded at TERRAscope, *Bull. Seismol. Soc. Am.*, *85*, 1021–1038, 1995.

Vanderlee, S., H. Paulssen, and G. Nolet, Variability of p660s phases as a consequence of topography of the 660 km discontinuity, *Phys. Earth Planet. Inter.*, *86*, 147–164, 1994.

Wallace, T. C., and D. V. Helmberger, Determination of seismic parameters of moderate-size earthquake from regional waveforms, *Phys. E-Plan.*, *30*, 185–196, 1982.

Walter, W. R., Source parameters of the June 29 Little Skull Mountain earthquake from complete regional waveforms at a single station, *Geophys. Res. Lett.*, *20*, 403–406, 1993.

Wang, C. Y., and R. B. Herrmann, A numerical study of P, SV, and SH-wave generation in a plane layered medium, *Bull. Seismol. Soc. Am.*, *70*, 1015–1036, 1980.

Westaway, R., Crustal volume balance during the India-Eurasia collision and altitude of the Tibetan plateau: A working hypothesis, *J. Geophys. Res.*, *100*, 15173–15192, 1993.

Wittlinger, G., et al., Seismic tomography of northern Tibet and Kunlun: Evidence for crustal blocks and mantle velocity contrasts, *Earth Planet. Sci. Lett.*, *139*, 263–279, 1996.

Yin, A., and S. Nie, A Phanerozoic palinspastic reconstruction of China and its neighboring regions, in *Tectonic evolution of Asia*, edited by A. Yin and T. M. Harrison, pp. 442–485, Cambridge University Press, 1996.

Zhao, L. S., and D. V. Helmberger, Geophysical implication from relocation of Tibetan earthquakes; hot lithosphere, *Geophys. Res. Lett.*, *18*, 1070–1084, 1991.

Zhao, L. S., and D. V. Helmberger, Source estimation from broadband regional seismograms, *Bull. Seismol. Soc. Am.*, *84*, 91–104, 1994.

Zhao, L. S., and J. Xie, Lateral variation in compressional velocities beneath the Tibetan plateau from Pn travel-time tomography, *Geophys. J. Int.*, *115*, 1070–1084, 1993.

Zhao, L. S., D. V. Helmberger, and D. G. Harkrider, Shear-velocity structure of

the crust and upper mantle beneath the Tibetan plateau and southeastern China, *Geophys. J. Int.*, *105*, 713–730, 1991.

Zhao, W., and J. Morgan, Uplift of the Tibet plateau, *Tectonics*, *4*, 359–369, 1985.

Zhao, W., and W. J. Morgan, Injection of India crust into Tibetan lower crust: a two-dimensional finite element model study, *Tectonics*, *6*, 489–504, 1987.

Zhao, W., K. D. Nelson, and P. I. Team, Deep seismic reflection evidence for continental underthrusting beneath southern Tibet, *Nature*, *366*, 557–559, 1993.

Zhu, L., and D. V. Helmberger, High frequency S-wave attenuation on the Tibet plateau (abstract), *Seismol. Res. Lett.*, *66*, 53, 1995.

Zhu, L., R. S. Zeng, F. T. Wu, T. J. Owens, and G. E. Randall, Preliminary study of crust-upper mantle structure of the Tibetan plateau by using broadband teleseismic body waveforms, *Acta Seismol. Sinica*, *6*, 305–315, 1993.

Zhu, L., T. J. Owens, and G. E. Randall, Lateral variation in crustal structure of the northern Tibetan plateau inferred from teleseismic receiver functions, *Bull. Seismol. Soc. Am.*, *85*, 1531–1540, 1995.